Turbulent jets in the presence of a turbulent ambient

By

Amirhossein Afrooz

Department of Civil Engineering and Applied Mechanics

McGill University

Montreal, Qc, Canada

February 2019

A thesis submitted to McGill University
in partial fulfillment of the requirements of the degree of
Master of Engineering
© Amirhossein Afrooz, 2019

Abstract

Turbulent mixing, which leads to dilution or chemical reactions (including combustion) at a molecular level, is studied using a passive scalar. Khorsandi (2013) and Perez-Alvarado (2016) studied the velocity and concentration fields of an axisymmetric turbulent jet in zero mean flow, respectively, in a quiescent and turbulent ambient. The aim of the present study is to extend this work observing a turbulent jet released into a nearly homogeneous isotropic turbulent background with negligible mean flow created with a random jet array. The characteristic of the jet in a turbulent background flow is compared to that released into a quiescent background. Planar laser induced fluorescence (PLIF) is used for flow visualization and to quantify concentrations in cross-sections of turbulent jets with Reynolds numbers of 5800 and 10600 at axial distances between x/D of 20 and 70. The data was post-processed using MATLAB codes.

Flow visualisation shows that the jet cross-section has greater variation in position and shape when released into a turbulent ambient, due to the larger eddies of the turbulence distorting the jet path and the smaller eddies distorting the jet cross-section, until at some downstream distance the turbulence results in the breakup of the jet (zero mean jet velocity). The increased variability of the jet is seen in time traces of the centreline concentration. The jet cross-sections are spatially averaged to determine the rate of decrease of the concentration and increase of the jet half width with axial distance. Normalized centreline concentration varies with normalized axial distance as x^{-1} in a quiescent ambient and with $x^{-1.7}$ for the jet with Re = 10600 and $x^{-2.1}$ for the jet with Re = 5800 in the turbulent ambient. The normalized jet half width varies with normalized axial distance as x^1 in a quiescent ambient and with $x^{1.2}$ for jet Re = 10600 and $x^{1.4}$ for jet Re = 5800 in the turbulent ambient. The position of the centre of mass of the jet cross-sections indicated a greater meandering of the jet path with downstream distance (Re = 10600). The radius of gyration of the jet was used to identify the growth in width of the cross-section independent of the meandering of the jet path. The normalized radius of gyration of the jet varied as x^{1.8} for the jet released in both quiescent and turbulent ambient, however the magnitude was greater in the turbulent ambient with a greater increase for the lower Reynolds number jet. The downstream evolution of the crosssectional shape factor also indicated the greater disruption of the cross-section in the turbulent ambient. Lastly, the decay in the time averaged centreline concentration was compared to that of the centreline velocity and was found to decrease more gradually in the turbulent ambient.

In summary, the turbulence in the ambient progressively breaks up the jet structure and distorts the jet path resulting in a faster rate of decay of the jet, which is greater for jets with lower Reynolds number.

Résumé

Le mélange turbulent conduit à la dilution et les réactions chimiques (y compris la combustion) au niveau moléculaire est étudié en utilisant un scalaire passif. Khorsandi (2013) et Perez-Alvarado (2016) ont étudié les champs de vitesse et de concentration d'un jet turbulent axisymétrique dans un écoulement moyen nul, respectivement, dans un environnement ambiant au repos et turbulent. Le but de la présente étude est d'étendre ce travail en observant un jet turbulent libéré dans un fond turbulent isotrope presque homogène avec un écoulement moyen négligeable créé avec un réseau de jets aléatoires et en le comparant à un jet turbulent libéré dans un fond au repos. La fluorescence planaire au laser (PLIF) est utilisée pour la visualisation des flux et pour quantifier les concentrations dans les sections transversales de jets turbulents avec des nombres de Reynolds de 5800 et 10600 pour x/d entre 20 et 70. Les données ont été post-traitées à l'aide des codes MATLAB.

La visualisation de l'écoulement montre que la section transversale du jet présente une plus grande variation de position et de forme lorsqu'elle est libérée dans une atmosphère turbulente, en raison des tourbillons plus larges de la turbulence qui déforment le trajet du jet et des tourbillons plus petits déformant la section transversale du jet. Les remous entraînent la rupture du jet (vitesse moyenne du jet nulle). La variabilité accrue du jet est visible dans les traces temporelles de la concentration dans l'axe. Les sections transversales des jets sont moyennées spatialement pour déterminer le taux de diminution de la concentration avec la distance axiale et le taux d'augmentation de la demi-largeur du jet. La concentration médiane normalisée varie avec la distance axiale normalisée x⁻¹ dans une ambiante au repos et x^{-1,7} pour le jet Re = 10600 et x^{-2,1} pour le jet Re = 5800 dans la turbulente ambiante. La moitié de jet normalisée varie avec une distance axiale normalisée x¹ dans une ambiante au repos et avec x^{1,2} pour le jet Re = 10600 et x^{1,4} pour le jet Re = 5800 dans une ambiante turbulente. La position du centre de gravité des sections transversales des jets indique un plus grand méandre du trajet des jets avec la distance en aval (Re = 10600). Le rayon de giration du jet a été utilisé pour identifier la croissance en largeur de la section transversale indépendamment du méandre du trajet du jet. Le rayon de giration normalisé

du jet varie x^{1,8} pour le jet libéré à la fois dans des conditions d'ambiante au repos et turbulentes, mais la magnitude était plus grande dans les conditions de turbulence ambiante, avec une augmentation plus importante dans les jets à faible nombre de Reynolds. L'évolution en aval du facteur de forme de la section transversale a également indiqué une perturbation plus importante de la section transversale plus proche de la sortie du jet dans l'ambiante turbulente. Enfin, la décroissance de la concentration médiane avec distance en aval a été comparée à celle de la vitesse et s'est révélée décroître plus progressivement dans l'ambiante En résumé, la turbulence dans une ambiante brise progressivement la structure du jet et déforme le trajet du jet. Cela se traduit par un taux de désintégration plus rapide du jet, qui est supérieur pour les jets avec un nombre de Reynolds inférieur.

Acknowledgements

Initially, I wish to express my sincere gratitude to my supervisor Prof. Susan Gaskin for her continuous support, patience and motivation during my studying at McGill University.

I am thankful Mr. John Bartczak for his help during the assembly of the experimental setup. I really appreciate the help of Dr. William Cook and Mr. Jorge Sayat with the who were very helpful with the electronics and computer problems.

I should express my gratitude to one of the major influencers of my life, Professor Gholamreza Rakhshandeheoo at Shiraz University, who changed my educational attitude and taught me principles of scientific research.

Finally, I would like to express my heartfelt gratitude to my family for their motivation, patient and confidence.

Table of contents

Abstractii
Résuméiv
Acknowledgementsvi
Table of contentsvii
List of figures
List of tables xiii
Nomenclaturexiv
Chapter 1: Introduction1
1.1 Background1
1.2 Thesis Structure
Chapter 2: Theoretical concepts and literature review
2.1 Passive scalar mixing within turbulent flows
2.2 Entrainment phenomenon and mixing in turbulent jets
2.3 Homogeneous isotropic turbulence in the laboratory
2.4 Effects of background turbulence on turbulent flows
2.4.1 Boundary layers and wakes in external turbulent flows
2.4.2 Jets and plumes in a turbulent background
2.5 Planar Laser induced fluorescence (PLIF) technique
Chapter 3: Experimental methods
3.1 Experimental facility29

3.2 Background conditions	29
3.3 Turbulent jet apparatus	33
3.4 Planar Laser induced fluorescence (PLIF) apparatus	36
3.5 Data acquisition and post-processing	44
3.6 Calibration Procedure	45
3.7 Reduction of potential sources of error	47
Chapter 4: Validation of concentration measurements	49
Chapter 5: Results	52
5.1 Passive scalar dynamics	52
5.1.1 Centerline concentration time tracings	54
5.1.2 Mean centerline concentrations	56
5.1.3 Mean radial concentration profiles	60
5.1.4 Half-width of the mean concentration profile	64
5.1.5 Cross-sectional center of mass	66
5.1.6 Cross-sectional radius of gyration	68
5.1.7 Cross-sectional shape factor	70
5.2 Comparison of the velocity and concentration fields comparison	71
Chapter 6: Conclusions	76
References	78

List of figures

Figure 3.1 Glass tank structure
Figure 3.2 Dimensions of the RJA, glass tank, and the jet setup. a) side view. b) front view30
Figure 3.3 Random jet array bilge pumps and their components
Figure 3.4 Front view of random jet array and jet in the glass tank
Figure 3.5 Constant head supply of dyed water to the jet (not to scale)
Figure 3.6 [a] horizontally and [b] vertically leveled jet and its distance from the RJA plane35
Figure 3.7 Traversing mechanism setup and its components
Figure 3.8 Schematic of the planar LIF system, top-view (not to scale)
Figure 3.9 Operation of the directing mirrors and the laser scanning device
Figure 3.10 Components of the laser beam scanning device
Figure 3.11 Coincidence of the jet tip with the generated laser sheet
Figure 3.12 Signal collecting system components
Figure 3.13 Schematic of the signal intensification procedure
Figure 3.14 Coincidence of the centers of the jet and image. a) Without jet. b) With jet
Figure 3.15 Location of the calibration box in the tank. a) Top view. b) Front view
Figure 3.16 Central and marginal calibration curves
Figure 4.1 Validation of normalised mean centreline concentration with axial distance for a turbulent jet
of Re=10600 of the present study with data from Law and Wang (2000) and Dahm and Dimotakis (1990)
50
Figure 4.2 Validation of the radial profiles of the mean concentrations of a turbulent jet from the present
study (Re=10600 at $x/D = 30$ and Re=5800 at $x/D = 70$) with data from Law and Wang (2000), Webster
et al. (2001), Fukushima et al. (2002), and Lavertu (2006)51

Figure 5.1 Average and instantaneous cross-sections of the turbulent jets (Re = 10600) issuing into a
quiescent background, and a turbulent background. [Colour map codes jet-fluid
concentration]53
Figure 5.2-Time traces of the centerline concentrations of the Re=10600 jet issued to the quiescent
ambient normalized by the averaged concentration $\binom{c_{cl}}{\bar{c}}$
Figure 5.3-Time traces of the centerline concentrations of the Re=10600 jet issued to the turbulent ambient
normalized by the averaged concentration $\binom{c_{cl}}{\bar{c}}$
Figure 5.4-Time traces of the centerline concentrations of the Re=5800 jet issued to the quiescent ambient
normalized by the averaged concentration $\binom{c_{cl}}{\bar{c}}$
Figure 5.5- Time traces of the centerline concentrations of the Re=5800 jet issued to the turbulent ambient
normalized by the averaged concentration $\binom{c_{cl}}{\bar{c}}$
Figure 5.6- Streamwise evolution of the normalized mean centerline concentrations (${}^{C_{cl}}/{}_{C_0}$) of the turbulent
jets with Reynolds numbers of 5800 and 10600 issuing into quiescent surroundings57
Figure 5.7- Streamwise evolution of the normalized mean centerline concentrations $\binom{C_{cl}}{C_0}$ of the turbulent
jet of Re=5800 issuing into both turbulent and quiescent ambient
Figure 5.8- Streamwise evolution of the normalized mean centerline concentrations $\binom{C_{cl}}{C_0}$ of the
Re=10600 turbulent jet issued into both turbulent and quiescent ambient
Figure 5.9 Streamwise evolution of the normalized mean centerline concentrations $\binom{C_{cl}}{C_0}$ of the Re=5800
turbulent jet issued into both turbulent and quiescent ambient. Best fit curve including point after breakup
[Re=5800 into turbulent ambient]59
Figure 5.10 Streamwise evolution of the normalized mean centerline concentrations $\binom{C_{cl}}{C_0}$ of the
·
Re=10600 turbulent jet issued into both turbulent and quiescent ambient. Best fit curve including point after breakup [Re=10600 into turbulent ambient]
oteakup [ke-10000 iiio tutoutent amotent]00
Figure 5.11 Radial profiles of mean concentration of the turbulent jet at Re=5800 (a) issuing into the
quiescent ambient and (b) issuing into the turbulent ambient. $[^{x}/_{D}^{=}$ 20, 30, 40, 50, and 60
respectively]

Figure 5.12 Radial profiles of mean concentration of the turbulent jet at Re=10600 (a) issuing into the
quiescent ambient and (b) issuing into the turbulent ambient. $[^{x}/_{D} = 30, 40, 50, 60, and 70]$
respectively]63
Figure 5.13a Downstream evolution of the half-width of the scalar field of the turbulent jet (Re = 10600
and Re = 5800) in turbulent and quiescent ambient65
Figure 5.13b Best fit curves of the half-width of the scalar field of the turbulent jet (Re = 10600 and Re =
5800) including anomalous furthest axial distances
Figure 5.14 Streamwise evolution of the radial position of the centre of mass of cross-sections of the scalar
field for a turbulent jet of Re =580067
Figure 5.15 Comparison of the center of mass position plots of (a) x/D=30 and (b) 60 of the Re=5800 jet
plotted as a line plot and as a scatter plot
Figure 5.16 Downstream evolution of the dimensionless radius of gyration of turbulent jets of Re = 10600
and 5800 issuing into quiescent and turbulent ambient69
Figure 5.17 Time traces of radius of gyrations of the jet of Re=5800 issued at the turbulent Background at
streamwise axial distances of x/D=40 and 50 (only covering the middle 25 sec
interval.)
Figure 5.18 Streamwise evolution of the cross-sectional shape factor of turbulent jets of Re=5800 and Re
= 10600 issuing into both quiescent and turbulent ambient
Figure 5.19 Linear regression relation between the mean centerline passive scalar and velocity fields of the
turbulent jet with the Reynolds number of 5800 [at streamwise normalized axial distances of 20, 30, 40, 50, 50, 50]
and 60 (quiescent ambient)]72
Figure 5.20 Linear regression relation between the mean centerline passive scalar and velocity fields of the
turbulent jet with the Reynolds number of 10600 [at streamwise normalized axial distances of 20, 30, 40,
50, 60, and 70 (quiescent ambient)]
Figure 5.21 comparison of mean centerline velocities and concentrations of the turbulent jet with Reynolds
number of 10600 subjected to the quiescent surrounding [at streamwise normalized axial distances of 20,
30, 40, 50, 60, and 70]73

Figure 5.22 comparison of mean centerline velocities and concentrations of the turbulent jet with Reynolds
number of 5800 subjected to the turbulent ambient [at streamwise normalized axial distances of 20, 30, 40
70, and 60]74
Figure 5.23 comparison of mean centerline velocities and concentrations of the turbulent jet with Reynolds
number of 10600 subjected to the turbulent ambient [at streamwise normalized axial distances of 30, 40
[0, 60, and 70]74

List of Tables

Table 5.1: Downstrea	m evolution of centreline mean concentration	60
Table 5.2: Decay con	stants for centreline mean velocity and concentration for	or the jet in quiescent
and turbulent ambient		75

Nomenclature

A area

 $(\mathcal{A}, \mathcal{B})$ calibration coefficients

C instantaneous concentration

 C_0 average jet exit concentration

c fluctuating concentration

D circular nozzle diameter

D molecular diffusivity

 d_0 waist diameter

f focal length

I fluorescence intensity

M molar concentration

 $Pe \text{ P\'eclet number} \equiv (Re*Sc)$

Pr Prandtl number $\equiv (v/\alpha)$

r jet radial coordinate

 $r_{1/2}$ jet half-width, radial coordinate where concentration decays by half of its centerline value

Re Reynolds number $\equiv (\frac{U_0*D}{v})$

Sc Schmidt number $\equiv (\nu/\mathcal{D})$

t time

U instantaneous axial velocity

 U_0 average jet exit velocity

u fluctuating velocity

x jet axial coordinate

 Z_R Rayleigh range

Chapter 1: Introduction

1.1 Background

Accurate estimation of the mixing of scalars occurring (at small scales) within a turbulent flow is essential in many industrial, environmental and natural applications. For example, many combustion systems are fed by a mixed flow of fuel and air and many sewage and drainage systems release pollutants into water bodies and rivers in the form of turbulent jets. For these cases, understanding scalar mixing processes in turbulent flows is an essential first step to be able to establish the intended mixing level for the optimization of combustion or to obtain the desired contaminant dilution to decrease the negative effects of the pollutant on the environment, respectively.

In real world situations, most environmental and industrial turbulent flows issue into turbulent surroundings, which modifies the entrainment and mixing processes as compared to those in a quiescent laboratory environment, thereby, complicating the predictions of turbulent jet behavior in such situations. The fluid dynamics of such flows are influenced by other external factors such as ambient density/thermal stratification, mean flow advection and boundary effects. Although the combination of these factors must be taken into consideration, an understanding of their individual effect on jet dynamics is required. The effect of the turbulent ambient can be determined from a comparison of the evolution of the turbulent jet in a turbulent ambient as compared to that in a quiescent ambient. Therefore, this study investigates the effect of a turbulent ambient on the scalar mixing of an axisymmetric turbulent jet.

The aim of the present study was to compare the passive scalar mixing behaviour of turbulent neutrally buoyant liquid phase axisymmetric jets with Reynolds numbers of 5800 and 10600 in a zero mean flow ambient with and without imposing a known approximately isotropic turbulence. These values of Reynolds number were chosen (following the decision in Khorsandi 2011 Perez-Alvarado 2016), to study two jets for which the effect of the ambient turbulence differed and whose break up could be observed in the measurement field. Re = 10600 was selected as the highest possible in our set up, while for the lower Re= 5800, breakup of the jet could be observed within our measurement field. The evolution of characteristic parameters with downstream distance (mean centreline concentration, time average radial profile, half-width, center of mass, radius of

gyration, shape factor) at the centerline and in cross-sections for axial distances between x/D = 10 and 70 were compared.

1.2 Thesis Structure

The remainder of the thesis is organized as follows. Chapter 2 presents a detailed chronological review of relevant literature, updating that presented in previous work from the laboratory on this subject by Khorsandi (2011) and Perez-Alvarado (2016). The review covers passive scalar mixing in turbulent jets, entrainment and mixing in a turbulent jet, the creation of isotropic turbulence in a laboratory setup, the effect of ambient turbulent on the turbulent flows of boundary layers, wakes, jets and plumes and, lastly, the planar laser induced fluorescence (PLIF) technique. In chapter 3, the experimental apparatus is described detailing the random jet array system, the jet setup and hydraulic system, the laser generating system, the laser scanning device and the signal collecting system. The experimental method is presented including the calibration procedure, the data acquisition and post processing procedures. In chapter 4, the validation of the experimental data is presented. In chapter 5, the results and statistics of the scalar field within the axisymmetric turbulent jets emitted into both quiescent and turbulent ambient are provided and discussed. Finally, in chapter 6, the conclusions of the present study are provided

Chapter 2: Theoretical concepts and literature review

A review of the topics relevant to the turbulent mixing of a passive scalar in a turbulent asixymmetric jet in a turbulent ambient are reviewed. These topics are passive scalar mixing in turbulent jets, entrainment and mixing in a turbulent jet, the creation of isotropic turbulence in a laboratory setup, the effect of ambient turbulent on the turbulent flows of boundary layers, wakes, jets and plumes and, lastly, the planar laser induce fluorescence (PLIF) technique. As this work is the continuation of a research program of over 10 years, this review is based on and updates the reviews presented in Khorsandi (2011) and Perez-Alvarado (2016).

2.1 Passive scalar mixing within turbulent flows

Turbulent jets are one of the most frequently occurring free shear flows in the environment and in industrial settings. Therefore, it has always been an active research area with many studies investigating the fluid dynamics of these flows. In the present study, steady-state, momentum-driven, liquid-phase, neutrally-buoyant, axisymmetric turbulent jets issuing into both quiescent and turbulent ambient are investigated to determine the effect of ambient turbulence on the scalar mixing in a jet.

An axisymmetric jet is a free shear flow whose mean momentum is in the axial direction, while it diffuses in its radial direction and has zero mean velocity in its azimuthal direction (i.e. no swirl). Since the radial gradients are greater than the axial gradients for a jet in a quiescent ambient, the boundary layer approximations can be applied to the Navier-Stokes equations (Pope, 2000). The continuity and axial momentum equations, after the application of the boundary layer approximations for this flow, are

$$\frac{\partial \langle U \rangle}{\partial x} + \frac{1}{r} \frac{\partial (r \langle U \rangle)}{\partial r} = 0 \tag{2.1}$$

$$\langle U \rangle \frac{\partial \langle U \rangle}{\partial x} + \langle V \rangle \frac{\partial \langle U \rangle}{\partial r} = \frac{v}{r} \frac{\partial}{\partial r} \left(r \frac{\partial \langle U \rangle}{\partial r} \right) - \frac{1}{r} \frac{\partial}{\partial r} \left(r \langle uv \rangle \right)$$
 (2.2)

where U and V denote the axial and radial velocities, respectively. x is the axial coordinate, r is radial coordinate, and u and v are the fluctuating axial and radial velocities. v represents the

kinematic viscosity, and $\langle \cdot \rangle$ denotes averaging. The mean pressure distribution has been estimated from the radial momentum equation and subsequently substituted in equation 2.2.

The velocity field of an axisymmetric jet released into quiescent surroundings has been rigorously investigated and its behavior is well established (Wygnanski and Fiedler 1969, Panchapakesan and Lumley 1993, Hussein, Capp et al. 1994; Xu and Antonia 2002, Lipari and Stansby 2011, Darisse, Lemay et al. 2015, and their references). The jet initially has a developing region after which it becomes self-similar and the axial mean velocity profile approaches a Gaussian distribution (Wygnanski and Fiedler 1969). The rate of decay of the centerline mean velocity of an axisymmetric turbulent jet in the self-similar region varies with x⁻¹ and the jet half-width, which is defined as the radial distance at which the mean axial velocity reduces to half of its centerline value, increases linearly with streamwise distance; i.e. varies with x¹. The Root Mean Square (RMS) of the velocity fluctuations become self-preserving farther downstream.

Turbulent flows are characterized by the existence of eddies having a continuous range of length scales the largest of which are determined by the flow's geometry, and the smallest of which are those at which the molecular diffusivity and viscosity overcome the concentration and velocity fluctuations (Tennekes et al. 1972). The small scales in turbulent flows were characterized by Kolmogorov through a famous theory that named after him (Kolmogorov 1941), Kolmogorov 1941). Kolmogorov's theory states that the smallest possible scale of the velocity field (the Kolmogorov scales), are those at which the turbulent kinetic energy is dissipated into the internal energy by viscous interactions, which depend solely on the kinematic viscosity (v) and the dissipation rate of turbulent kinetic energy per unit mass (ϵ). Thus, the Kolmogorov length scale has been defined as $\eta \equiv (v^3/\epsilon)^{1/4}$. The Kolmogorov theory predicts a -5/3 power law region of the energy spectrum in the inertial subrange, which occurs between the largest scales and the Kolmogorov scales, where viscosity and large-scale effects can be considered negligible.

Furthermore, to quantify the diffusivity of the scalar fields, the Schmidt number (Sc=v/D) is used to define the ratio of viscous forces to diffusion, where D represents the molecular diffusivity of the scalar in a given fluid. It quantifies the smallest (dissipative) scales of a scalar field. Using a similar line of reasoning to that used by Kolmogorov, Corrsin (1951) defined the smallest scales of a scalar field for Sc<<1 as $\eta_{\theta} = (D^3/\epsilon)^{1/4} = \eta \text{Sc}^{-3/4}$. For gases the Schmidt number is low and the "Corrsin scale" (η_{θ}) should be equal to or larger than the Kolmogorov scale, and the spectra of the

scalar fluctuations exhibit a -5/3 power law region (similar to the velocity field) in the inertial-convective subrange, which occurs between the largest and the smallest (η_0) scales (Oboukhov 1949, Corrsin 1951). Later, Batchelor (1959) defined the smallest scales of the scalar field for cases where Sc>>1 as $\eta_B \equiv (vD^2/\epsilon) = \eta Sc^{-1/2}$, known as the "Batchelor scale," in his honor. For the case of scalars in liquids, Sc is much larger than one, and the Batchelor scale is smaller than the Kolmogorov scale. and two power law regions are defined for the spectra of the scalar fluctuations. First, an inertial-convective subrange, a -5/3 power law decay, occurs between the largest and the Kolmogorov scales and, second, the viscous-convective subrange, a -1 power law decay, occurs between the Kolmogorov and the Batchelor scales.

A passive scalar in a flow is defined as a non-reactive, dynamically-neutral contaminant whose presence does not affect any dynamical characteristics of the carrying fluid. The transport of a passive scalar (C) through a non-reacting flow is governed by the advection- diffusion equation as follows.

$$\frac{\partial C}{\partial t} + u_i \frac{\partial C}{\partial x_i} = D \frac{\partial^2 C}{\partial x_i \partial x_i}$$
(2.3)

where C denotes the concentration of the passive scalar, t represents the time, u_i is the velocity in the i direction and D is the molecular diffusivity of the passive scalar. A nondimensionalized equation of the normalized concentration can be obtained by introducing a set of nondimensional variables of C*=C/C_o, t*=U_jt/D, u_i *= u_i /U_j, and x_i *= x_i /D, where C_o the initial concentration, U_j denotes the initial velocity and D corresponds the nozzle's diameter. The non-dimensional expression of the advection-diffusion equation is thus:

$$\frac{\partial C^*}{\partial t^*} + u_i^* \frac{\partial C^*}{\partial x_i^*} = \frac{1}{\text{Re } Sc} \frac{\partial^2 C^*}{\partial x_i^* \partial x_i^*}$$
(2.4)

where $Re=U_jD/v$ and Sc=v/D represent the Reynolds and Schmidt numbers, respectively. Therefore, the evolution of the normalized scalar concentration depends on the Péclet number, which is defined as the product of the Reynolds and Schmidt numbers (Pe=ReSc).

Extensive experimental studies of the scalar field of turbulent flows have been conducted regarding the dispersion of jets released into quiescent surroundings. A range of approaches and experimental conditions were employed, however most, were unable to resolve the smallest scales

(Batchelor scale). A brief review of some of the most important studies investigating the scalar field in turbulent flows is provided. Starting with the studies on passive scalars in plumes and confined jets, those on the passive scalars advected by turbulent jets in a quiescent surrounding following.

Gibson and Schwarz (1963) studied the decay of a random homogeneous passive scalar as a temperature field using a single-electrode conductivity probe in a bridge circuit. When temperature is treated as passive scalar, the Prandtl number ($Pr=v/\alpha$) becomes is used to define the ratio between viscosity and thermal diffusivity. The velocity field was detected by means of a Lintronic constant-temperature hot-film anemometer. Compatible results with predictions of universal similarity and the local isotropy theories were achieved. results consistent with Batchelor's predicted spectrum for the scalar field was reported.

Wilson and Danckwerts (1964) measured the temperature in a hot air jet ($Pr \sim 1$) using a resistance-thermometer, for Reynolds numbers between 2×10^4 to 4×10^4 . The axial mean temperature evolution and the half-width of the scalar profiles were found to follow the x^{-1} rate of decay and x^1 rate of increase, respectively. The mean radial profile of the temperature was well estimated by a Gaussian distribution, demonstrating self-similarity after a streamwise distance of x/D = 20 (where D is the nozzle's diameter). While the profile of the temperature fluctuations was found to be self-similar after a normalized streamwise distance of 40.

Becker, et al. (1967) developed a novel light-scattering technique for concentration measurement of a free air jet of Re=54000, using smoke as the tracer (Sc~38000). At the centerline, the concentration power spectra exhibited a -5/3 power region, as expected by the Kolmogorov approximation. However, a k⁻¹ region was not identified due to the inadequate spatial resolution of the technique, which was unable to resolve the smallest scales.

Concentration measurements in a methane jet (Re=1600 and Sc \sim 1) were performed by Birch, et al. (1978). Raman scattering of laser light was employed to observe the flow behavior. Higher RMS concentration fluctuations and peak of radial RMS concentration were observed for the methane jet as compared to the hot air jet. The Gaussian profile of the centerline concentration pdf became self-preserving at a non-dimensional streamwise distance of x/D=20.

Lockwood and Moneib (1980) examined the temperature fluctuations of a heated inert round free jet for Re= 5×10^4 , using a thermocouple. The centerline intensity of the temperature fluctuations was observed to approach a constant value at x/D = 40. The radial profile of the temperature intensities suggested that the maximum values correspond to those of the largest gradients of the mean temperature profile.

In order to investigate buoyancy effects, Panchapakesan and Lumley (1993) and Panchapakesan and Lumley (1993) simultaneously measured the concentration and velocity fields of two air and helium jets (Sc~0.7) discharging into air. A composite hot-wire/concentration probe closely observed the transition region between the non-buoyant jet and the plume region ($50 \le \frac{x}{D} \le 120$). A wider mean concentration profile for the helium jet as compared to the pure air jet was obtained in addition to a higher axial RMS of the velocity fluctuations in the helium jet than in the air jet, confirming the effect of the additional buoyancy.

Quantitative point measurements and a qualitative planar Mie scattering flow-visualization technique were utilized by Mi et al. (2001) to assess the velocity and scalar (i.e. temperature) field characteristics. A normalized axial distance range of 0 to 70 of a slightly heated air jet at a Reynolds number of 16,000 was investigated. Two different exit conditions were considered, a smooth contraction nozzle producing a 'top-hat' velocity profile and a long straight pipe generating a jet with fully developed pipe turbulence. The results revealed that the turbulent scalar properties of the jet were analogous to the findings of George (1989) for the zone of the flow dominated by its initial condition. The rate of decay of the centerline mean scalar profile was reported to be larger for the jet discharged from the smooth contraction than that of the jet from the long pipe in both the near and far fields. It was suggested that the differences in the underlying turbulence structure of the jet in the near field might cause the difference in the scalar field statistics.

Darisse et al. (2015) conducted experiments for simultaneous measurements of velocity and concentration for a free round turbulent air jet. Point measurements of laser Doppler velocimetry and cold-wire thermometry were used in the near-field (x/D=30) of a turbulent jet of Re = 140 000. It was observed that slightly heating the jet leads the temperature to behave as a passive scalar. Results demonstrated good agreement with the established profiles of (mean and RMS) concentration and velocity.

High Schmidt number liquid-phase turbulent jets have also been extensively investigated. The laser-induced fluorescence (LIF) measurement technique has been used to measure concentration in many studies and, as a planar observation technique, has allowed for flow visualization. The study of Dahm and Dimotakis (1990) obtained the concentration distribution in the self-similar region of a steady, axisymmetric, free liquid-phase turbulent jet issuing into a quiescent ambient. The jet Reynolds numbers were between 1500 to 20000 and disodium fluorescein (Sc~2000) was used as the passive scalar. Turbulent transport and molecular mixing within a normalized axial distance $0 \le x/D \le 350$ were observed. Large regions of high concentration fluid separated by unmixed fluid were seen, confirming the presence of a large-scale organization in the jet far-field (Dahm and Dimotakis, 1987). Time traces of concentration at the centerline revealed that less streamwise mixing occurs with increasing Reynolds number.

Furthermore, Dowling and Dimotakis (1990) reported a relatively comprehensive study of the scalar transport in turbulent gas phase jets with Reynolds numbers of 5000, 16000, and 40000. The experiments were conducted using Rayleigh scattering to measure the scalar field. The resolution of the apparatus was able to capture the smallest scales for the Reynolds numbers of 5000 and 16000 but not for 40000. Wider radial profiles of RMS temperature fluctuations were obtained at the higher Reynolds numbers. An identical trend was observed in the water jet results of Dahm and Dimotakis (1990). The pdfs of concentration fluctuations indicated full mixing on the jet axis, which was in contrast with the results (Dahm and Dimotakis 1990) at higher Schmidt numbers.

Subsequently, Miller and Dimotakis (1991) studied the centerline scalar concentration fluctuations of a high-Schmidt-number turbulent jet using point LIF. The dye used was sodium fluorescein (Sc~10³), and the jet Reynolds numbers ranged from 3,000 to 24,000. An inverse relationship between the normalized RMS scalar fluctuations and the Reynolds number was obtained. The pdf of the concentration and the shape of the normalized scalar power spectra appeared to be Reynolds number dependent, in contrast to the low Schmidt number flows. Although, the measurements were fully spatially resolved for this range of Reynolds numbers, no k⁻¹ region was reported in the scalar power spectra.

Yoda et al. (1994) studied the concentration field in water jets with Reynolds numbers of 1000 to 4000, by means of the planar laser-induced fluorescence (PLIF) measurement technique and using

disodium fluorescein (Sc~2000) as the passive scalar. Although, the experiments could not resolve beyond the Kolmogorov microscales, roughly axisymmetric regions of large concentration gradient were found situated near the jet axis, corresponding to the basic structure of fine-scale passive scalar mixing.

Dispersion and mixing of a passive scalar in a turbulent jets of Re=2800 to 18000 were investigated by Tong and Warhaft (1995). Temperature fluctuations were induced through the self-similar region of the jet by using heated axisymmetric fine wire rings. It was reported that approximately 1.5 times the eddy turnover time was required for the intense local thermal field to fill the whole jet close to the ring. The evolution of the cross-correlation coefficient, ρ , and the segregation parameter, α , reached asymptotic values also in about 1.5 eddy turnover times. This was in contrast to the mixing and dispersion in grid turbulence, where the evolution process was reported to be slower. Moreover, a strong dependence on the measurement location as well as the direction of derivatives was found associated to the far field measurements.

A comprehensive study on the scalar power spectra in a turbulent water jet was conducted by Miller and Dimotakis (1996). In this study, the Reynolds number varied between 12 500 to 72 000, while, the centerline measurements were performed by means of a point laser induced fluorescence setup with the passive scalar of disodium fluorescein (Sc~2000). The experiments had an improved spatial resolution, however their order of magnitude remained larger than the Batchelor scale. The spectra at different downstream locations varied with Reynolds number, however, the k⁻¹ region in the spectra was not reported. The spectra's similarity with the high-frequency/wavenumber prediction of Batchelor (1959) was found at high Reynolds.

Separately, Catrakis and Dimotakis (1996) obtained cross sections of the disodium fluorescence passive scalar field and iso-concentration surfaces in turbulent water jets for Reynolds numbers of 4500 to 18 000. The two-dimensional concentration profile, radial scalar power spectra, as well as the pdfs of the concentration fluctuations were found to be Reynolds number dependent at low Reynolds numbers. A mixing transition was found to occur within the range of Reynolds numbers studied.

Round, turbulent, unsteady jets were studied by Johari and Paduano (1997) using the LIF technique. A dyed fluid was vertically released into a large water tank using gravity driven flow. The jet velocity followed a continuous increase and then a subsequent decrease between zero and

the maximum velocity. The line integral of concentration across the jet diameter was calculated to study the jet dilution. It was reported that the unsteady deceleration phase contributes more to dilution in comparison to the steady phase. Moreover, the observation of the molecular scale mixing, offered that the unsteady jet mixed in a shorter distance than the steady jet.

Dimotakis (2000) explained the mixing transition as a universal turbulent phenomenon for different shear flows, including turbulent jets. Negligible Reynolds number dependence was observed for the flow statistics above a certain value. A transition to a better mixed state was observed to occur above a minimum Reynolds number. a universal Reynolds number of 10⁴ was proposed as the lower bound of fully-developed turbulent flow.

Su and Clemens (2003) investigated the fine-scale scalar mixing in a gas-phase jet via simultaneous planar Rayleigh scattering and planar laser induced fluorescence (PLIF) that was performed in parallel planes for a Reynolds number range of 3290 to 8330. Consistent results with that of Buch and Dahm (1996) in a water jet were reported in terms of scalar dissipation rate, which was later indicated in a review by Antonia and Orlandi (2003) on the behavior of passive scalars with different Schmidt numbers.

Burattini and Djenidi (2004) performed simultaneous velocity and passive scalar (temperature) measurements in the near field of a round jet with and without obstructing grids placed at the nozzle's exit. The Reynolds number was 4.9×10^4 and the flow was incompressible. The obstructed jet was observed to maintain higher attenuated streamwise and radial concentrations in comparison to the unobstructed jet. In the near field, the spatial similarity of the moments of velocity fluctuations was improved for the perturbed jet.

Soltys and Crimaldi (2015) employed a two-channel planar laser-induced fluorescence (PLIF) system to investigate the instantaneous spatial structure of two initially separated scalars discharged from parallel jets. A weak coflow of 0.37 cm s⁻¹ with less than 2 % of the mean jet velocity of the lower Reynolds number, was imposed to prevent the accumulation of jet fluid, while the coflow had negligible effects on the jet structure within the test section (Nickels and Perry 1996). Therefore, the flow was considered as a jet in quiescent surrounding. Joint probability distribution functions (JPDFs) and instantaneous images of the scalar field revealed the existence of incursions of fluid between the two jets at near axial distances, before scalar mixing occurred.

Nironi, et al. (2015) studied the source configuration effects on dispersion process of a passive scalar. Size, elevation, and the emission velocity were the parameters of interest of this study. Results provided the estimations of intermittency factors, which proposed the main controlling mechanisms of the scalar dispersion and associated form of the PDF. Moreover, a detailed description of the velocity statistics was discussed, including direct estimates of the Eulerian integral length scales from two-point correlations.

Temporal development of scalar dispersion in an isothermal impulsively started gas-phase jet was quantified by Soulopoulos, et al. (2015). By means of a PLIF apparatus, it was possible to obtain the measurements of the concentration field of acetone across a plane encompassing the nozzle centerline. The probability density functions of the mixture fraction and scalar dissipation rate were analyzed based on different axial downstream distances and time intervals after the ignition. Moreover, regions at the edge of the jet and the developing vortex ring were identified as high mixing zones based on data from instantaneous distributions of the scalar dissipation rate.

Kravtsov, et al. (2016) studied the passive scalar transport in the near-field of a submerged turbulent gas-phase jet via PLIF technique. The jet was issued from a round pipe with Reynolds numbers of 3000, 6000, and 9000, while, the vapor of acetone served as the passive scalar. The average concentration profiles in the near field of the jets were to be independent of the Reynolds number. Nevertheless, it was reported that the fluctuation's amplitude of concentration depends on the Reynolds number within the mixing layer.

Kothnur and Clemens (2005) carried out an analysis of previously acquired experimental data to develop a relationship between strain rate and scalar dissipation rate structures in gas-phase turbulent planar jet flows. Simultaneous measurements of two-dimensional velocity and conserved scalar fields were analyzed for jets with local Reynolds numbers between 1000 to 6100. The spatially resolved data showed nearly Gaussian profiles of scalar dissipation, taken across the sheet-like scalar dissipation structures, and satisfactory agreement was revealed with a simple one-dimensional unsteady strained laminar diffusion-layer model.

Feng, et al. (2006) utilized simultaneous particle image velocimetry (PTV) and PLIF techniques to investigate the turbulent mixing in a confined rectangular jet. The Reynolds number based on hydraulic diameter was 50000, while, the passive scalar had a Schmidt number of 1250. Therefore, velocities conditioned on the basis of the scalar concentration were evaluated. Due to the confined

geometry, and the non-Gaussian profile of the PDFs, the conditional mean velocity fit a linear model only when the mixture fraction was close to the local mean mixture fraction. A gradient PDF model was suggested for the conditional velocity, which compared well to the experimental data. The model gave good predictions of cross stream conditional velocity. However, the predictions for the streamwise conditional velocity were poor.

An efficient experimental method for simultaneous measurements of instantaneous vector and scalar fields, LIF-PTV (particle-tracking velocimetry) method, was employed by Webster, Roberts et al. (2001) in a turbulent jet with a Reynolds number of 3000. Rhodamine 6G and Titanium dioxide were used as the passive scalar and flow tracer, respectively. An excellent agreement was observed with the results of previous point velocity and concentration measurements. The profiles of mean velocity, turbulent stresses, mean concentration, concentration variance, and turbulent flux of tracer were observed to follow the self-similar profiles in the far field of the jet very well. The functionality of the system in measuring the velocity and concentration distributions and turbulent characteristics was extensively discussed. Moreover, several studies have recently discussed the advantages of this experimental method (Cowen, et al. 2001, Romano 2002, Krug, et al. 2014).

Romano (2002) detected the spanwise and streamwise vortices in the near field of axisymmetric water jets within the Reynolds number range of 1000 to 10000. Laser-induced fluorescence, laser Doppler anemometry and particle tracking velocimetry were used for the experiments. No-slip and free-slip conditions were examined at the nozzle outlet, and the subsequent effects on the generation, growth and interaction of large vorticial structures were investigated. For the free-slip jet, the vorticial structures developed more gradually and closer to the nozzle as compared to the no-slip jet, with higher local mixing for the free-slip case. Moreover, a slower rate of decrease for velocity field, a longer potential core and a higher shear layer (momentum) thickness were reported for the free-slip conditions.

Law and Wang (2000) applied Particle Image Velocimetry coupled with LIF to capture the vector-scalar fields in turbulent water jets with a Reynolds number of 12700 and a high Schmidt Number passive scalar (Sc~3,000). Despite the reported inadequate spatial and temporal resolution of the cameras and data acquisition system, the agreement of the mean concentration and velocity profiles with previous studies was satisfactory although, differences in the turbulent intensities

were observed. The efficiency of this method as a powerful means of velocity-concentration measurements was later proven by several subsequent studies (Fukushima, et al. 2002, Funatani, et al. 2004 Westerweel, et al. 2005, Peterson, et al. 2013, Wen, et al. 2018).

Fukushima, et al. (2002) studied the mixing of a passive scalar in a self-preserving axisymmetric turbulent jet with Reynolds number of 2000. Combined PIV-LIF was utilized for measurements of the mean velocity, turbulent intensity of velocity fluctuations, Reynolds shear stress, mean concentration, concentration fluctuation intensity, and turbulent flux at the center plane of the jet. All the properties were reported to follow a self-similarity pattern in the far field of the jet, and were validated with the results from direct numerical simulation, point velocity measurements, and combined PIV, PTV, or laser Doppler velocimetry (LDV) and LIF measurements (e.g. Panchapakesan and Lumley (1993), Aanen, Telesca et al. (1999), Webster, Roberts et al. (2001), Lubbers, Brethouwer et al. (2001)).

Coupled velocity and concentration measurements of low Reynolds numbers neutrally-buoyant turbulent round jets were performed by Zarruk and Cowen (2008). Far field ($60 \le x/D \le 80$) characteristics of the jet flow with two Reynolds numbers of 1500 and 4000 were studied using PIV-LIF apparatus. Based on the reports, the centerline velocity decay constant increased with Reynolds number and the virtual origin moved farther from the nozzle exit. However, the scalar concentration decay coefficient in addition to the scalar field's virtual origin were found to be independent of the Reynolds number. A self-similar behavior was reported for the centerline turbulent intensities beyond $x/D \approx 75$. Nevertheless, the scalar fluctuations were strongly Reynolds number dependent, increasing with the enhanced entrainment of ambient flow on the jet axis at lower Reynolds number. A Reynolds number dependency was reported for scalar fluxes as well. Consequently, the turbulent Schmidt number was estimated to decrease with the decreasing Reynolds number.

The coupled PIV-LIF technique was employed by Mistry and Dawson (2014) to study the entrainment process in the far-field of a round turbulent jet. The flow Reynolds number was set at 25300 with $Re_{\lambda} \approx 360$ based on the nozzle diameter and Taylor microscale, respectively. A negligibly diffusive dye (Sc \gg 1) enabled precise measurements of the concentration field. Self-similarity was observed in the far field. Moreover, the centerline velocity decay constant as well as the jet's half-width agreed with theoretical predictions. It was concluded that for a range of

scalar thresholds, a constant ratio exists between the instantaneous and averaged interfacial surface areas, analogous to axial distance from the jet core.

2.2 Entrainment phenomenon and mixing in turbulent jets

Theoretically for incompressible turbulent jets, the jet width should increase with axial distance due to the inclusion of ambient fluid to the mean flow of the jet. The ambient fluid becomes turbulent in the case of turbulent jets. The multi-scale process of drawing surrounding fluid into the jet is termed entrainment. A hypothesis first introduced by Morton, et al. (1956) related the increase in jet mass flow to an entrainment velocity (V_e) normal to the surface of the jet boundary, and proportional to a characteristic velocity (u_m) at each distance along the jet axis ($V_e = \alpha u_m$). The centerline velocity is the local characteristic velocity at a given downstream position, and α is a constant of proportionality known as the entrainment coefficient. From experimental records, the accepted value of the entrainment coefficient (α) for jets is 0.0535 (Fischer, List et al. 2013). Although, the correlation between the entrainment velocity and mean axial velocity was proposed by the entrainment hypothesis, it does not provide any information about the mechanism of entrainment.

Despite the numerous studies investigating the entrainment phenomenon, the mechanism of entrainment is still under examination. Two principal hypotheses explaining the entrainment mechanisms, attribute important entrainment processes to different scales. The equilibrium hypothesis proposed by Townsend (1966) explains the entrainment as a cyclic process in which large coherent structures (i.e. eddies) engulf large volumes of ambient fluid. Thus, the large-scale eddies are the main mechanisms of the entrainment process. On the other hand, the superlayer hypothesis (Corrsin and Kistler (1955) asserts that the transformation of ambient fluid to turbulent flow occurs across a thin layer, separating the ambient and turbulent flow, by the viscous interactions between the small scales, which is termed 'nibbling'. Various experiments have been conducted to cast insight on the importance of the different scales associated with the entrainment process.

Several papers support the position that the equilibrium hypothesis is the dominant entrainment mechanism (Yule 1978, Long, et al. 1981, Dahm and Dimotakis 1987, and Shlien 1987), while, several others support the position that the superlayer hypothesis is the dominant mechanism

(Mathew and Basu 2002, Westerweel, Fukushima et al. 2005, and Wolf, et al. 2012) of entrainment and mixing within the turbulent flows.

An extensive review of turbulent mixing was reported by Dimotakis (2005). The mechanism of fluid mixing at the molecular scale as an important feature of the turbulent flows was discussed for a considerable number of experimental, theoretical, modeling, and computational work. It was argued that for high Reynolds number flows, turbulent mixing occurs across a wide spectrum of scales.

Westerweel, et al. (2009) used PIV for conditional sampling measurements in the far field (60 \leq $\chi^2/D \le 100$) of a turbulent round submerged liquid jet with Reynolds number of 2000. The dynamics and transport processes were investigated at the interface of the turbulent and nonturbulent regions of flow, termed as the Turbulent Non-Turbulent Interface (TNTI). The fluctuating turbulent jet interface was detected using the LIF technique with a high Schmidt number dye (Sc~2,000) to assess the concentration field. Distinct discontinuities were observed at the interface of the TNTI zone in the mean axial velocity and mean scalar profile, and the mean vorticity tended towards a singularity. Consistent with the works of Mathew and Basu (2002), and Hunt, Eames et al. (2008), the results suggested a much higher contribution of small-scale mixing (nibbling) rather than the large-scale engulfment (less than 10%) in the entrainment process of a jet flow (without forcing). This agreed well with the highly mixed concentration field in the interior of the jet. Theoretical support to explain the different dominant entrainment mechanisms in jets and wakes compared with those of free shear layers was proposed. The local eddy viscosity and eddy diffusivity were used to describe the difference between the velocity and scalar fields of the jet. Due to the higher values of eddy diffusivity compared to those of the eddy viscosity, flatter profiles for concentration were obtained at the interface, which suggests greater discontinuity in scalar field than in the mean velocity profile.

Mistry, et al. (2016) observed the entrainment process across the turbulent/non-turbulent interface for $40 \le x/D \le 60$ of an axisymmetric turbulent jet. Time-resolved particle image velocimetry and planar laser-induced fluorescence methods were implemented for interface identification across the turbulent and non-turbulent zones of a high Reynolds number jet. Applying spatial-filtering methods with various filter sizes, confirmed the power-law behavior of the mean length of the TNTI. A multi-scale methodology was proposed from whose results, it was

declared that the mean mass flux, i.e. the product of the entrainment velocity and the surface area, remained constant for a known range of filter sizes. In agreement with results of Meneveau and Sreenivasan (1990), the entrainment velocity along the TNTI followed a power-law profile, increasing with the filter size. It supports the fact that mean entrainment velocity balanced the scaling of TNTI length in a way that the mass flux remained independent of the coarse-grain filter size. Therefore, at the smallest scales, the entrainment velocity reaches its minimum values, and is explained by the presence of a very large surface area. While, at the largest scales, the large entrainment velocity is balanced by a smaller (smoother) surface area.

Carlier and Sodjavi (2016) employed a single x-wire probe thermo-anemometry technique to obtain the coupled velocity–temperature fields at high frequency. A stratified plane shear layer between two horizontal air flows with low Richardson number (Ri_{max}= 0.02) was explored for the effect of buoyancy on the turbulent mixing and entrainment processes. To distinguish between the different driving mechanisms in turbulent mixing (namely entrainment, engulfing, nibbling and mixing), probability density functions as well as the joint probability density functions (JPDFs) were examined. Applying a temperature thresholding method enabled the distinction between the unmixed fluid entrained from the hot and cold sides of the mixing layer into the mixing layer. Consistent with the prediction by the Dimotakis model (Dimotakis 1986), it was hypothesized that the model could be further developed by considering the individual contributions of the nibbling and engulfment within the process of entrainment and mixing.

Vanderwel and Tavoularis (2016) experimentally studied a passive scalar plume released in a uniformly sheared turbulent flow to investigate the role of coherent structures in scalar dispersion. Stereo particle image velocimetry and planar laser-induced fluorescence were applied to measure the velocity and concentration fields. Hairpin vortices were generated in flow to study the effects of coherent structures on turbulent dispersion. It was observed that the fluorescent dye tended to move far away from the vortices because of high dissipation at the periphery of the vorticial structures. Additionally, a more complicated correlation between the uniform momentum zones, the locations of vortices, and dye transport was reported. The presence of vortices was found to be the reason for the large scalar fluxes and large Reynolds stress events in the flow. The fact that the Reynolds stress was not correlated with the scalar flux, further supported the dominant role of coherent structures in scalar transport in plumes.

Burridge, et al. (2017) used the coupled two-dimensional PIV-LIF measurement techniques to assess the central vertical plane in an axisymmetric pure turbulent, high Péclet number plume. An edge-detection method characterized the edge of the plume, in both a fixed Eulerian frame and a frame relative to the instantaneous plume edge. The self-similarity of the time-averaged vertical and horizontal velocities, and Gaussian distribution in the vertical velocity were evident in a Eulerian frame. Compression of the slightly larger fluxes of engulfed fluid within the plume to the vertical transport outside the plume, revealed that the engulfment of ambient fluid preceded the nibbling across turbulent/non-turbulent interface, before the ultimate and irreversible mixing into the ambient flow. Finally, it was suggested that unlike the significant vertical velocities beyond the scalar edge of the plume, the characteristic width of the velocity profile was not greater than that of the scalar field. Moreover, the buoyancy distribution was shown to be up to 20 % wider than that of the velocity.

Mistry, et al. (2018) implemented the PIV-LIF techniques to characterize the mixing and geometric evolution of the turbulent/non-turbulent interface in the near-field of an axisymmetric turbulent jet that was discharged into a water tank with a Reynolds number of 24000. The near field of the jet, $0 \le x/D \le 6.8$ was visualized using Rhodamine 6G as the passive scalar. Thereafter, the multiscale nature of the TNTI was monitored, and it was reported that the fractal scaling of the interface in the far field of an axisymmetric jet, was initiated at the end of the potential core.

Recently, Kabanshi, et al. (2018) presented the fundamental aspects of axisymmetric free jets and entrainment in ventilation applications. Two jets with Reynolds numbers of 2540 and 4760 in the range of streamwise axial distances of $0 \le x/D \le 5$ were experimentally investigated. Subsequently, significant differences were reported in comparison to previous research (such as Mi, et al. 2001, and Trabold, et al. 1987) based on the shape of velocity and temperature profiles, as well as the level of entrainment. A Reynolds number dependency was reported for the entrainment process, particularly, at the end of this downstream range. However, further studies will be required to reconcile these results with results reported earlier.

2.3 Homogeneous isotropic turbulence in the laboratory

In a general sense, turbulent flows should be neither homogeneous nor isotropic. However, the study of homogeneous isotropic turbulence can play a fundamental role in further understanding

the physics of turbulent flows in real applications. Such an assumption could isolate the self-interaction of turbulent fluctuations (Orszag 1974), while it prevents complications encountered in natural and man-made flows, such as stratification, mean shear and the effects of fluid-solid boundaries (Tsinober 2001). Moreover, studying homogeneous isotropic turbulent flows can help to analyze the fundamental properties and mechanisms of turbulence (e.g. internal intermittency, spectral energy transfer). Even though homogeneous isotropic turbulence can be seen as a (relatively) simple flow, it is difficult to generate and control in the laboratory, as mean velocity gradients are necessary for the initial production of turbulent kinetic energy.

Sseveral methods have been proposed for generating homogeneous isotropic turbulent flows. Gridgenerated wind tunnel turbulence is the most common approach, which can develop relatively high Reynolds numbers. Either using active grids (Mydlarski and Warhaft 1996), or low-viscosity-fluid wind tunnels (Bodenschatz, et al. 2014), however, the existence of a mean flow may lead to problematic circumstances, such as difficult recognition of the mean flow and turbulent fluctuations effects in Lagrangian measurements. Using zero-mean-flow turbulence reduces the experimental error sources. There are several methods for generating zero-mean-flow turbulence, such as one, or two parallel grids oscillating in a direction normal to the plane of the grids (Thompson and Turner 1975, Villermaux, et al. 1995, McKenna and McGillis2004, and Blum, et al. 2011). However, this system suffers from large mean flows.

An alternative approach to generating nearly zero-mean-flow homogeneous isotropic turbulence is to place loudspeakers pointing towards the center of a chamber (Webster, et al. 2004, Goepfert, et al. 2010, and Chang, et al. 2012), placed with respect to the symmetry of the chamber. Vortex rings pushing through the circular orifices are the main deficiency of this system. Although negligible mean flows result, the desired isotropic flow is confined to a very small region in the center of the chamber.

Rotating grids (Liu, et al. 1999) as well as propellers (Berg, et al. 2006) also have been employed to create homogeneous isotropic turbulent flows. However, the levels of turbulence were relatively low (Re $_{\lambda} \sim 290$ and 172, respectively) and the isotropic flow was limited to a small volume. Although two counter-rotating disks in cylindrical containers applied in the works of Douady, et al. (1991), Belin, et al. (1997) and Voth, et al. (2002) could solve the low turbulence intensities, it still suffers from anisotropy.

Random jet arrays (RJA) are a relatively acceptable technique for generating approximately homogeneous isotropic turbulence with zero mean flow (Variano et al. 2004, Lavertu et al. 2008, Variano and Cowen 2008, Khorsandi et al. 2013, Bellani and Variano 2014, and Pérez-Alvarado, et al. 2016). A single RJA is a planar configuration of jets that, randomly and independently, turn on and off to produce turbulence downstream of the array. A nearly homogenous flow is achieved in a plane parallel to the RJA which decays in the direction normal to the plane of the RJA having a negligible mean flow of less than 10% of the RMS velocities in all directions over a large spatial zone (Variano and Cowen 2008). The flow isotropy is of the same order as that of grid-generated, wind tunnel turbulence, and relatively high Reynolds numbers can be achieved (such as $Re_{\lambda} = 314$ in Variano and Cowen 2008). Two facing RJAs, used in the work of Bellani and Variano (2014), generated a nearly homogeneous isotropic turbulent flow with a negligible mean flow at the center of the tank. Flow isotropy was significantly improved as compared to a single RJA, and was in the range of 0.95-0.99 in the center of the tank. The Taylor microscale Reynolds number was 334 and the region of homogeneity and isotropy was roughly $0.4 \times 0.4 \times 0.2$ m³.

In a comprehensive study, Pérez-Alvarado, et al. (2016) tested various driving algorithms for a single random jet array to characterize the statistics of the generated turbulence. A range of spatial configurations of the operating jets was considered. The statistics of the array's on/off time intervals were also varied to determine the best feasible homogeneous isotropic zero-mean turbulent flow in the ambient. As an inevitable limitation of the single RJAs, and due to the unidirectional forcing, nonzero skewness of the velocity fluctuation normal to the plane of the RJA was detected in all flows, and slightly super-Gaussian kurtoses of the velocity fluctuations were observed in all directions. The algorithms with set spatial configurations generated the most isotropic flows, however, their low turbulent kinetic energy and high mean flow velocities were not ideal. The algorithm referred to as RANDOM or "sunbathing algorithm", induced the closest approximation to zero-mean-flow homogeneous isotropic turbulence. The horizontal and vertical homogeneities of RMS velocities were reported as approximately ± 6 %, while, deviations from isotropy (w_{RMS}/u_{RMS}) fell in the range of 0.62 to 0.77. Mean flows were not observed to be greater than 7 % of the RMS velocities, while, the characteristic RMS velocity was reported as $Re_T = u_T$ $\ell/v = 2.360$.

2.4 Effect of background turbulence on turbulent flows

In most environmental and industrial turbulent flows, the existence of ambient disturbances dictates a higher complexity of the system. To investigate such systems, elaborate experimental facilities are required. In this section, the effects of a turbulent ambient on turbulent boundary layers, wakes, plumes and jets are discussed.

2.4.1 Boundary layers and wakes in external turbulent flows

The interaction between external disturbances and turbulent boundary layers and wakes have been investigated in a number of studies (Hancock and Bradshaw 1983, Thole and Bogard 1996, Sharp, et al. 2009, Amoura, et al. 2010). Hancock and Bradshaw (1989) employed smoke for flow visualizations within a boundary layer. The irregularity of the interface between the boundary layer and the external fluid stream was found to increase with free stream turbulence. Enhanced mixing was reported through the outer edge of the boundary layer, increasing with the intensity of the free-stream turbulence.

Thole and Bogard (1996) used an array of jets discharging perpendicular to the free-stream of a boundary layer and increased the external turbulence intensity to 10 to 20%. Although, the log-law sublayer still resisted disruption from all the imposed external intensities, the outer part of the boundary layer became much flatter due to the enhanced mixing. Analyzed energy spectra revealed a much greater mixing of the free stream into the boundary layer for the higher turbulence intensity cases.

Dasi, et al. (2007) quantified the concentration iso-surfaces of the concentration field of a high-Schmidt-number passive scalar (Rhodamine 6G, Sc=1250). An iso-kinetic source with an initial finite characteristic length scale discharging into the inertial layer of fully developed open channel flow turbulent boundary layer generated the turbulent field. A Reynolds number dependence was observed for the concentration threshold of the iso-surfaces at larger scales of the inertial—convective regime. Similar behavior for the injection length scale, and fractal geometry measurements were recorded. Moreover, it was concluded that the instantaneous scalar field showed the highest inhomogeneity for length scales close to the Kolmogorov scale.

An active grid was used by Sharp, et al. (2009) to identify the effects of free-stream turbulence on a boundary layer. The turbulence intensity of the free stream was varied between 0.25% to 10.5%.

The Reynolds number based on the momentum thickness of the boundary layer ranged between 550 to 3000, and the hot-wire anemometry technique was employed for the measurements. Compatible results with earlier statistics were obtained in terms of mean and variances of the longitudinal velocities. Analysis of the energy spectra and higher-order moments of the statistics revealed that higher mixing was attained by increasing the external turbulence intensities.

Mellado, et al. (2009) examined the passive scalar field of a temporally evolving shear layer by means of gradient trajectories. The scalar probability density function and the conditional scalar dissipation rate were analyzed in the presence of an external intermittency. The conditional dissipation rate showed a strong dependence with lateral position in addition to the conditioning value of the scalar. It was claimed that conditioning on the scalar had no influence on the fluctuation of the dissipation rate compared to unconditioned values. Flow partitioning was considered to measure the effect of external intermittency on flow parameters. Three zones including a turbulent zone, a turbulence interface and quasi-laminar diffusion layers were identified from the different types of gradient trajectories. For Reynolds numbers between 1500 and 3000 with a Schmidt number equal to 1, the turbulent interfaces were reported to make a major contribution to both statistics.

There are several experimental studies on the effects of external turbulence on wakes. Amoura, et al. (2010) related investigations of an array of pumps discharging into the top reservoir of a recirculating channel and generating the turbulent background which flowed downstream into a channel passing over a sphere place in the middle of the channel. The turbulence intensity of the free-stream varied between 15 to 26% of the mean flow. The centerline velocity defect decay was observed to vary as x⁻². The enhanced mixing induced by the external turbulence was demonstrated through the RMS profiles of the velocities. Shorter wake lengths and more damped vortex shedding were reported as the other effects of the ambient turbulence.

A theoretical analysis by Eames et al. (2011) provided a model describing the effect of external turbulence on a wake. The model was able to predict the behavior of wakes with Reynolds numbers of less than 1000, while, the turbulence induced by the wake itself was disregarded. Based on the approximations described, when the velocity defect becomes comparable to the RMS of the free-stream velocity, the velocity defect obeys an x⁻² decay rate, and the width of the wake grows linearly. The scaling of the velocity defect and wake width as well as their order of magnitude,

were defined by the model. However, poor agreement was found between the experimental records and the model's predictions.

2.4.2 Jets and plumes in a turbulent background

The external turbulence is either imposed by a turbulent cross, counter or coflowing stream, or by a turbulent ambient with zero mean flow. To date two principal hypotheses have been proposed for the effect of ambient turbulence on turbulent jets. The standard assumption supports the superposition of the dilution effects of the jet and that of the ambient turbulence, first proposed by Wright (1994) with the addition of a term to the classic entrainment function to account for the external turbulence, $E=2\pi\alpha bu_m$ (Morton, et al. 1956), where b and u_m represent the half-width of the velocity profile and jet's centerline mean velocity, respectively. However, Hunt (1994) suggested that in the case of great external turbulence, when the RMS velocity of the external turbulence is of the same order of the RMS of the jet velocity, the jet structure would be disrupted and this negative forcing would impose less entrainment. The external turbulence would be entrained and would not disrupt the jet structure provided the jet entrainment velocity is larger than the RMS velocity of the turbulent surrounding. This hypothesis indicates a possible reduction in entrainment unlike the standard assumption.

Wright (1994) analyzed the mixing of jets in a turbulent co-flow. By changing the bottom roughness of the channel, low levels of external turbulence could be generated. There was a linear relation between the dilution and the bottom roughness. Since this effect was observed even in the near field of the jet, the strength of the external turbulence in effecting the jet mixing was inferred.

Antoine, et al. (2001) performed simultaneous measurements of velocity and concentration using coupled 2D laser Doppler velocimetry and laser induced fluorescence. A turbulent jet (Re=10000) issuing into a low velocity co-flowing stream was fed with the fluorescent dye (Rhodamine B, Sc~3,000) to determine the flow characteristics. The self-similar region from x/d=70 to x/d=140 was explored to determine the moments involving correlations of velocity and concentration fields. The resulting mean and RMS profiles of velocities and concentration followed the accepted shapes, and the jet spreading rate reduction was found to be the main effect of the co-flow compared to the free jet case.

Gordon, Cater et al. (2004) used planar-laser-induced fluorescence measurements to investigate the mean concentration field in round zero-net-mass-flux jets in cross-flow (ZNMF-JICF). The jets were generated in a working fluid without net transfer of mass across the system boundary during one period of oscillation. In the range of examined Reynolds numbers of 600 to 23200 and velocity ratios of 3 to 30, the ensemble-averaged PLIF images distinguished two distinct flow regimes; single and multiple trajectory regions. While the multiple trajectory regime diffused deeply into the ambient cross-flow, the single trajectory demonstrated that the mixing of the bulk flow occurs outside the upstream boundary layer. Analyzing the diffusion of ZNMF-JICF revealed independency of the jet to cross-flow velocity ratio unlike JICF.

Gaskin, et al. (2004) were the first to support Hunt's prediction of a reduction in entrainment due to the existence of ambient turbulence. The effect of the ambient turbulence on plane jets in a shallow co-flow was studied. A plane jet discharged into a shallow flow, with a series of ridges at the bottom of the flume to generate the turbulent intensity of the co-flow. The Reynolds number of the jet was 1200 and the intensity of the external turbulence, u'/U_{∞} (where u' and U_{∞} were the RMS of the velocity fluctuations and the mean co-flow velocity, respectively) ranged from 5 to 15%. Hot-film anemometry and flow visualization with a passive scalar were used to obtain the velocity and concentration fields. It was observed that by increasing the external turbulence, the decay rate of the mean velocity was increased, while, the entrainment rate and dilution were decreased. Close to the jet exit, these effects were minimal. Further downstream, the jet structure was disrupted by the external turbulence, and the small-scale entrainment seemed to become dominant in comparison to the large-scale engulfment, which was known to be the dominant entrainment process in free jets.

Lavertu (2006), investigated differential scalar diffusion within turbulent jets. A single random jet array created nearly homogeneous, isotropic turbulent ambient with negligible mean flow. The jet axis and plane of the jet array were set parallel to ensure a constant external turbulence level along the jet axis (unlike that of Ching, et al. 1995 and Guo, et al. 1999, where the turbulent intensity increased by downstream distances). The jet Reynolds number ranged from 900 to 10600 and the RMS of the velocity fluctuations of the external turbulence was roughly 1.5 cm/s. It was reported that the differential diffusion in the turbulent jet was increased with higher ambient turbulence, attributed to the increase in entrainment due to the surrounding turbulence.

Shan and Dimotakis (2006) studied the concentration fields in liquid-phase strong transverse jets over the Reynolds number range of 1000 to 20 000, using the laser-induced-fluorescence technique. The velocity ratio between the jet and the freestream was 10. The turbulent mixing in the far field ($^{x}/_{D} = 50$) of the transverse jet was reported to be Reynolds number dependent, as were the scalar field PDF evolutions. Comparison between the transverse jets and the jets discharging into the quiescent reservoirs implied more efficient mixing of the entrained fluid in the presence of the external forcing. A well-mixed plateau separated by sharp cliffs were observed in the jet's scalar field. Moreover, the scalar field was found to be anisotropic. This anisotropy was related to the vortex-induced large-scale strain field of the transverse jet. It was concluded that the large and small scales of high-Schmidt-number turbulent mixing flows could be correlated, with a probable result on the universality of small scales of the scalar field for Reynolds numbers beyond 200 000.

Xia and Lam (2009) performed combined velocity and concentration measurements of submerged round jets into a quiescent ambient and within a coflow. Laser Doppler anemometry along with the laser-induced fluorescence techniques were employed for the measurements at $^{\chi}/_{D} = 40$ for the Reynolds numbers of 1000 to 5000. While, the coflow-to-jet velocity ratios of 0 to 0.43 were implemented. The jet centerline velocity and concentration were reported to decrease with axial streamwise distances in the zone of established flow. While, a linear increase with downstream distance was reported regarding the jet width. The presence of a strong coflow was shown to augment the turbulence properties of the jet. The length of the zone of flow establishment was found to increase as the flow approached the laminar case, with a shorter zone of flow establishment length for the concentration than for velocity by one to two jet exit diameters.

Or, et al. (2011) considered the change of velocity and concentration fields in the near field of a round jet in stagnant ambient and in a moving environment of a co-flow, counter-flow and cross-flow situation. The effect of the moving ambient on the flow establishment and potential core length was discussed by means of velocity and concentration measurements using PIV-LIF. The decay constants for the jet centerline velocity and concentration were compared to the $1/\chi$ profile in the quiescent ambient. While the presence of a co-flow tended to enhance the decay constant, however, the counter-flow decreased the constant as did the cross-flow. In terms of the virtual origin, it was reported that any form of moving environment slightly reduced the physical length

of the potential core. Correspondingly, the intermittency function was proposed for analyzing the concentration fluctuations in the potential core. Finally, an estimate of the potential core length of a jet in moving environment was deduced from the mean intermittency function.

The effect of ambient turbulence on turbulent jet properties were investigated by Khorsandi (2011) and Khorsandi, et al. (2013). Using the same apparatus as the work of Lavertu (2006), two different turbulent intensities were studied and velocity measurements were conducted at different downstream positions. The jet Reynolds numbers were 5,300, 5,800 and 10,600, and the turbulent kinetic energy of the background were $\frac{1}{2}\langle u_i u_i \rangle = 4.44$ and 9.33 m²/s². Acoustic Doppler velocimetry (ADV) and flying hot-film anemometry were employed for velocity measurements. The decay rate of the mean velocity, and half-widths of the velocity were observed to increase in the presence of the ambient turbulence. Moreover, the decreased mass flow rate was reported to imply lower entrainment rates, which confirmed the prediction of Hunt (1994) and experimental results of Gaskin, et al. (2004).

Torres, et al. (2012) investigated the perturbation of the mean scalar concentration field of jets discharging into a uniform counter-flow. The PLIF technique was used to obtain the centerline decay and radial spreading of the mean concentration field. Experiments were conducted for two different jet diameters, and jet to counter-flow velocity ratios varied between 4 to 19. It was found that the jet growth rate in the radial direction fell into two regions; i.e. regions characterized by a linear growth and a power law, respectively. Empirical expressions were proposed to predict the concentration decay in the established flow region in both the axial and radial directions of jets in counter-flow.

Gampert, et al. (2013) conducted experimental research for detailed investigation of conditional statistics of passive scalar field and its instantaneous dissipation rate in the presence of external disturbances. A round turbulent jet of propane discharged into coflowing carbon dioxide, and the high-frequency planar Rayleigh scattering method facilitated the acquisition of a highly resolved three-dimensional field of mass fraction including the Taylor's microscales. The Reynolds number varied from 3000 to 8600. Agreements were reported in terms of joint probability density of the scalar difference, the length of dissipation elements, and the normalized marginal probability density functions as compared to the DNS results of Wang and Peters (2006) and Wang and Peters

(2008). It was mentioned that the viscous forces and dissipation played a significant role in the inertial-range statistics, and probably, for the higher-order statistics as well, evident from the much weaker signatures of the internal intermittency in dissipation-dominated flow regions.

Thong, et al. (2015) investigated the mixing control in turbulent jets to optimize a practical combustion. The capability of a confined cross-flow for dilution mixing was investigated along with detailed assessment of turbulent mixing capabilities of the jet in a combined cross-flow. The studied flow was a primary water jet, which was modified with smaller jets located upstream of the nozzle exit. The joint PIV-PLIF techniques were employed to characterize the flow structures. Various primary flows were examined to find the influence of cross-flow velocity on the induced scalar mixing within the nozzle. Based on the velocity ratios, which caused the three distinct flow modes of streaming flow mode, impinging flow mode, and backflow flow mode, different flow structures were detected in the flow. Furthermore, Thong, et al. (2017) observed that the side injection of cross-flow highly influenced the near-field region of the flow and had minor effects further downstream. With increasing the jet to cross-flow momentum ratio, velocity decay rates and turbulence intensity within the jet core were reported to increase in the near-field of the jet.

Ryan, et al. (2017) examined the turbulent mixing and scalar transport in an inclined, skewed jet through a crossflow using magnetic resonance imaging (MRI) measurement technique in addition to the Large Eddy Simulation (LES) numerical approach. Three-dimensional mean velocity and mean concentration fields were obtained for a 30° skewed jet subjected to the crossflow. Existence of a single dominant vortex induced spanwise asymmetries to the velocity and concentration profiles, which resulted in increased and highly anisotropic mixing throughout the jet in compare to the stagnant surrounding.

Near-field interactions between an inclined jet with a crossflow over a flat plate was investigated by Wen, et al. (2018). A 30° inclined round water pipe was discharged through the streamwise direction of the crossflow. Time-resolved particle image velocimetry (TR-PIV) and LIF techniques were used to measure the flow structures. Four different jet-to-cross-flow velocity ratios, 0.25, 0.5, 0.75, and 1.0, were examined to compare the flow patterns in the near-field. Subsequently, significant interaction decreases in jet—cross flow was reported in the inclined configuration, especially, through the lower velocity ratios. Moreover, considerable flow instabilities at the nozzle exit were interpreted as a robust interaction between the emerging jet and the crossflow.

2.5 Planar Laser induced fluorescence (PLIF)

The Planar Laser Induced Fluorescence (PLIF) measurement technique is a preferred flow measurement system, which is used to obtain a series of instantaneous two-dimensional images of the flow's scalar field. The PLIF measurement technique is a non-intrusive, and high-resolution measurement technique which also allows for visualization of the turbulent flow. In comparison to other similar techniques, such as conductometric, thermal, and color change techniques, PLIF has the advantage of detecting micro, meso and macro turbulent mixing scales. Computational Fluid Dynamics (CFD) approaches are unable to predict the turbulent flows transient phase precisely, even though, could perform acceptable simulations of the established turbulent flows. (Gorgeon et al.,1993, Wilkes et al.,2005, and Hu et al.,2010).

Crucial to the development of these technique have been the progress of laser sources and sensors. CW lasers were used to excite fluorescent dyes strain in the 70s. Frequency-doubled CW laser sources found to be more functional in the 80s and 2-D imaging via array detectors was possible (PLIF). Through the late 90s, infrared excitation approaches (IR-PLIF) were suggested. High pressure and high-speed imaging PLIF were reported to be feasible through the mid-2000s. Laser light is not the only energy source for fluorescence excitation, but it does enable high-performance fluorescence mechanisms due to the laser's high spectral irradiance and focus-ability. Fluorescence occurs when light energy excites a molecule causing an electron to briefly increase its energy state, which then emits light, at a longer wavelength, as it falls back to a lower energy state. The PLIF measurement technique used the fluoresce of a dye which at lower concentrations is proportional to the light it emits. (Shan et al., 2004, Crimaldi 2008; Vanderweel and Tavoularis, 2014, Donges and Noll 2015, Hanson et al., 2016).

Guilbault (1990) proposed the relation between the fluorescence light intensity and corresponding concentration of the fluorescent substance as follows.

$$F = \phi I_o (1 - e^{\varepsilon bc}) \tag{2.5}$$

Where ϕ defines the quantum efficiency, I_o expresses the incident radiant power, ε is the molar absorptivity, b defines as the path length of the cell and c represents the molar concentration. Therefore, the basic fluorescence intensity-concentration relation reveals that some major elements other than the concentration would affect the fluorescent intensity. The Mclaren expression of the

basic equation states that for $\varepsilon bc < 0.05$ or in other words, for a highly diluted dye solution, the basic equation would be reduced to the following form.

$$F = k\phi I_o \varepsilon bc \tag{3.4}$$

Through the LIF procedure, passive scalars can be measured within a region illuminated by a laser source. This region can be a point, along the laser line, a two-dimensional plane (PLIF), or a volume. A plane can be formed using cylindrical lenses or by scanning a laser beam into a laser sheet (when averaged over time). Laser beam scanning devices could be categorized as deflection and refraction scanners. While, deflection scanners are subcategorized as oscillating and rotating mirrors (Deusch and Dracos 2001, Larsen and Crimaldi 2006, Cho et al. 2014).

In a general sense, several phenomena such as attenuation, photobleaching, thermal blooming, and photomultiplier tube drift threaten the accuracy of LIF measurements. In cases where the laser beam crosses a mass of dyed fluid before attaining the measurement section, attenuation occurs attributable to energy absorption by the fluorescent dye throughout the laser beam trajectory, resulting in a non-linear relationship between the concentration and the fluorescence intensity within the measurement section. When the laser radiation heats up the dyed fluid it leads to the thermal blooming phenomenon. Furthermore, the reduction of fluorescence intensity of the dye is caused by a steady irradiation causing photobleaching. (Smith, 1977, Koochesfahani, 1984, Wang and Fiedler, 2000, Lavertu, 2006, Crimaldi, 2008, Chorvatova, et al. 2018).

The signal-to-noise ratios (SNR) in addition to spatial resolution are crucial factors determining the LIF measurement accuracy. In this regard, various approaches have been examined and proposed. Studies have considered the effect of alterations in the laser illumination uniformity, , have evaluated the impacts of insufficient spatial resolution, have investigated digital approaches to collect signals from the LIF technique using CCD cameras, , have examined probable errors due to variations in laser sheet thicknesses, laser output power and dye concentration (Koochesfahani and Dimotakis, 1985, Ferrier, et al 1993, Guillart, et al. 1998, Wang and Fiedler 2000, Vanderwel and Tavoularis 2014).

Chapter 3: Experimental methods

3.1 Experimental facility

The experiments were conducted in the Environmental Hydraulics laboratory situated in the Department of Civil Engineering and Applied Mechanics of McGill University. They were performed in an open glass tank with dimensions of 1.5m by 2.4m by 0.9m, as shown in Figure 3.1. The side walls of the tank were made of single panes of 1.905 cm thick tempered glass while, the bottom was made of two superimposed 1.905 cm thick tempered glass panes for a cumulative thickness of 3.81 cm, to reduce the deflection due to the weight of the water. A steel frame supported the panes of glass. The experimental apparatus was situated in a darkroom (completely painted in black, to minimize any peripheral light reflections during the experiments.



Figure 3.1 Glass tank structure.

3.2 Background conditions

As the aim of this study was to explore and evaluate the effects of background turbulence on the scalar field of a turbulent jet, the observations of the turbulent jets in the presence of turbulent ambient were compared to the observations of the jet issuing into a quiescent background. For the case of the experiments performed in the quiescent background, the tank was gradually filled with filtered water. Subsequent to filling, the tank was left to settle (usually more than 3 hrs) to allow

dissolved oxygen to come out of solution, to allow circulation in the tank due to filling to decay and for the water to reach a state of thermal equilibrium with the ambient temperature.

A random jet array (RJA) system was used to generate an approximately homogeneous, isotropic, zero-mean turbulent flow in the section of the glass tank in which the experiments were performed. The jet array was designed based on that of Variano and Cowen (2008) but constructed on a larger scale. The RJA has 10 columns of 6 bilge pumps (Rule 25D, 500 GPH) attached to a vertical sheet (0.9m by 1.5m) of high-density polyethylene, as shown in Figure 3.2.

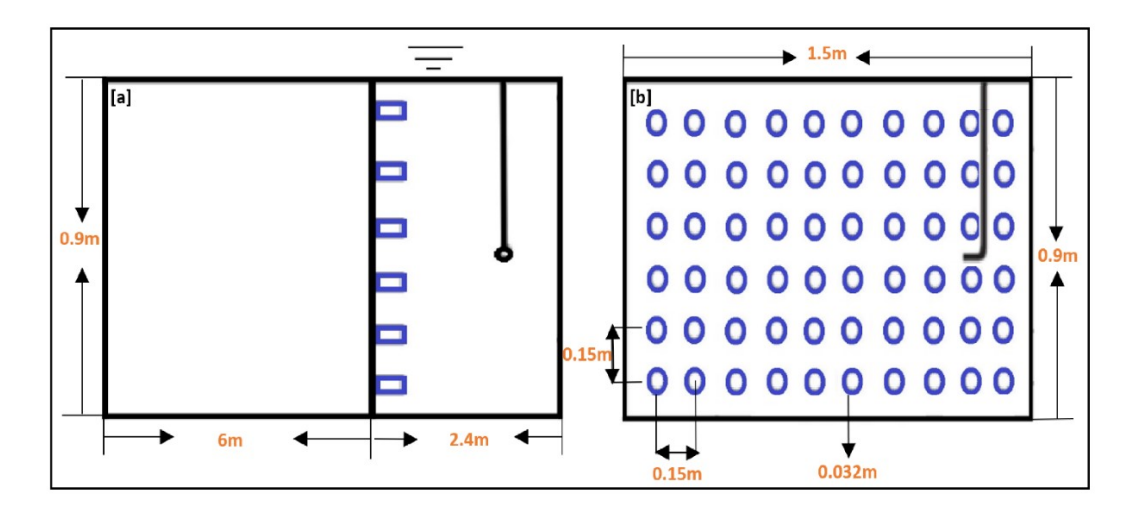


Figure 3.2 Dimensions of the RJA, glass tank, and the jet setup. a) side view. b) front view.

Polyvinyl chloride (PVC) elbow joints (Spears 1407-010) were fastened to the outlet of the pumps and precisely leveled to straighten the flow in a direction perpendicular to the plane of the RJA. Additionally, a 15cm PVC extension of 3.18cm diameter, as well as a male adapter (Spears 436-132) were coupled to the bilge pumps to expand the diameter of the outlets and straighten the flow (Figure 3.3).

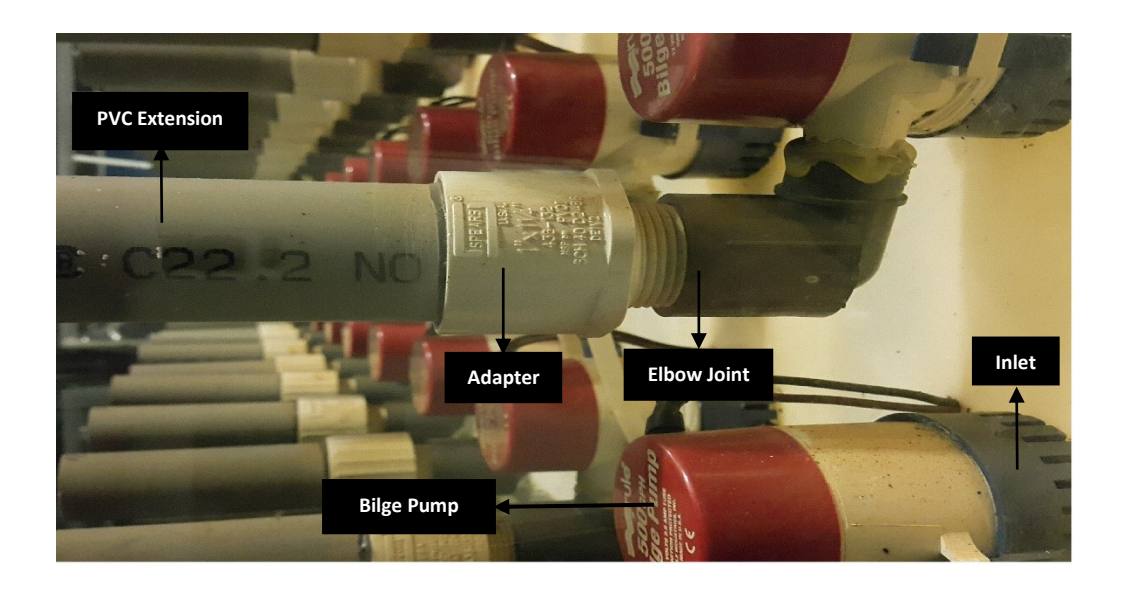


Figure 3.3 Random jet array bilge pumps and their components.

The RJA mechanism was designed such that the net mass flow rate within the control volume remains zero. This was achieved as the bilge pumps draw in the surrounding water at their base, and immediately expel the water into the same ambient through the attached PVC extensions 24cm away from the polyethylene plane to which the base was attached. Preserving a zero net mass flow rate inside the control volume permits the zero mean flow to be maintained. Identical horizontal and vertical center-to-center distances of the jets (15 cm) as well as the symmetric boundary condition with the tank walls and sides and the free surface helps to reduce secondary flows (Figure 3.4) as found for oscillating grid turbulence (Fernando and De Silva 1993).

The required power for RJA system's pumps was provided by means of a power supply (Model SPSA2012200). This supplied a constant 12V output with variable current, which depended on the demand of the pumps. The power supply's maximum output power was 120A. Therefore, the maximum instantaneous power demand could never exceed the power supply's output power as each pump's electricity consumption was less than 2A. The wires connecting the power supply to the pumps were taped up and sealed to prevent any formation of small circuits within the water inside the glass tank. Cable connections were used a sealed crimp and solder butt splice connector (NSPA Multilink ML5-16). These were covered with numerous coatings of liquid electrical tape, an adhesive-lined supple polyolefin heat shrinks tubing and again finally further layers of liquid electrical tape to establish the optimal insulation against the moisture and water.



Figure 3.4 Front view of random jet array and jet in the glass tank.

A custom algorithm was scripted in LabVIEW software to control the RJA and adjust its performance. The algorithm allowed the pumps to switch on and off independently. The jets produced by the pumps merged at a distance downstream of the RJA plane generating a turbulent zone that decayed in the normal direction to the plane of the jet array. A number of RJA control algorithms have been investigated (Perez-Alvarado et al., 2016) to determine which generated the closest estimation to a homogeneous isotropic zero-mean flow background turbulence.

The ideal algorithm would generate turbulence with the lowest mean flow, maximum degree of isotropy, and the highest RMS velocity. The turbulence characteristics for each algorithm tested were observed and compared to determine the best algorithm.

The best performing algorithm was that called RANDOM, which used the came driving algorithm concept as that of Variano and Cowan (2008). RANDOM was used for the experiments in this study. In the algorithm, each pump was independently and randomly was switched on and off. The on and off intervals were selected from a normal distribution with adjustable mean (μ) and standard deviation (σ). The optimal values were μ_{on} and σ_{on} of 12s and 4s and μ_{of} and σ_{of} of 108s and 36s respectively, which maintained 10% of the pumps functioning on average at any time.

3.3 Turbulent jet apparatus

The turbulent jet flow discharged horizontally into the tank with its outlet level and directed in a plane parallel to the RJA plane. The jet apparatus included a supply reservoir, a pump, a constant head reservoir, a solenoid valve, a three-dimensional traversing mechanism and some other jet components (Figure 3.5 and photo in Figure 3.4). The hydraulic setup of the jet was designed to maintain a constant flow rate and allowed for a range of jet Reynolds number.

A constant flow to the jet was assured by a constant head reservoir fed from a supply reservoir. The supply reservoir was an approximately 35-liter glass carboy located beside the tank on the floor used for mixing the dye and the water prior to each experiment. It was also the overflow repository for the constant head reservoir, a 12-liter spherical glass carboy located at an elevation of 4 m above the floor. The dyed water was pumped toward the constant head reservoir by means of a $\frac{1}{3}$ hp pump and conveyed via 1.27cm diameter plastic tubing. A ball valve was placed near the pump's outlet to control the flow rate toward the constant head reservoir. The constant head reservoir was a 12-liter spherical glass carboy located about 1.9m above the top of the glass tank to supply a uniform and steady gravitational flow toward the jet. The level in the constant head reservoir was maintained with an overflow that returned to the supply reservoir. This setup is shown in Figure 3.5.

The flow to the jet was supplied from the base of the constant head reservoir with a 1.9 cm diameter plastic tubing. A ball valve controlled the flow rate, which was measured using a flow meter (Omega FL50002A), with an accuracy of maximum 5%. A solenoid valve, whose controller was located near the supply reservoir, allowed the set flow rate to be turned on and off remotely at the start and end of the experiments. A range of jet Reynolds numbers were possible. The Reynolds numbers for this study were 10600 and 5800 requiring flow rates of $4.26 \frac{L}{min}$ and $2.33 \frac{L}{min}$ respectively.

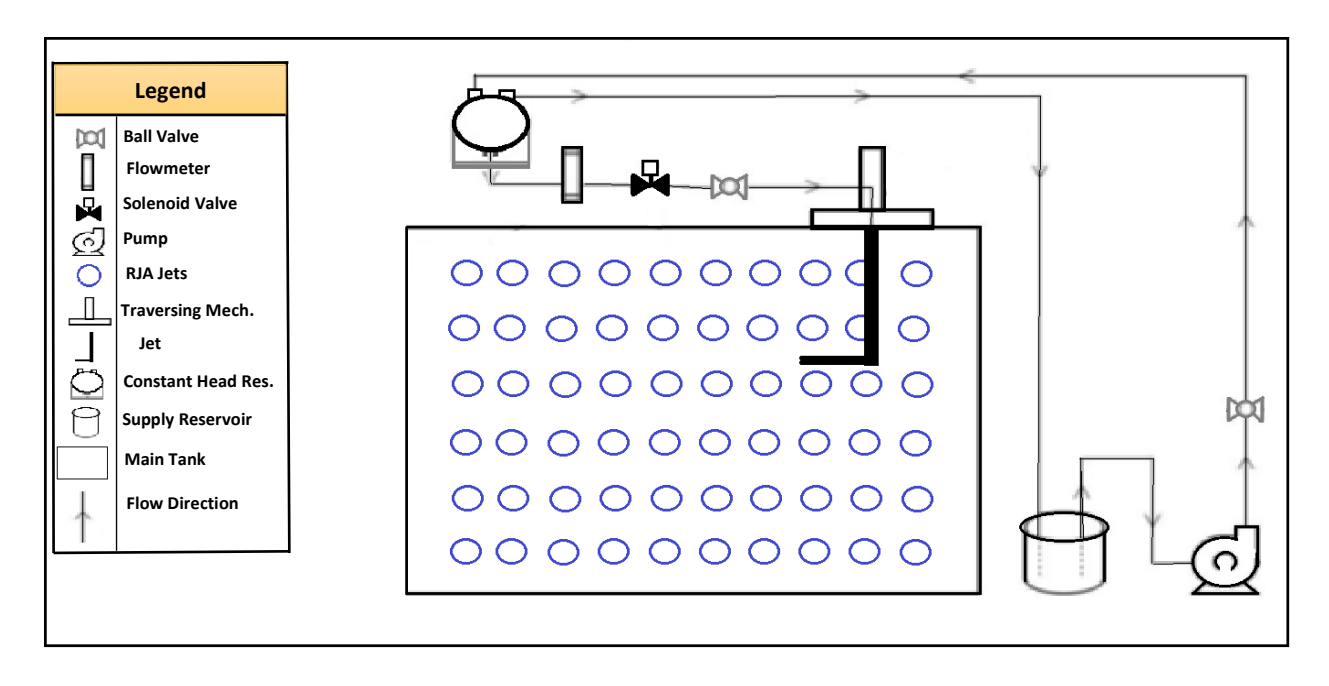


Figure 3.5 Constant head supply of dyed water to the jet (not to scale).

The jet was made of a section of copper pipe with an 8 mm inner diameter that extended vertically a distance of 50 cm followed by a 90° bend that extended 48 cm allowing the jet to release horizontally in a plane parallel to the RJA (x-direction). The 48 cm length of pipe beyond the 90° bend ensured the flow was fully develop at the jet exit. Prior to the experiments, the jet was leveled precisely in both the vertical and horizontal axes to ensure the accuracy of the data (e.g. radial profiles) as shown in Figure 3.6. As the turbulence created by the RJA decayed in the normal direction to its plane, the jet was placed horizontally in a plane parallel to the RJA so that a constant level of background turbulence occurred along the jet's axis. For these experiments the jet was situated 110cm from the tips of the RJA PVC extensions where the previous studies using this setup (Khorsandi et al., 2013, Perez-Alvarado et al., 2016) indicated that the turbulence generated by the RJA was nearly homogeneous and isotropic with zero-mean flow.

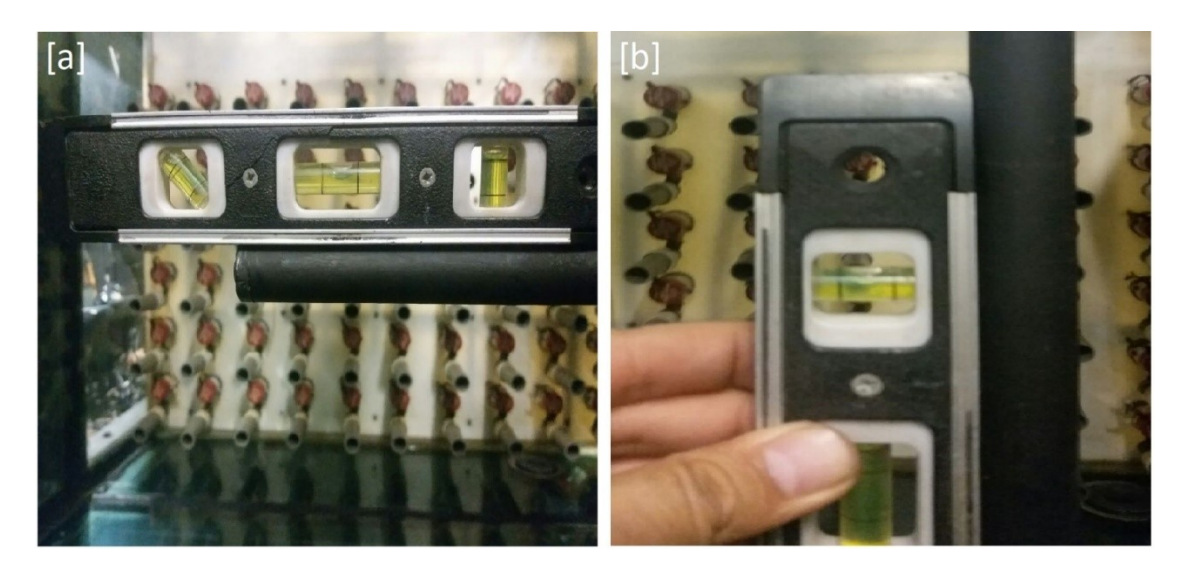


Figure 3.6 [a] horizontally and [b] vertically leveled jet and its distance from the RJA plane.

A Velmex traversing mechanism (Figure 3.7) was used to allow the jet to translate precisely within the three-dimensional volume of the glass tank. The traversing mechanism was made of a system of three BiSlide assemblies that each encompasses a basis, a carriage, and a motor-driven lead screw. A limit switcher was placed at the base of each assemblage to prevent collisions between the jet and the tank walls or the carriage and the end plates. The motors were controlled with a stepper motor controller (Velmex VXM-2) and a LabVIEW program was used to translate the jet in the three-dimensions by means of the traversing mechanism.

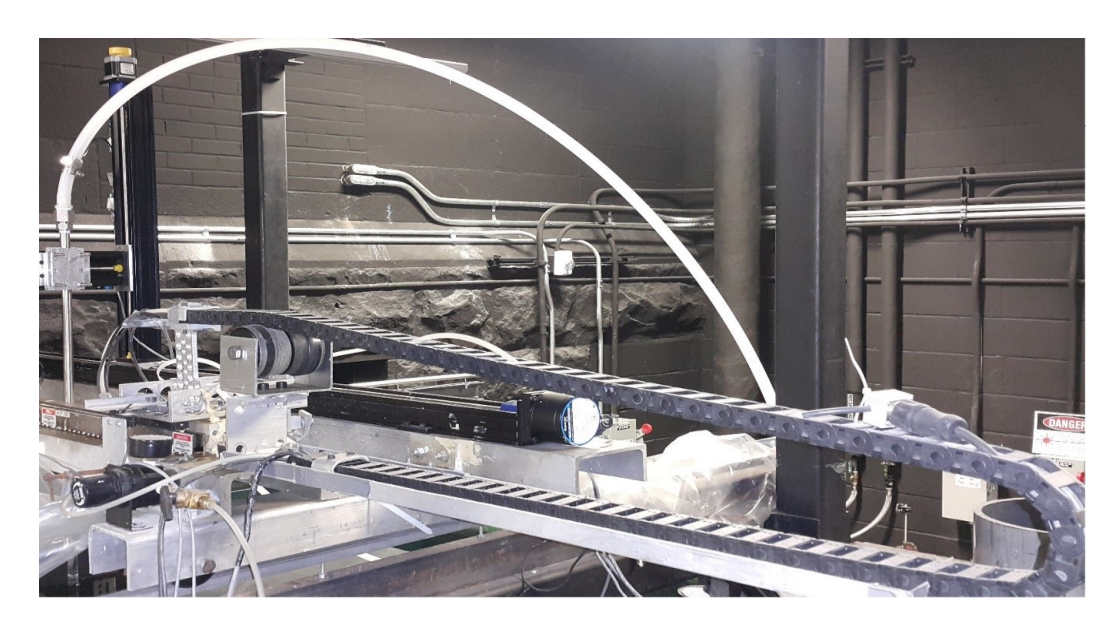


Figure 3.7 Traversing mechanism setup and its components

The range of movement of the traversing mechanism was 130 cm, 24 cm and 55 cm in the x, y and z directions respectively with a resolution of 0.05mm. Note that the x-direction is aligned along the jet axis, y is normal to the plane of the RJA and z is in the vertical direction. The traversing mechanism was mounted on a C-shaped channel, that allowed motion in the x-direction. This channel could be displaced in the y-direction along the top of the tank by means of wheels running along guide rails (Figure 3.7). This allowed for approximate placement manually followed by precise adjustment using the traversing mechanism.

3.4 Planar Laser induced fluorescence (PLIF) apparatus

Planar Laser Induced Fluorescence (PLIF) was performed both for flow visualization technique and for quantifying scalar concentrations in the jet. In this technique a fluorescent dye within the flow is excited by a laser sheet, which results in the dye fluorescing at an intensity that is proportional to its concentration. Images recording the light intensity can then be converted into concentrations. Concentrations were acquired within the radial cross-sections of the turbulent jets emitted into both quiescent and turbulent backgrounds. The LIF apparatus includes the laser sheet generating system (laser beam generator device, laser beam conveying mirrors and a laser scanning device) and the signal collecting system (camera, intensifier, lens, filter).

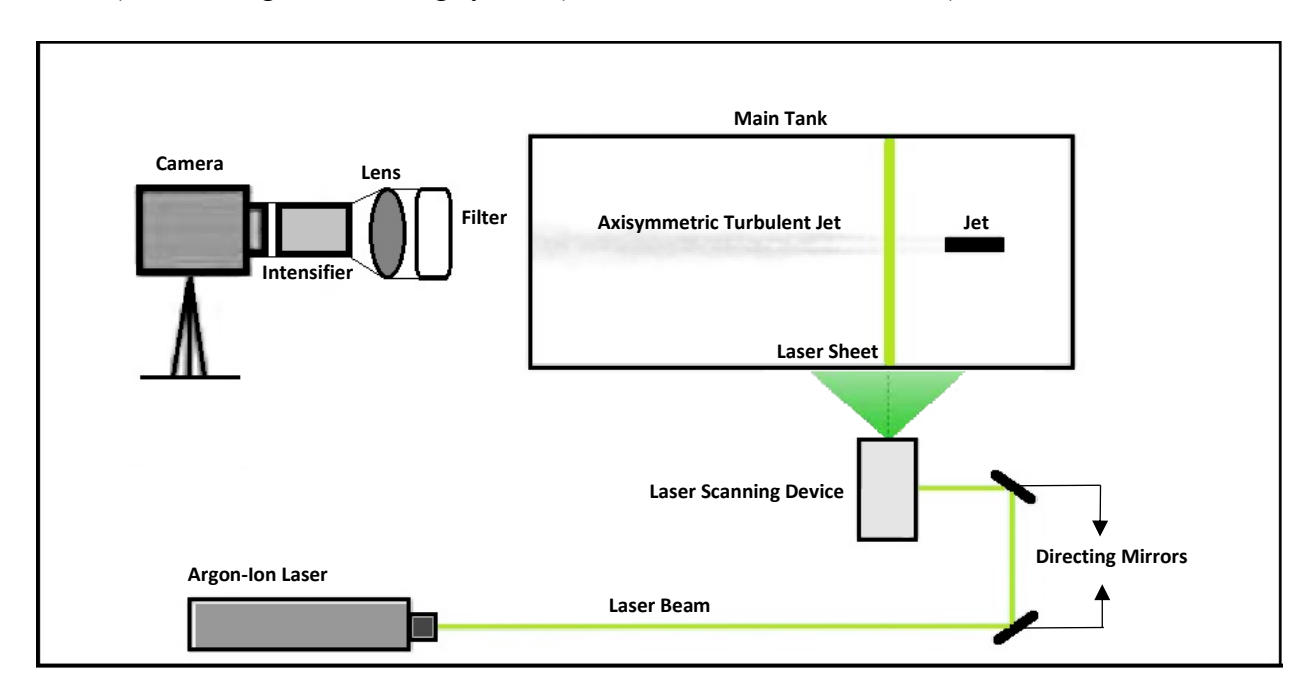


Figure 3.8 Schematic of the planar LIF system, top-view (not to scale).

The laser light excites the fluorescent dye (disodium fluorescent) thereby making it fluoresce in the plane of the intended measurement positions. The laser sheet generation system, an argon-ion laser (Coherent Innova 90) was employed to generate the laser beam. The operation mode of the laser was adjusted to the light-regulated mode due to the consistency (\pm 0.5%) of its output power in comparison to the other modes. A constant and known output power was required for minimizing the error in the concentration measurements. This was achieved by warming the laser up, that is it was operated for about an hour at the intended output power before each experiment to reduce any potential oscillation and non-uniformity in its output power. A power meter (Coherent Lasermate) with a precision of \pm 5% was employed to measure the power of the generated laser beam at the point of emission (from the laser). The laser power was monitored throughout the warm-up period and immediately after each experiment to assess the uniformity and consistency of the laser output power during each experiment. Differences greater than 2% between the initial and the final output power were considered unacceptable.

For the experiments, the aperture of the laser was adjusted to 3.97 mm and the output power of the laser was regulated to 1 W. The laser was operated in single line mode at a wavelength of 514.5nm (green). Based on the manufacturer's information, the laser beam has a Gaussian cross-section. Two mirrors (Melles 1÷Griot 02MLQ003/009), installed on magnetic optical holders with adjustment screws, were used to direct the laser beam from the laser to the laser scanning system (Figure 3.9).

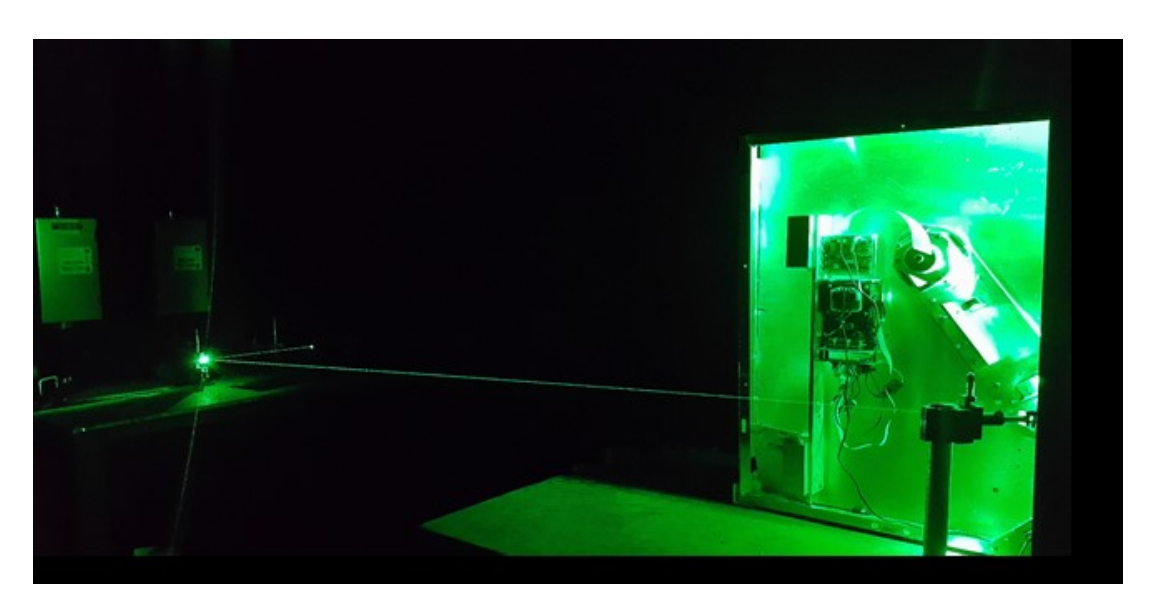


Figure 3.9 Operation of the directing mirrors and the laser scanning device

The laser beam was expanded to a planar area of measurement to obtain cross-sections of the jet for the experiments. A laser scanning device expanded the laser beam to a laser sheet at the required measurement section. The laser scanning device consisted of a focusing lens, a circular dielectric mirror, a rotating mirror, and an electrical controller circuit, which was programmed to rotate the mirror with a certain angular velocity (Figure 3.10). This mechanism was mounted inside an aluminum case that could be leveled and screwed tightly to a metallic table to reduce peripheral vibrations and consequently any slight displacements.

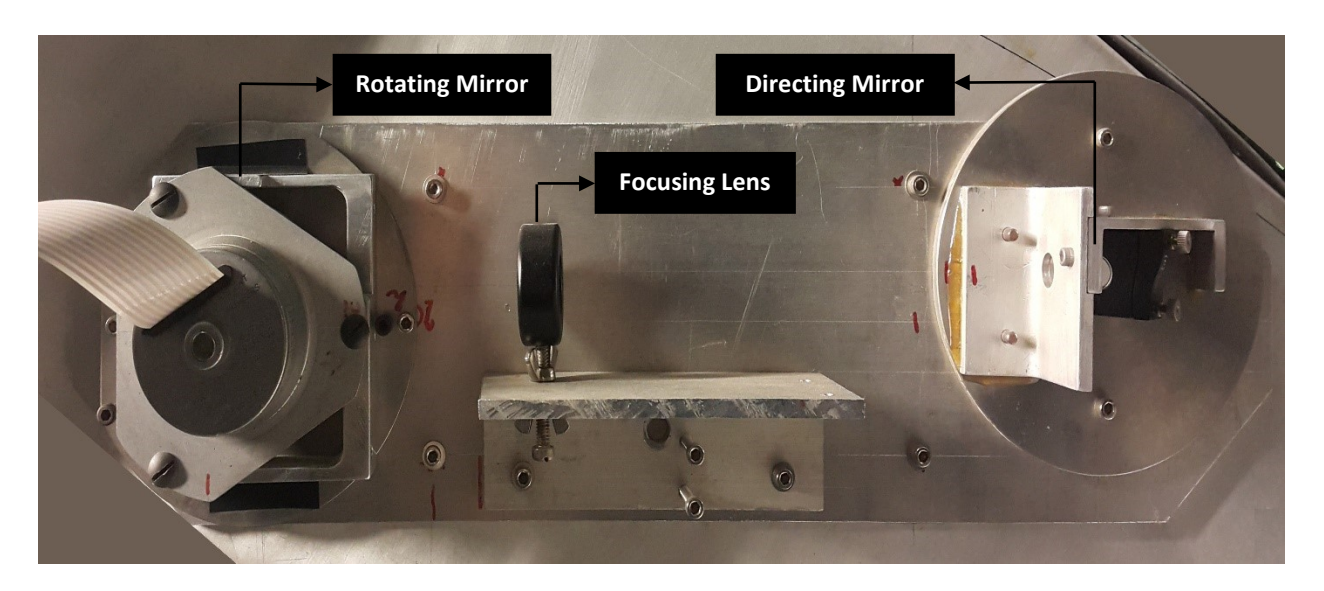


Figure 3.10 Components of the laser beam scanning device.

As the laser beam entered the scanning device, a 12.7mm circular dielectric mirror (Newport 5151) directed it to the focusing lens (1.5m focal length plano-convex lens PLCX-25.4-772.6- C), which focused the beam to a waist diameter of 470µm at the focal point. The waist diameter is calculated as (Ready 1978):

$$d_0 = \frac{2.44f_1\lambda_1}{D_b} \tag{3.1}$$

where d_0 is the focused diameter, f_1 is the lens focal length, λ_1 is the wavelength of the laser beam and D_b is the diameter of the laser beam. Another important parameter was the distance at which the focused beam grows to $\sqrt{2}$ times of the waist diameter, the Rayleigh range, which is calculated as (Ready 1978):

$$Z_R = \frac{\pi f_1^2 \lambda_1}{D_h}$$
 (3.2)

where Z_R is the Rayleigh range. As shown in Figure 3.10, the lens was fixed on a holder fixed inside the aluminum frame of the laser scanning device. After passing through the focusing lens, the laser beam reached an 8-sided polygonal mirror (Lincoln Laser Company DT-08-236-019). An electric motor rotated the polygonal mirror at an angular velocity of 12000rpm, scanning the laser beam to produce a laser sheet when integrated over a given time interval. The 12000 rpm of the octagonal mirror, results in Therefore, the rotation of the octagon produces nearly $1600 \frac{scans}{second}$ of the laser beam over the intended measurement plane. The intensity of the laser sheet decreases approximately by 44% from the near laser corner to the far laser corner of the measurement plane, due to the scan sweeping out a section/segment of a circle. This difference in intensity is accounted for in the calibration procedure described below. The amount of thermal blooming and photobleaching is minimized due to the short period that any parcel of fluid is irradiated.

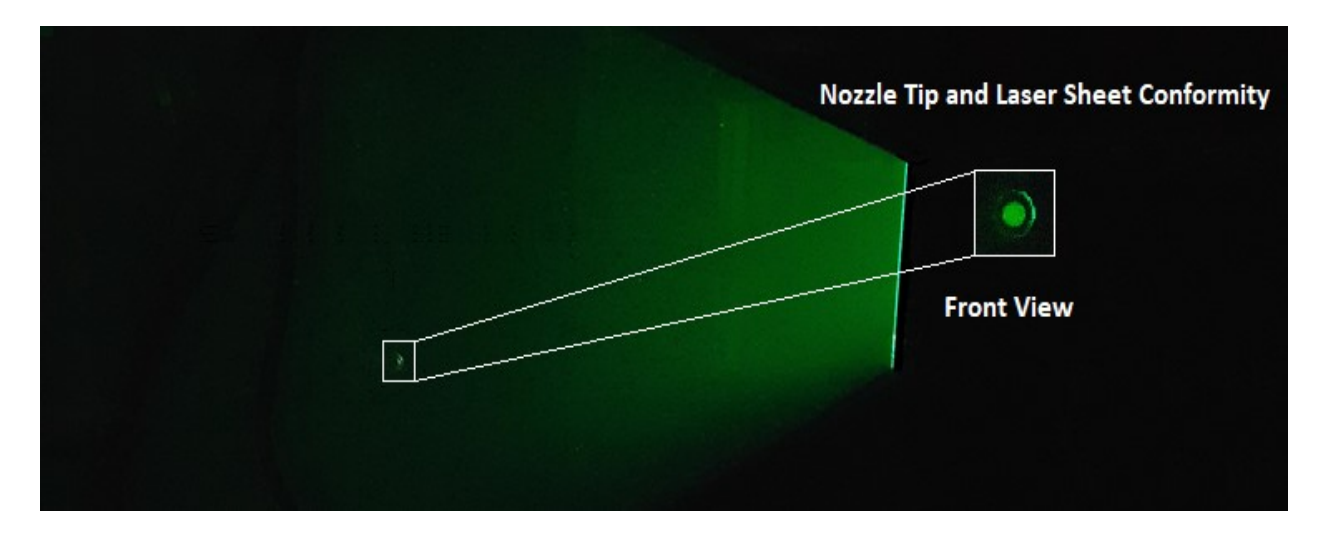


Figure 3.11 Coincidence of the jet tip with the generated laser sheet.

Another option to generate a laser sheet from a laser beam would be to use corresponding cylindrical lenses. However, these cylindrical lenses do not produce a uniform intensity laser sheet due to a Gaussian distribution of light intensity over the measurement area. There is also an increased risk of photobleaching and thermal blooming as the fluid is continually irradiated by the laser sheet, which would need to be minimized by using a pulsed laser.

The laser scanning device an all its elements are aligned to forma laser sheet perpendicular to the streamwise axis of the turbulent jet. For this purpose, a plumb bob, a level, and the traversing mechanism were employed to maintain a vertical and a fine horizontal alignment along the jet axis using the traversing mechanism. The laser scanning device and, thus also, the laser sheet were leveled and oriented perpendicular to the glass pane of the tank and thus also the jet axis. The plumb bob was used to ensure its vertical alignment. The set up was then tested with the minimum output power of the laser (for safety) and the final position was assured by fixing the position of the adjustment screws.

The final check of the alignment of the laser sheet perpendicular to the jet axis was achieved by traversing the jet in the horizontal and vertical directions and assuring that the tip of the jet remained just touching the laser sheet. Note that the laser has a shutter at its outlet, so that it can be blocked when not in use. This is required for the safety of the operator.

The light intensity emitted by a given dye concentration was measured with a signal collecting system that also needed to be aligned perpendicular to the laser sheet. This system was a camera coupled with an image intensifier and an optical filter, that was fixed and secured along an optical rail of 69cm length held and supported via two tripods. The tripods (QuickSet 5-95534-9 and 5-95534-9A) allowed the system to be adjusted vertically (Figure 3.12). The signal emittedby the dye excited by the laser sheet initially passed through an optical filter to ensure the blocking of any scattered laser radiation to the lens. Therefore, a 25mm diameter 550nm long pass color filter (ThorLabs FGL550) was attached to the camera lens (F-Micro-Nikkor 55mm f/2.8).

According to the manufacturer's specifications, the optical filter reduces transmission of wavelengths of 525nm to lower than 0.0004%. As the wavelength of the emitted light from disodium fluorescent ranges from 480 to 650nm, a small portion of the fluorescence signal and other disruptive scattered laser radiations are blocked at the optical filter and only the fluorescence radiations above 525nm reached the lens.

The measurement section was captured using a lens with a focal length of 1.5m and angle of view of 43°. The lens's aperture was adjusted to the maximum possible to admit the greatest amount of light to the camera sensors in order to have the highest sensitivity to the emitted fluorescence signals.

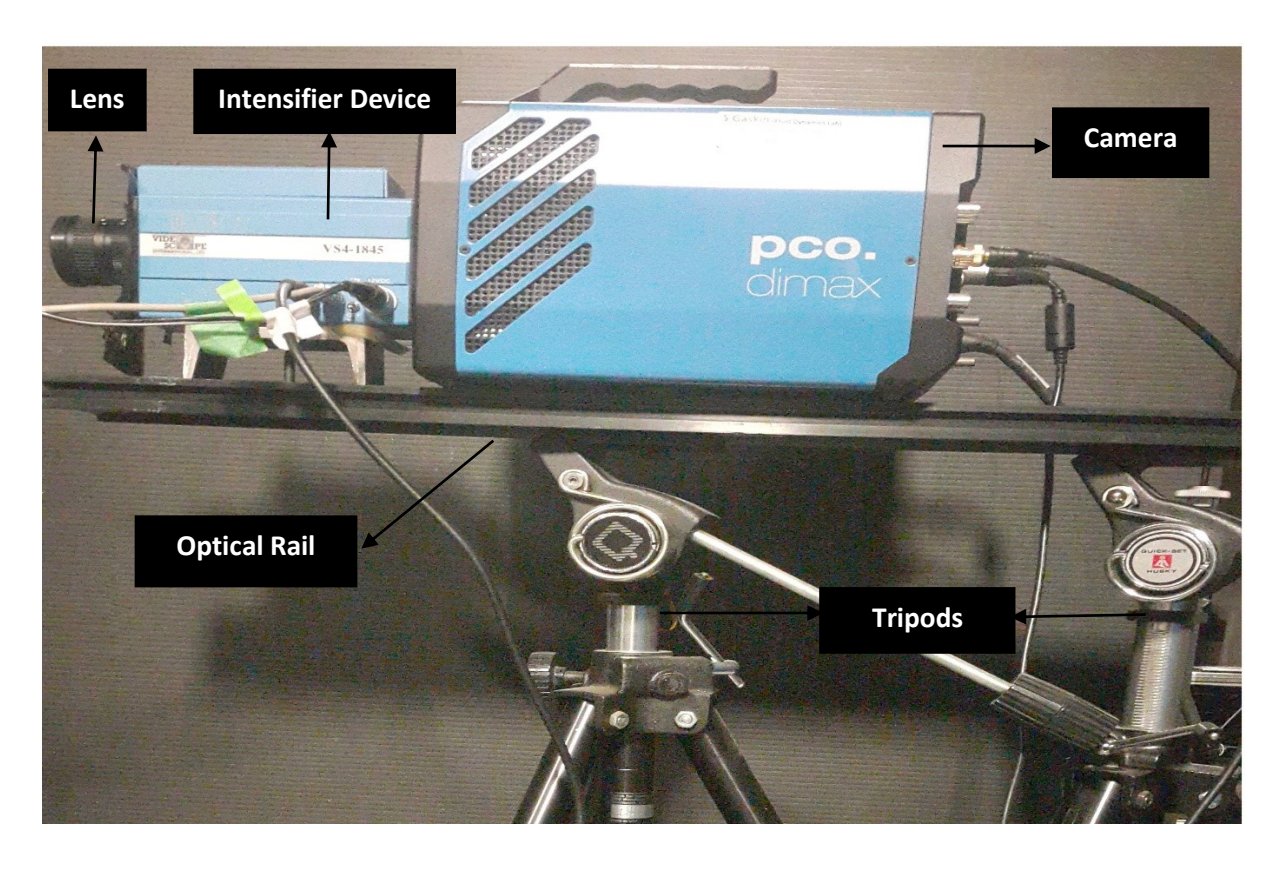


Figure 3.12 Signal collecting system components.

An image intensifier (Video Scope VS4-1845) was coupled to the camera to allow the system to have a higher sensitivity to the lower intensity signals. The selected dye concentration for the experiments led to low fluorescence levels emitted (with a linear relationship between light intensity and camera greyscale). The wavelength range of the intensifier of 450-900 nm was appropriate for the filtered signal range (525-650nm).

The image intensifier functions by inducing two subsequent emissions of electrons (by the incident low-level light) between plates with a high DC voltage difference (similarly to an electrons cascade on a phosphor screen) thereby strengthening the light signal. This procedure uses three plates (a photocathode, a micro-channel plate and a phosphor screen) spanning a high DC voltage difference to speed up the electron flow (Figure 3.13).

The light reaching the intensifier first hits a Gallium Arsenide (GaAs) photocathode, which conveys the electrons towards the micro-channel plate. This results in a secondary cascade of electrons towards the phosphor screen. The increased number of electrons hitting the phosphor

screen results in the emission of photons, at a rate that has been amplified compared to the initial signal. The photocathode of the image intensifier is vulnerable to normal or intense light (e.g. ambient room lighting) so all lights were switched off prior to and during the operation of the camera.

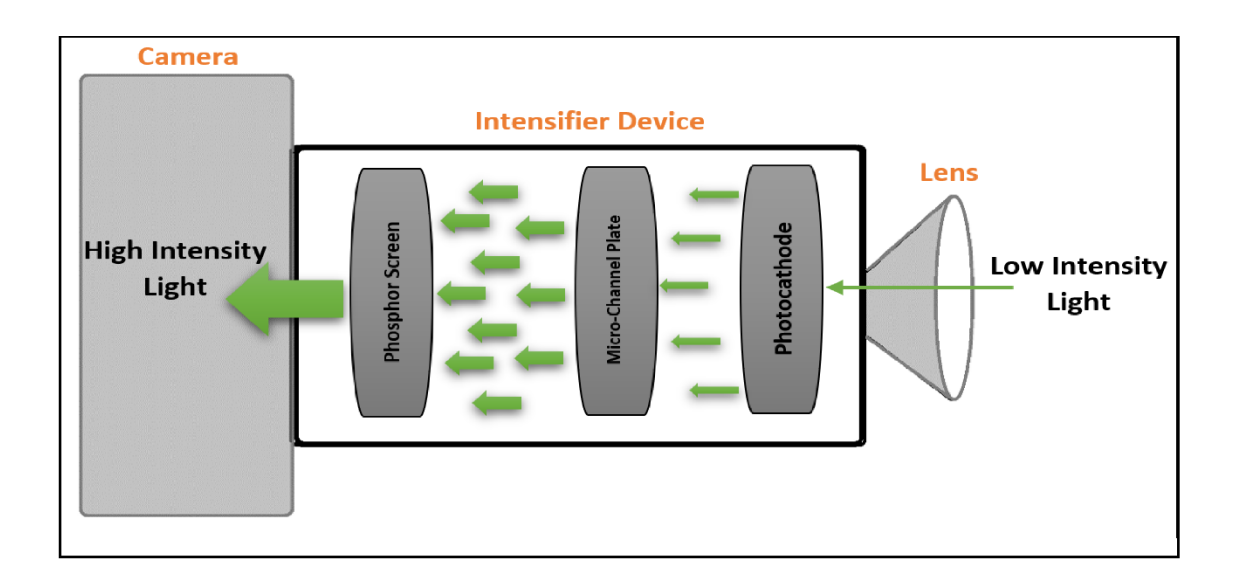


Figure 3.13 Schematic of the signal intensification procedure.

The intensifier gate, gain, and gate delay were set using the its controller software (VSI image intensifier controller software). The gate mode was set to the continuous mode during the experiments, which maintains a continuous flow of electrons from the photocathode toward the Micro-channel plate as well as an continuous intensification of the signal during the signal collecting procedure. The intensifier gain was set to 75000 for all of the experiments, while gate delay was set to zero to results at all measurement locations that could be compared.

A C-mount adapter coupled the image intensifier device to the camera (12-bit monochrome pco.dimax). This camera, which has a 2016×2016-pixel resolution, captured instantaneous cross-sections of dyed turbulent jets flow A controller software (Camware) allowed for the adjustment of recording characteristics. However, the image intensifier reduced the image capture area to a circulation section with a radius of 800 pixels. In addition, coupling the camera and intensifier results in the central area of the image being more sensitive and reaching saturation at lower light intensity levels.

As shown in Figure 3.14, the coupled optical filter, image intensifier, and the camera was fixed on an optical rail mounted on two tripods. The signal collection system was aligned perpendicular to the jet using the adjustable tripods (in darkness except for feeble illumination of the tank). Subsequently, the jet tip was aligned with the centre of the measurement plane, as indicated by a red cross in the Camware software (Figure 3.14) and the alignment was checked by translating the jet along its axis (680 mm) with the traversing mechanism. Any adjustments required were made with the tripods to adjust the camera height. This procedure was repeated until the alignment was optimized so that the camera image plane was parallel to the laser sheet.

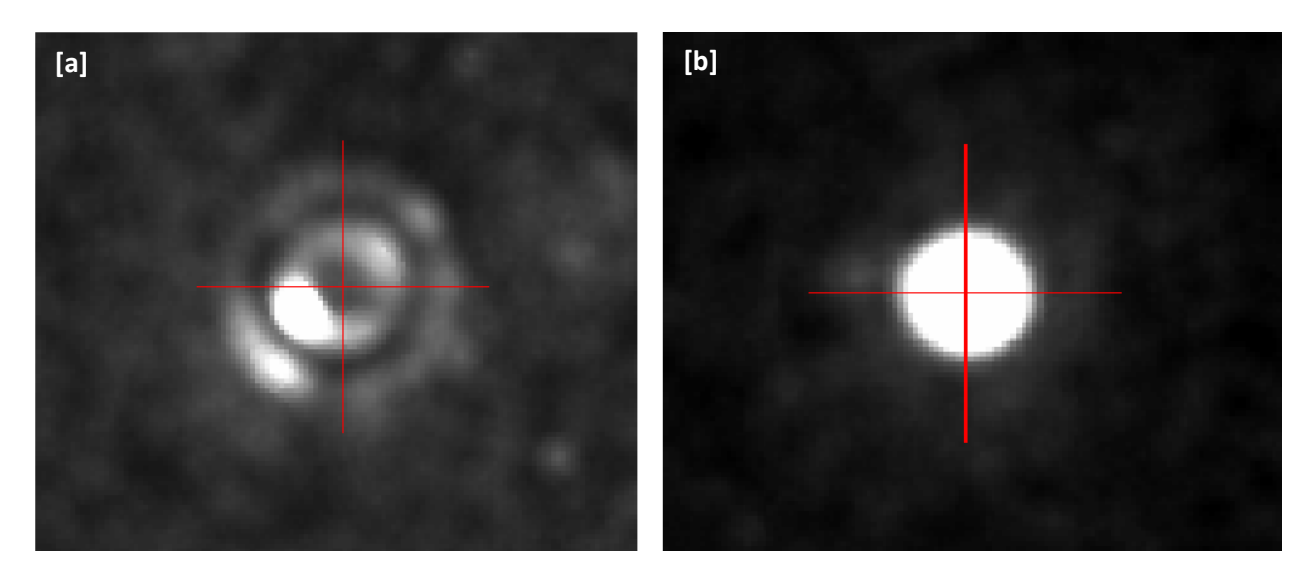


Figure 3.14 Coincidence of the centers of the jet and image. a) Without jet. b) With jet.

Once the camera system was aligned, the camera was focussed on the tip of the jet when it coincided with the laser sheet. The focus in the field of view was checked by translating the jet and viewing the tip in the laser sheet and a final check was made of the laser sheet alignment.

The laser, the laser sheet generation system, and the signal collection system were fixed to rigid tables and to reduce vibrations to a minimum their legs were placed on vibration dampers made of 25.4mm thick sheets of Sorbothane.

The fluorescent dye used in the laser induced fluorescence (LIF) experiments to determine scalar concentrations was disodium fluorescein having a Schmidt number of 2000. As the disodium fluorescein decays rapidly with exposure to light it stored in a light proof container. In addition,

all sources of light were turned off both during preparations for the experiments and during the experiments.

The concentration of disodium fluorescein used for the experiments was in the order of 10^{-7} mol/L as this resulted in a linear relationship between concentration and light intensity when excited by the laser light. Note that the relationship is not linear at higher concentrations. This low concentration also ensured the density of the solution was the same as the ambient, which prevents inertial effects. In addition, attenuation and trapping of the emitted light is minimized at low concentrations. Therefore, sources of error in the LIF experiments are minimized through the use of low concentrations of fluorescent dye.

3.5 Data acquisition and post-processing

The concentrations of a passive scalar in the turbulent jet were observed using planar laser induced fluorescence (LIF) and acquired as a series of instantaneous images of the cross-sections of the jet flow captured by a 12-bit camera (PCO.dimax). The camera was controlled with a software package (Camware). This enabled the adjustment of the signal acquisition rate, delay time, and the exposure time. A standard signal acquisition rate of 30 frames per second, as well as an exposure time of 30ms, was selected, while the exposure delay time was set to zero. As each laser beam scan duration was 625µs, an exposure of 30ms integrated 48 beam scans per image.

The data was acquired as a series of images of 2016×2016 pixels in which each pixel contains a light intensity value. The images were first saved on the internal memory of the camera, then, transferred to the hard disk of the computer via a Link cable and finally stored on an external hard drive. Each experiment's duration was set to the optimum interval of 170 seconds due to the following restrictions: firstly, re-entrainment of dyed jet fluid, which would lead to an overestimation of the measured concentrations, and secondly, the size of the internal camera memory limited the number of images to 5000.

Convergence of the mean and RMS concentration data of the turbulent jet released into a quiescent ambient occurred after 170 s or 5000 images (Perez-Alvarado, 2016). Therefore, one experiment was sufficient. However, 5 to 7 series of full-length experiments at each axial distance were required for convergence of the data of the jets that emitted into the turbulent background. Jet cross-sections were measured at axial distances of x/d = 0, 10, 20, 30, 40, 50, 60 and 70.

Each full-length experiment resulted in 44 GB of data which was stored on an external hard drive. Post-processing of the data was dividing the data into blocks for each computer, which then used parallel computing to reduce processing time. The post-processing procedure was performed using several custom MATLAB codes. First, a calibration was made to determine the relationship between light intensity to concentration. This was then used to convert the images to concentration, which allow for the calculations of mean concentrations (centreline, radial profiles), RMS concentrations, radial profile half widths and radius of gyration.

3.6 Calibration procedure

Calibration was required to convert the light intensity of the images obtain from the LIF experiments into concentrations of the passive scalar (disodium fluorescein) for each pixel in the image. Guilbault (1973) proposed the following relationship between light intensity and concentration as:

$$F = \phi I_o (1 - e^{\varepsilon bc}) \tag{3.3}$$

Where ϕ defines the quantum efficiency, I_o expresses the incident radiant power, ε is the molar absorptivity, b defines as the path length of the cell and c represents the molar concentration. Mclaren expression of the basic equation states that for $\varepsilon bc < 0.05$ or in other words, for a highly diluted dye solution, the basic equation would be reduced to the following form:

$$F = k\phi I_o \varepsilon b c \tag{3.4}$$

Consequently, it can be concluded that the fluorescence intensity is a linear function of concentration for highly diluted concentrations. In the captured images, there is a spatial variation of laser sheet intensity in the measurement plane, of intensification by the intensifier, due to the curvature of the lens and due to the pixel by pixel variation in the camera. This required a pixel by pixel calibration of the images. A calibration procedure was therefore carried out and applied to the full image.

The calibration was carried out using a rectangular calibration box 75cm by 43cm by 31cm (Figure 3.15). The open top calibration box sides were made of 0.63cm thick panes of tempered glass while a 2.54cm thick sheet of plexiglass was used for the bottom. A relatively thin tempered glass was used for the sides to maintain the maximum peripheral transparency while a thicker plexiglass pane was used for strength. Use of the calibration box allowed for minimizing dye consumption.

For the calibration procedure, the calibration box was placed inside the main tank, while both were empty, and two cylindrical PVC supports raised it to be coincident with the camera view (Figure 3.15). Once the box was in place both the tank and the calibration box were filled to the same level.

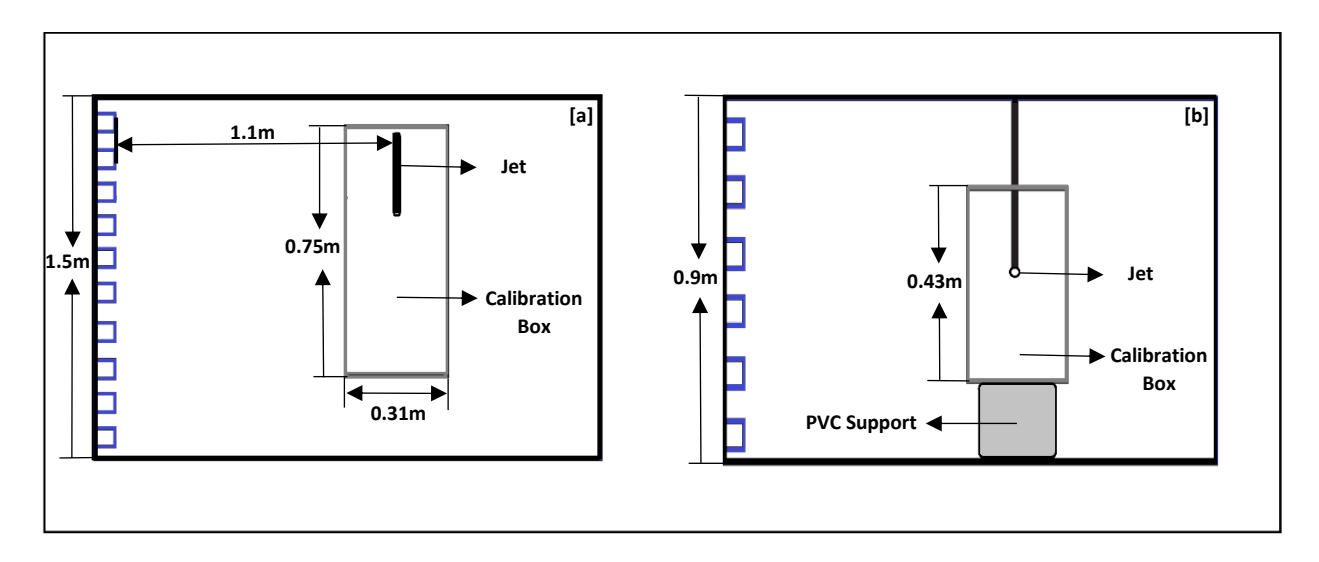


Figure 3.15 Location of the calibration box in the tank. a) Top view. b) Front view.

Thereafter, the dyed water, which was mixed inside the supply reservoir in advance, was circulated between the supply reservoir and the calibration box by means of a coupled $\frac{1}{3}$ HP pump, several two-way hoses, regulation valves, and the jet, which was situated within the calibration box inside the main tank. A hose was linked to the outlet of the pump to convey the dyed water to the constant head reservoir, which feeds the jet. While, the constant head's overflow hose was attached to the calibration box to conserve the closed cycle of flow throughout the jet, supply reservoir, and the calibration box.

The calibration procedure was used to develop a relationship between the light intensity of the images and the concentration within the jet. The first image taken was of the calibration box while it was filled with pure water, which was considered as the uncontaminated background. Thereafter, images were obtained as the concentration of the sodium fluorescein was increased at fixed increments of concentration. Each image recorded light intensity data in a circular measurement field of approximately 40cm in radius (due to the field of view restrictions from the intensifier). A linear association between the concentrations and the intensity counts was developed on a pixel by pixel basis. The individual calibration curves accounted for the different excitation intensities across the field of view as well as for the range of response from individual pixels. This is shown

in Figure 3.16 for a pixel in the centre of the image and one at the margins of the image (central and marginal points).

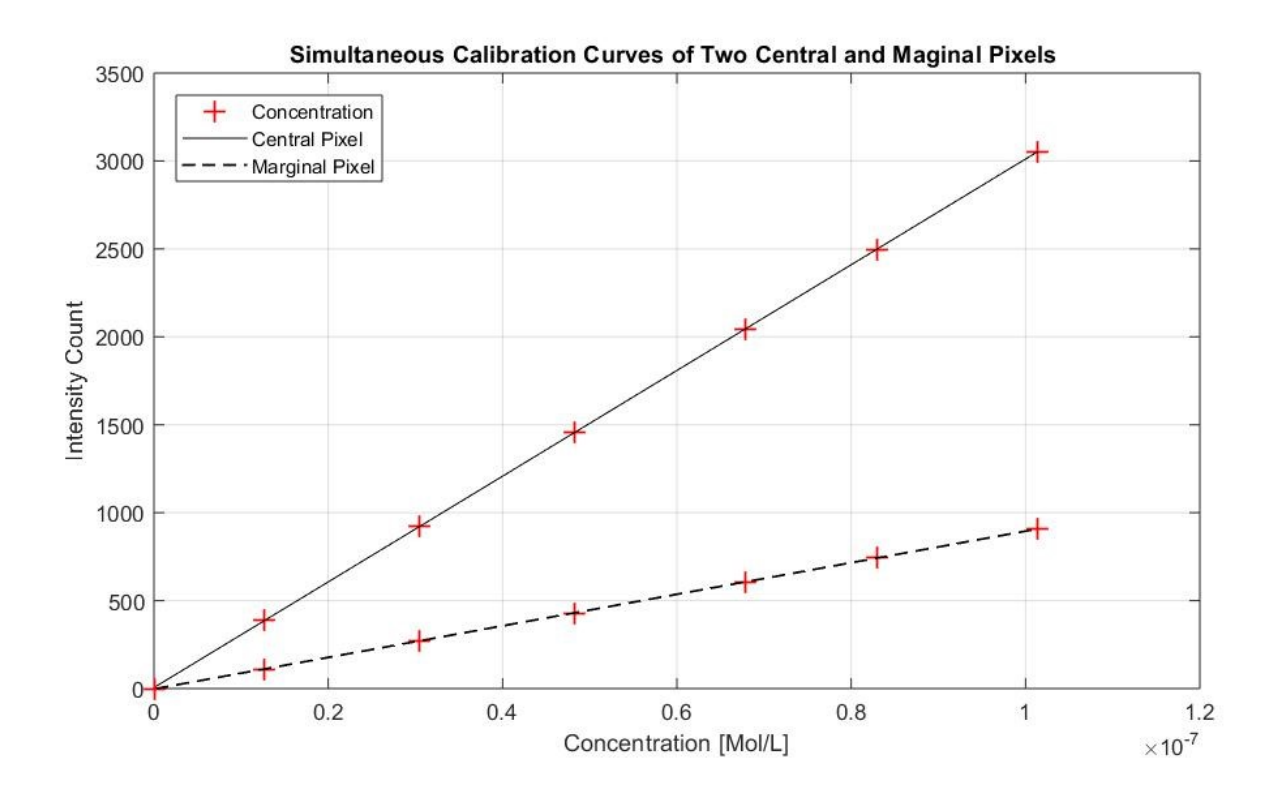


Figure 3.16Central and marginal calibration curves.

A custom MATLAB script was programmed and used to read the data of each pixel and fit a linear curve in the following form;

$$C_{df} = AI + B (3.5)$$

Where C_{df} indicates the of disodium fluorescein's concentration, I denotes the intensity of the corresponding pixel, and A and B are constants of the linear fitted curve. These constants were calculated, saved, and used to convert recorded light intensity to concentrations.

3.7 Reduction of potential sources of error

Any sources of light or reflections of the laser sheet can contribute to error in the images, both in areas recording the background flow and in the jet flow, and hence overestimations of concentrations. To minimize these sources of error, all sources of light as well as potential reflectors were turned off, covered, or painted black inside the lab (including walls, ceiling, tank

structure etc.). The experimental volume in the tank was also covered with black cardboard except for a small slit for the laser sheet and the field of view for the camera. The main sources of error in the LIF technique are thermal blooming, photobleaching, attenuation, trapping, and inertial effects. If the laser radiation heats up the dyed fluid it can lead to the thermal blooming phenomenon, i.e. fluorescence due to heat instead of light excitation. Photobleaching or reduction in the fluorescence intensity of the dye is caused by steady irradiation. These two phenomena were controlled and avoided throughout the calibration procedure and the experiments by creating the laser sheet by scanning the laser beam, thus reducing the time of irradiation of the fluid

Lavertu (2006) conducted a test in which the dyed fluid was continuously irradiated to observe the degradation of the fluorescence signal with time for the joint effects of photobleaching and thermal blooming. Based on his results, the fluorescence signal degraded by 2%, in comparison to its peak value, in 200µs. In the current study, the laser beam irradiates a parcel of fluid for 2µs and hence it was concluded that thermal blooming and photobleaching impacts could be assumed to be insignificant. Attenuation is attributable to energy absorption by the fluorescent dye along the laser beam trajectory, which results in a non-linear relationship between the concentration and the fluorescence intensity within the measurement section. Accordingly, by adopting a highly diluted concentration of dye, attenuation is minimized. Trapping occurs when the fluorescence signal within the measurement section is absorbed by dye located between the measurement section and the signal collection system.

Another potential source of error in the LIF experiments arises from the temperature difference between the dyed jet fluid and the ambient fluid resulting in inertial effects. To reduce this error, during the experiments the reservoir for the jet fluid was filled from the main tank prior to each experiment. Additionally, the thermal effect of the laser beam on the jet flow was negligible due to the very short fraction of time that the fluid was irradiated by the laser (due to scanning the laser beam). The density difference due to the 1 mg/L concentration of disodium fluorescein used was calculated to be $7 \times 10^{-5}\%$, which is negligible.

Chapter 4: Validation of concentration measurements

Data on the passive scalar field of the turbulent jets are compared to previous studies to validate the measurement technique. For this purpose, the mean centreline concentration decay with axial distance and the self similarity of a radial profile of turbulent momentum jets issued into the quiescent ambient of the present study were empared to the same results of Dahm and Dimotakis (1990), Law and Wang (2000), Webster et al. (2001), Fukushima et al. (2002), Lavertu (2006), and Perez-Alvardo (2016). All of the studies noted, as well as the present study, were conducted using the LIF technique for the concentration measurements of the neutrally-buoyant liquid-phase (water) turbulent jets that issued into the identical liquid-phase stagnant surroundings.

Dahm and Dimotakis (1990) conducted concentration measurements of a Re = 5000 turbulent water jet that emitted into a stagnant water ambient by means of the LIF technique. The centerline concentrations were measured within the range of 0 < x/D < 350 in addition to the jet radial profiles. Law and Wang (2000) reported the synchronous velocity and concentration measurements of an Re = 12700 turbulent jet. They conducted the experiments using Digital Particle Image Velocimetry (DPIV) and LIF concurrently to obtain the centerline concentrations and the radial concentration profiles of the jet in the range of $40 \le x/D \le 70$.

Webster et al. (2001) accomplished the simultaneous measurements of the passive scalar and the velocity field of a turbulent water jet that maintained a Reynolds number of 3000 via coupling the PIV/LIF measurement techniques. Meanwhile, Fukushima et al. (2002) utilized the same coupled measurement techniques as Webster et al. to observe the coincident vector and scalar field behaviours of a turbulent jet with a Reynolds number of 2000. Finally, Lavertu (2006) observed the radial concentration profiles of a Re = 10600 turbulent jet at a constant longitudinal axial distance of x/D = 50.

For the validation, two commonly measured parameters of the neutrally buoyant turbulent jets were considered as the comparison criteria to ensure the current measurement technique's meticulousness and compare its accuracy to that of the other results. The measured parameters were normalized for comparison, with the axial and radial distances normalized by the jet diameter and the concentrations normalized by the maximum centreline concentration.

The indices compared are as the streamwise gradient of the mean centerline concentrations normalized by the concentrations right at the jet exit $\binom{C_{cl}}{C_0}$ vs. $\binom{x}{D}$ and the radial profiles of mean concentrations normalized by the centerline concentrations $\binom{C_r}{C_{cl}}$ vs. $\binom{x}{D}$. Although all radial profiles andthe streamwise concentration decay gradients of the jets issued into a quiescent background were verified and validated, only the radial concentration profiles at two axial distances each at a different Reynolds number are plotted.

In Figures 4.1, the streamwise gradient of the normalized mean centerline concentrations of the higher Reynolds number jet (Re. of 10600) is compared to studies in the literature. There is a good comparison with the results of Dahm and Dimotakis (1990) and those of Law and Wang (2000) with comparable Reynolds numbers of 5000 and 10600 respectively. Note that Law and Wang conducted their experiments only within the χ /D range of 40 to 80.

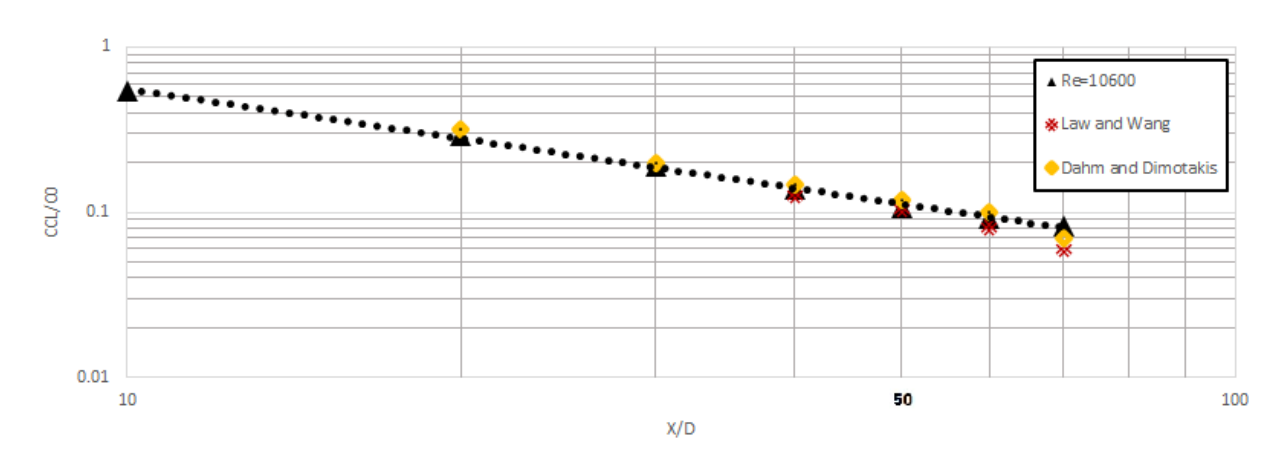


Figure 4.1 Validation of normalised mean centreline concentration with axial distance for a turbulent jet of Re=10600 of the present study with data from Law and Wang (2000) and Dahm and Dimotakis (1990)

A seen in figure 4.1, The normalized streamwise concentrations of the present study and those of previous studies follow a x^{-1} decay rate with axial distance. Therefore, it is interpreted that the logarithmic decay rate of the streamwise concentration is independent of Reynolds number of the jet, as reported in the literature.

Theoretically, the normalized mean radial concentration profiles within the self-similar zone of a turbulent flow should collapse onto a Gaussian profile. The present study considerss the self-similar region of turbulent jets.

The radial profile of the jet with the lower Reynolds number (Re = 5800) at $^{x}/_{D}$ = 70 is plotted with the $^{x}/_{D}$ = 30 of the jet with the higher Reynolds number (Re = 10600) in Figure 4.2 and compared to the corresponding radial profiles of Law and Wang (2000), Webster et al. (2001), Fukushima et al. (2002), and Lavertu (2006).

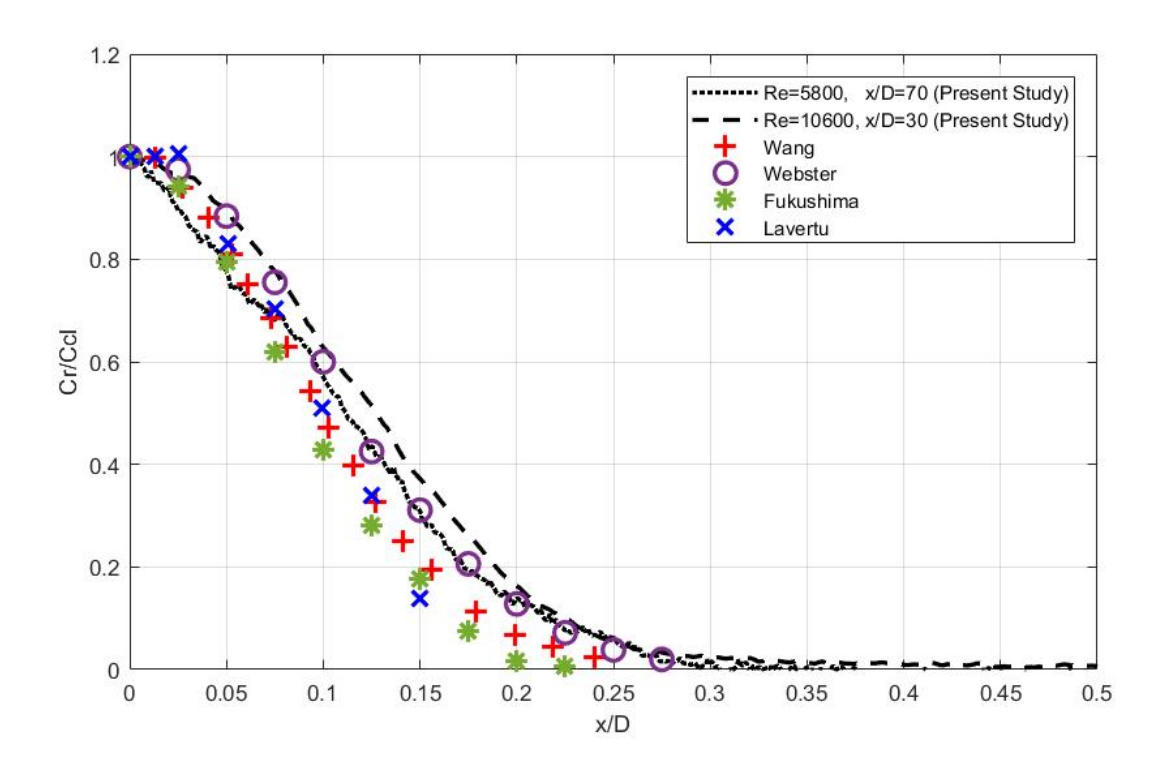


Figure 4.2 Validation of the radial profiles of the mean concentrations of a turbulent jet from the present study (Re=10600 at x/D = 30 and Re=5800 at x/D = 70) with data from Law and Wang (2000), Webster et al. (2001), Fukushima et al. (2002), and Lavertu (2006).

The comparison indicates a good fit with the previous studies, with the best fit occurring for the profiles at similar Reynolds number. That is the profiles of Re = 10600 and Law and Wang (2000) as well as the profiles of Re = 5800 and Webster et al. (2001).

Chapter 5: Results

The results of the evolution of the passive scalar field of the turbulent jets with different Reynolds (Re = 5800 and 10600) issuing into both stagnant and turbulent surroundings are presented and discussed. The scalar concentration results are compared to the jet velocity field reported by Khorsandi (2011) that were performed in the same experimental setup and governing flow-ambient characteristics. Comparing the results of the scalar and velocity fields under the same conditions allows any differences in the evolution of the two fields to be identified.

5.1 Passive scalar dynamics

The passive scalar fields of the turbulent jets were measured while the jet was flowing horizontally at the same vertical distance from both the water surface and the tank's bed. Moreover, the jet was situated at $\frac{y}{M} = 7.3$ far from the RJA (where M is the spacing of the jets of the RJA) to maintain an imposed Turbulent Kinetic Energy (TKE) of $4.4 \frac{cm^2}{s^2}$ throughout the experiments in the turbulent ambient. The axial distance over which the scalar fields were observed was $10 \le x/D \le 70$, to demonstrate the scalar field evolution within the self-similar region of the turbulent jets issuing into a stagnant ambient.

Two jet Reynolds numbers of 5800 and 10600 were considered for the comparison of the scalar field evolution of the jets in presence of the background turbulence. While, the scalar field of a jet with an intermediate Reynolds number of 8200 was investigated in addition to 5800 and 10600 in a quiescent ambient. The higher Reynolds number was considered to be a fully developed turbulent jet and also allowed for a direct comparison to the velocity field results of Khorsandi (2011) and the scalar field results of present study. Moreover, the lower Reynolds number was also chosen to be identical to that of Khorsandi's and allowed for the jet to breakup within the distance under observation.

In general, the results obtained confirmed a fundamental alteration in the scalar field's behaviour in terms of the entrainment mechanism, jet shape, and breakup threshold of the jets issuing into a turbulent surrounding in comparison to the jets emitted into quiescent surroundings. Due to this significant difference, the raw data ensembles associated with the jets issued into the turbulent background required on average a data record 6 times the length as that of the jets emitted into the

quiescent background to converge. In other word, each PLIF experiment in quiescent surroundings recorded 5000 instantaneous images of a cross-section, while, 25000 to 35000 instantaneous images were captured for the same jet in a turbulent background.

Flow visualization of cross-sections of turbulent jets issuing into the turbulent background revealed that these jets tend to meander about the centerline unlike those issuing into quiescent surroundings. Moreover, it was observed that the turbulent surrounding imposes a substantial distortion to the jet structure and significantly erodes the jet's mean momentum as compared to the quiescent ambient. Figure 5.1 demonstrates the ensemble averaged cross-sections of the jets in the quiescent background as well as some instantaneous cross-section samples of jets issued into the turbulent backgrounds.

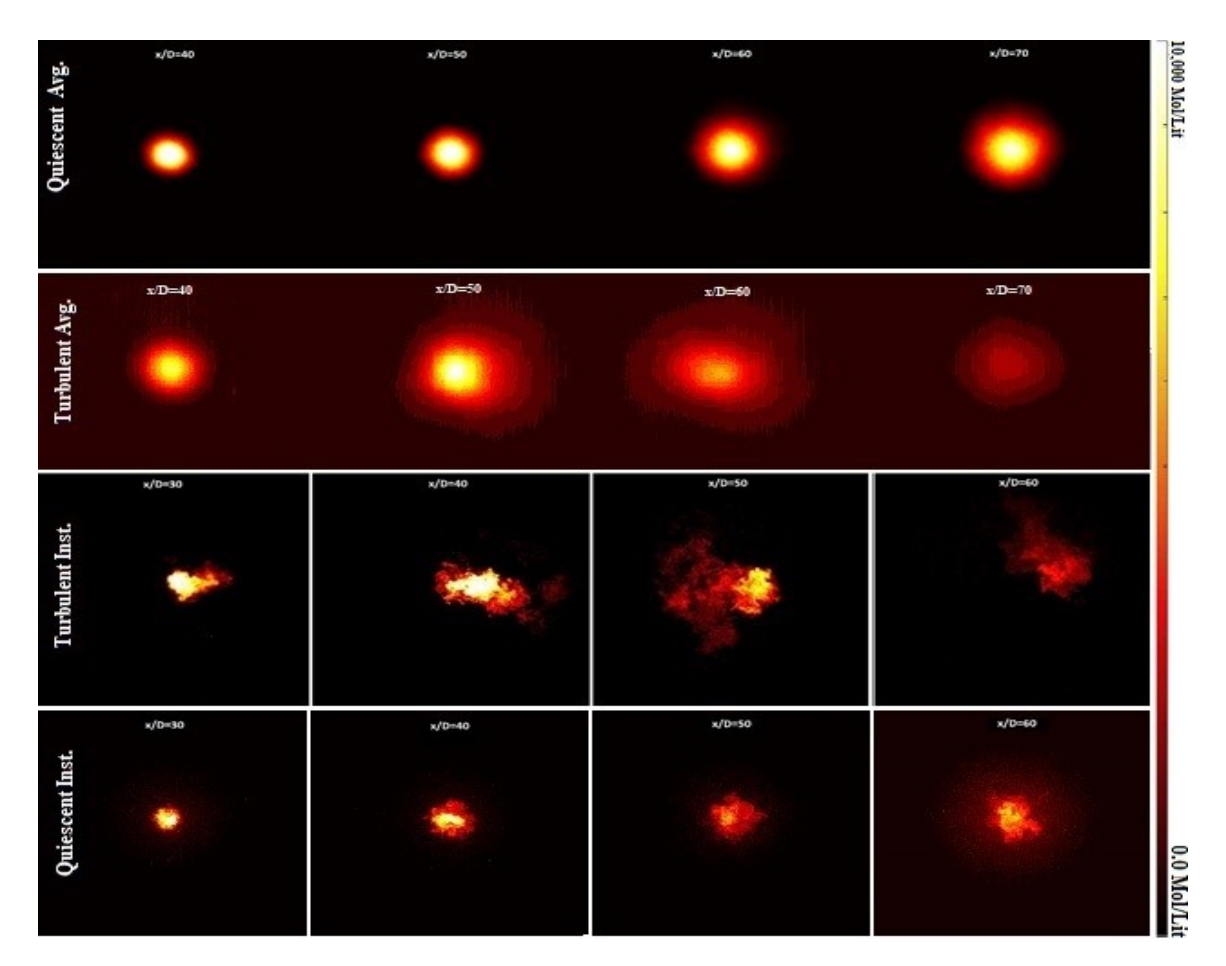


Figure 5.1 Average and instantaneous cross-sections of the turbulent jets (Re = 10600) issuing into a quiescent background, and a turbulent background. [Colour map codes jet-fluid concentration]

5.1.1 Centerline concentration time tracings

Commonly, investigation of the centerline concentration of a turbulent jet, is the basis for understanding the other dynamical features of the jet. In an Eulerian framework, the evolution of the centerline concentration along the jet's streamwise axis can inform interpretations of the jet behaviour in terms of the jet structure at different axial distances, can distinguish between the jet zones, can be used to compare the dynamical characteristics of different jets, can be used to evaluate Reynolds number effects, and so on.

Time traces of the centerline concentration at each cross-section were obtained and normalized by the averaged concentration at that section (${^C_{cl}}/{\bar{c}}$). The results for the jets issued into both quiescent and turbulent backgrounds with different Reynolds numbers are shown in Figures 5.2, 5.3, 5.4 and 5.5.

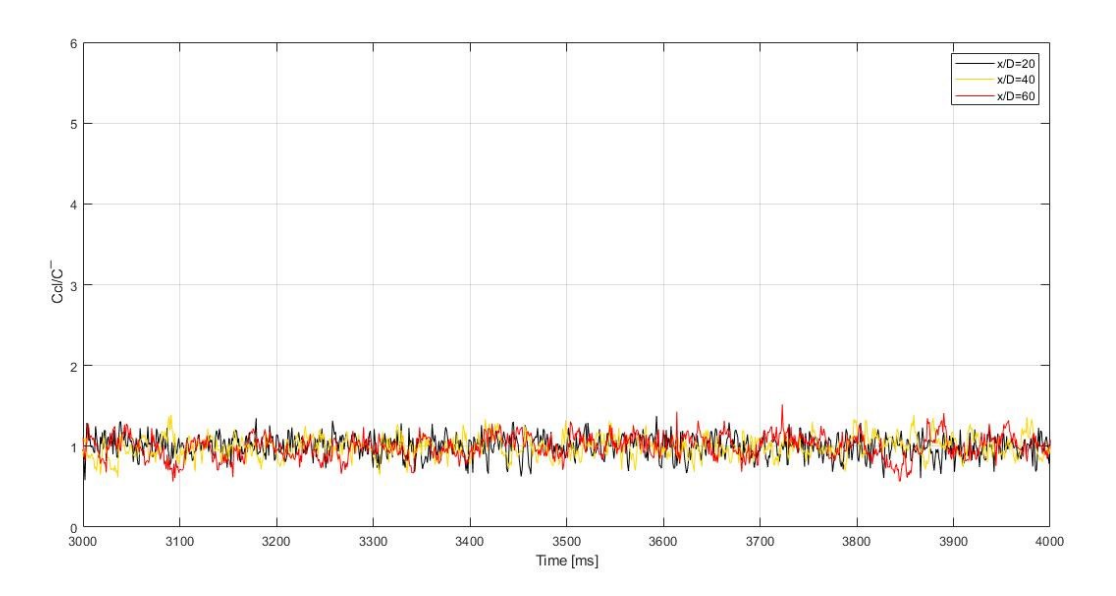


Figure 5.2-Time traces of the centerline concentrations of the Re=10600 jet issued to the quiescent ambient normalized by the averaged concentration (${}^{C_{cl}}/{}_{\bar{c}}$)

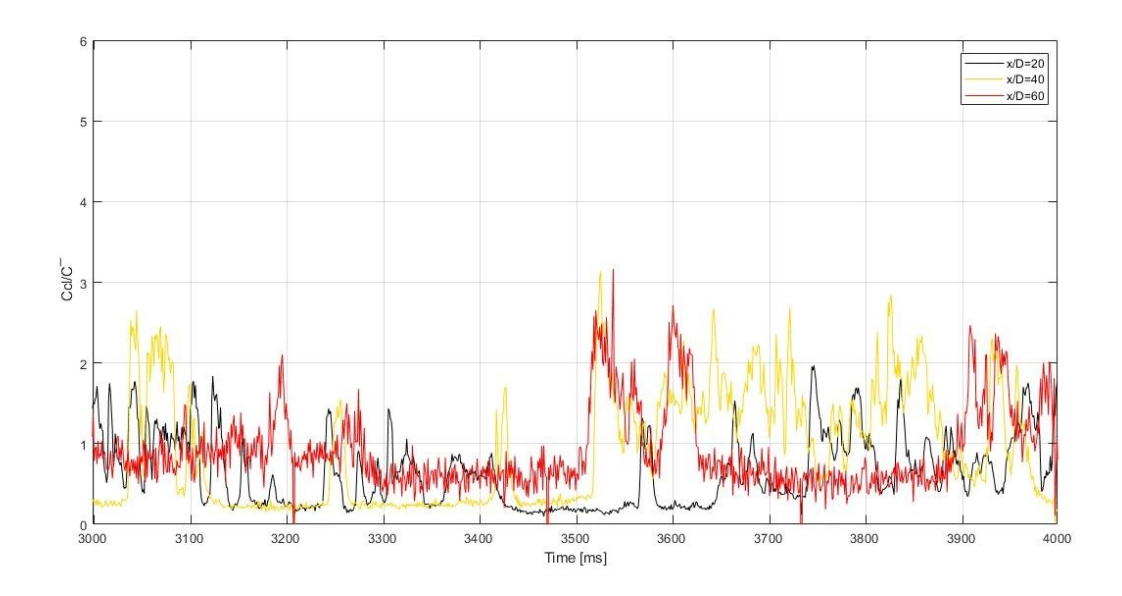


Figure 5.3-Time traces of the centerline concentrations of the Re=10600 jet issued to the turbulent ambient normalized by the averaged concentration $\binom{c_{cl}}{\bar{c}}$

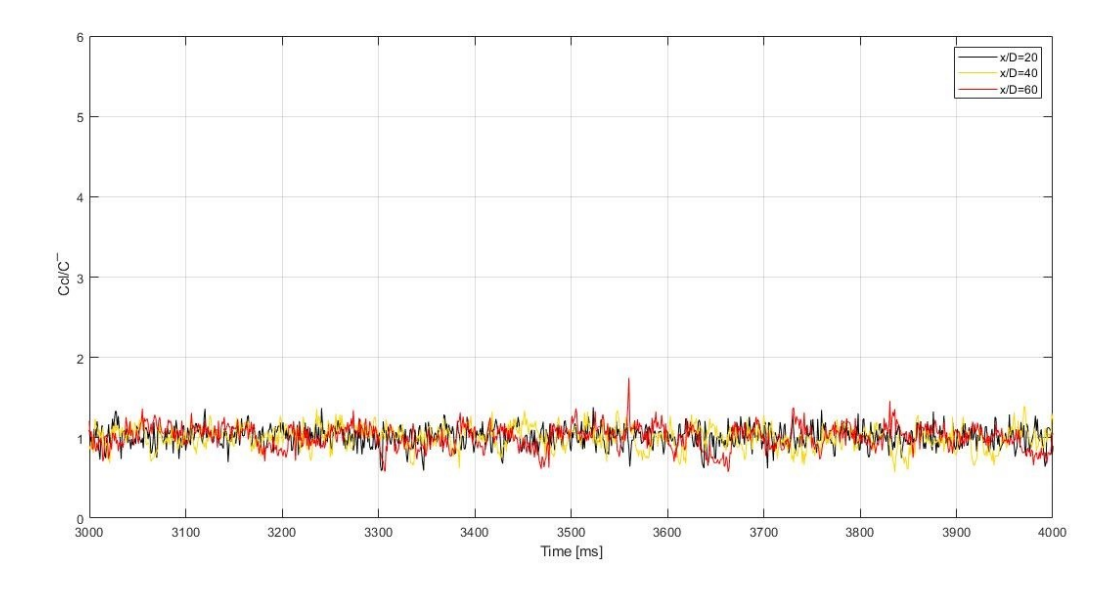


Figure 5.4-Time traces of the centerline concentrations of the Re=5800 jet issued to the quiescent ambient normalized by the averaged concentration $\binom{c_{cl}}{\bar{c}}$

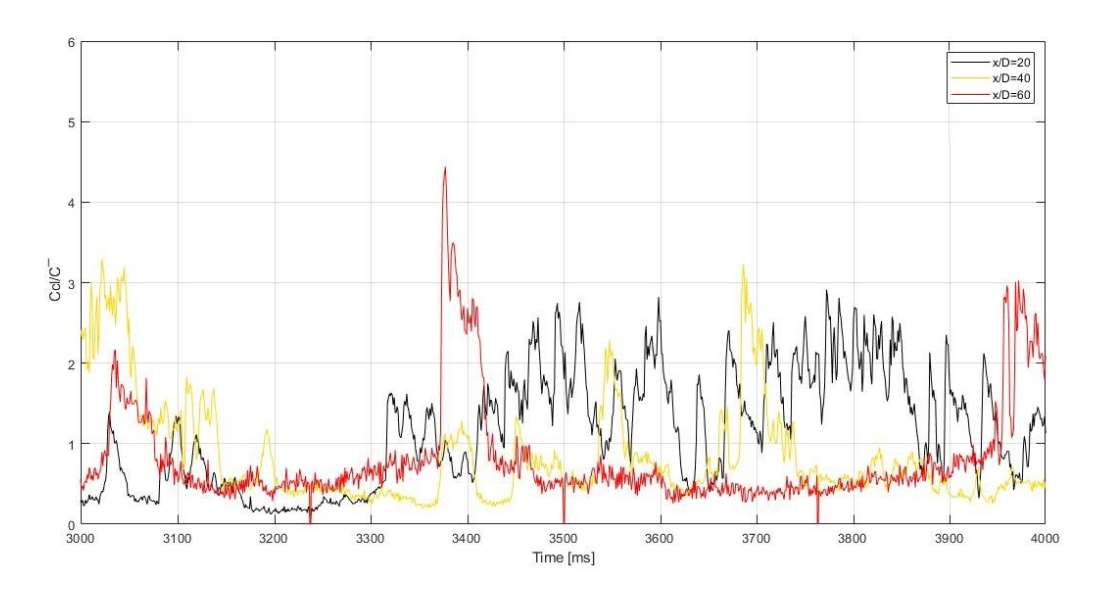


Figure 5.5- Time traces of the centerline concentrations of the Re=5800 jet issued to the turbulent ambient normalized by the averaged concentration (${}^{C_{cl}}/{}_{\bar{C}}$)

Figures 5.3 and 5.5 present the centerline concentration time traces at axial distances of 20, 40 and 60 for the higher (10600) and lower (5800) Reynolds number jets in the turbulent ambient. In the quiescent ambient the concentration fluctuates approximately equally about the mean, with the magnitude of the fluctuations increasing with axial distance. However, in the turbulent ambient, there are greater magnitudes of fluctuations and larger excursions from the mean occur above the mean concentration, as seen in Figures 5.2 and 5.4. In addition, there is a greater variation in the fluctuations as axial distance increases.

5.1.2 Mean centerline concentrations

The evolution of the mean centerline concentrations with axial distance was of interest. The centerline concentrations of the turbulent jets (Re = 5800 and 10600) issuing into both turbulent and quiescent backgrounds were normalized by the initial concentration and averaged (${}^{C_{cl}}/{}_{C_0}$). As shown in the logarithmic plot of Figure 5.6, both Reynolds numbers have to an axial concentration decay rate of x^{-1} . However, at the higher Reynolds number, jet centerline concentrations exhibit slightly lower concentrations than those at the lower jet Reynolds number at the absolute distances given (if they were plotted from the virtual origin they would collapse onto the same curve).

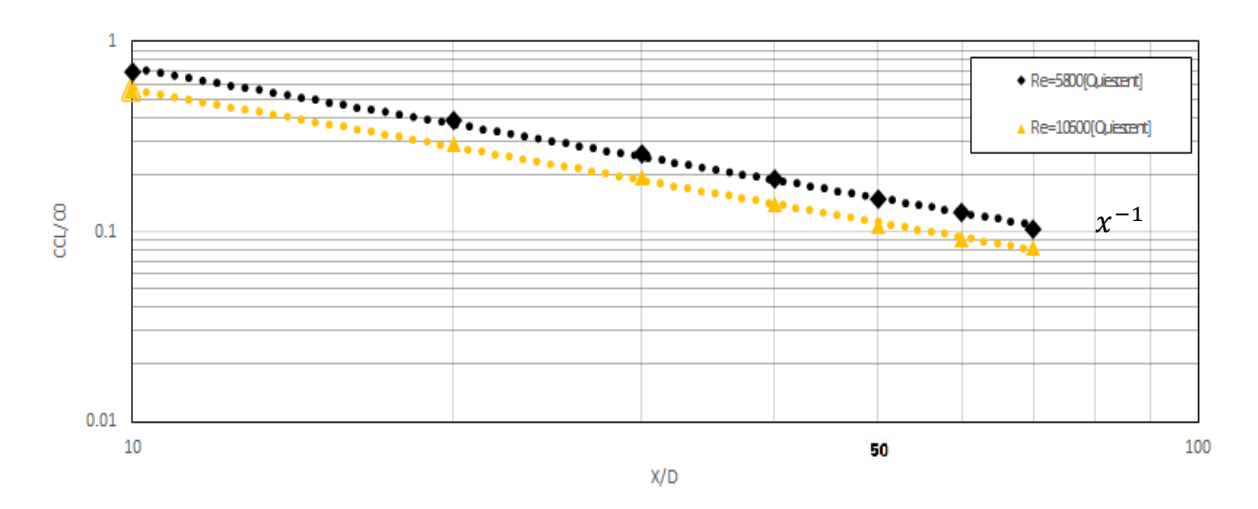


Figure 5.6- Streamwise evolution of the normalized mean centerline concentrations $\binom{C_{cl}}{C_0}$ of the turbulent jets with Reynolds numbers of 5800 and 10600 issuing into quiescent surroundings

The three logarithmic plots in Figures 5.6, 5.7, and 5.8 demonstrate that the non-dimensionalized mean centerline concentrations of the jets emitted into the quiescent ambient decay in the streamwise direction at a constant rate of x^{-1} independent of the Reynolds number. However, the jets with higher Reynolds exhibit a slightly lower centerline concentration. On the other hand, the jets subjected to the turbulent ambient demonstrate a steeper decay rate of centreline concentrations than the same jets into the quiescent ambient, while, the centreline concentrations of the jet with lower Reynolds number decays at a faster rate (near $x^{-1.7}$) than the jet with higher Reynolds number (near $x^{-1.2}$). Notably, an identical ambient turbulence created with the RJA and having a TKE at the centreline of the jet of $4.4 \frac{cm^2}{s^2}$, was imposed at both jet Reynolds numbers.

These results indicate that the jet with Reynolds Number of 5800 was impacted both more and closer to the jet outlet by a $4.4 \frac{cm^2}{s^2}$ TKE background turbulence in comparison to the jet with the Reynolds number of 10600 (Gaskin et al. (2004) and Khorsandi et al. (2013)).

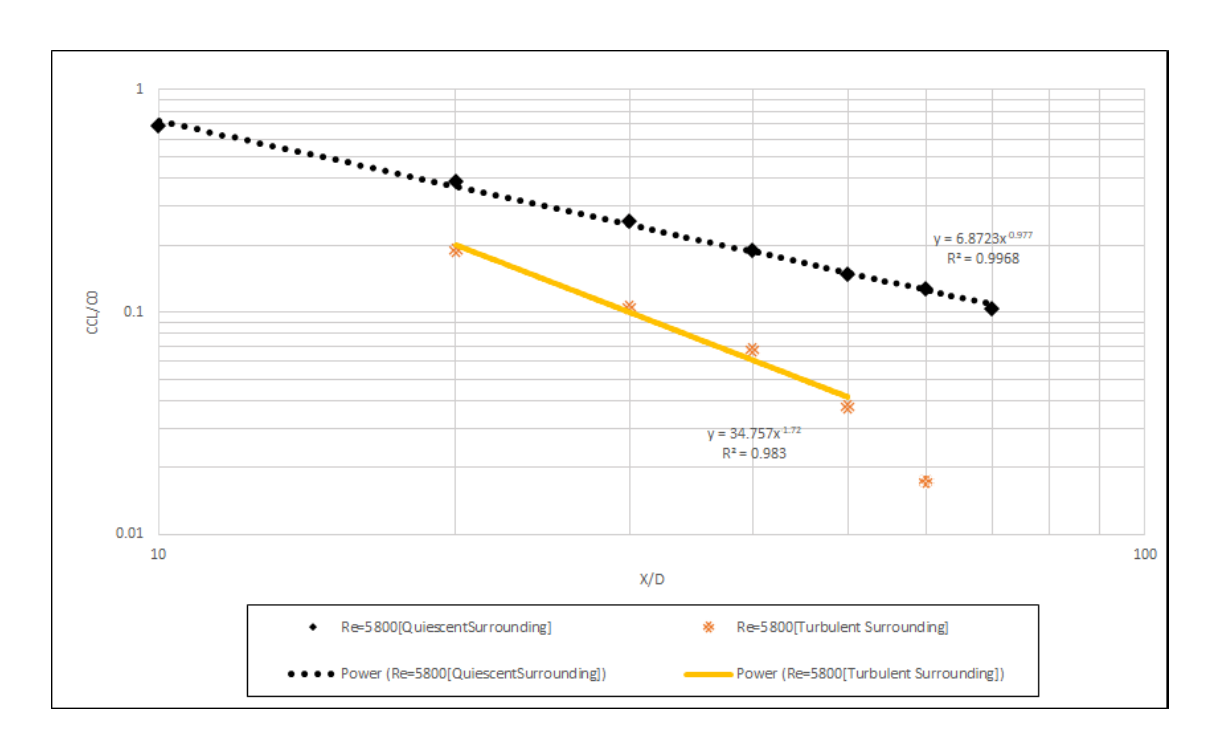


Figure 5.7- Streamwise evolution of the normalized mean centerline concentrations ($^{C_{cl}}/_{C_0}$) of the turbulent jet of Re=5800 issuing into both turbulent and quiescent ambient

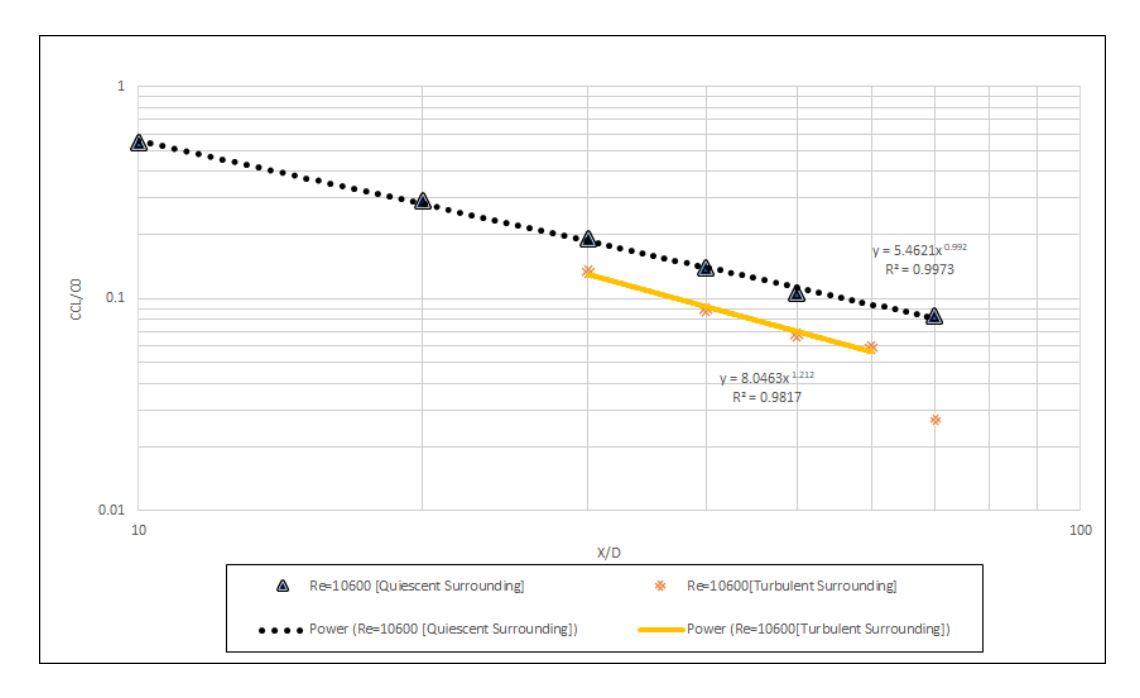


Figure 5.8- Streamwise evolution of the normalized mean centerline concentrations ($^{C_{cl}}/_{C_0}$) of the Re=10600 turbulent jet issued into both turbulent and quiescent ambient

The evolution of the centreline mean concentration with axial distance can be fitted to a straight line (i.e. power law decay) either considering all points or considering only points up the distance at which the jet structure decays (i.e. the breakup location of the jet) (see Table 4.1). Alternatively, a logarithmic equation can be fitted to all points as the best possible fit for both Reynolds (Figures 5.9 and 5.10). However, as the jet behaviour changes once the jet structure (as indicated by the complete decay of jet velocity in the data of Khorsandi et al. 2013) decays, the rate of decay of the concentration is that given by the power law equation (as predicted by the theory) fitting the points up to the point of jet breakup (x/D = 50 for Re = 5800 and x/D = 60 for Re = 10600) and then changes for distances beyond.

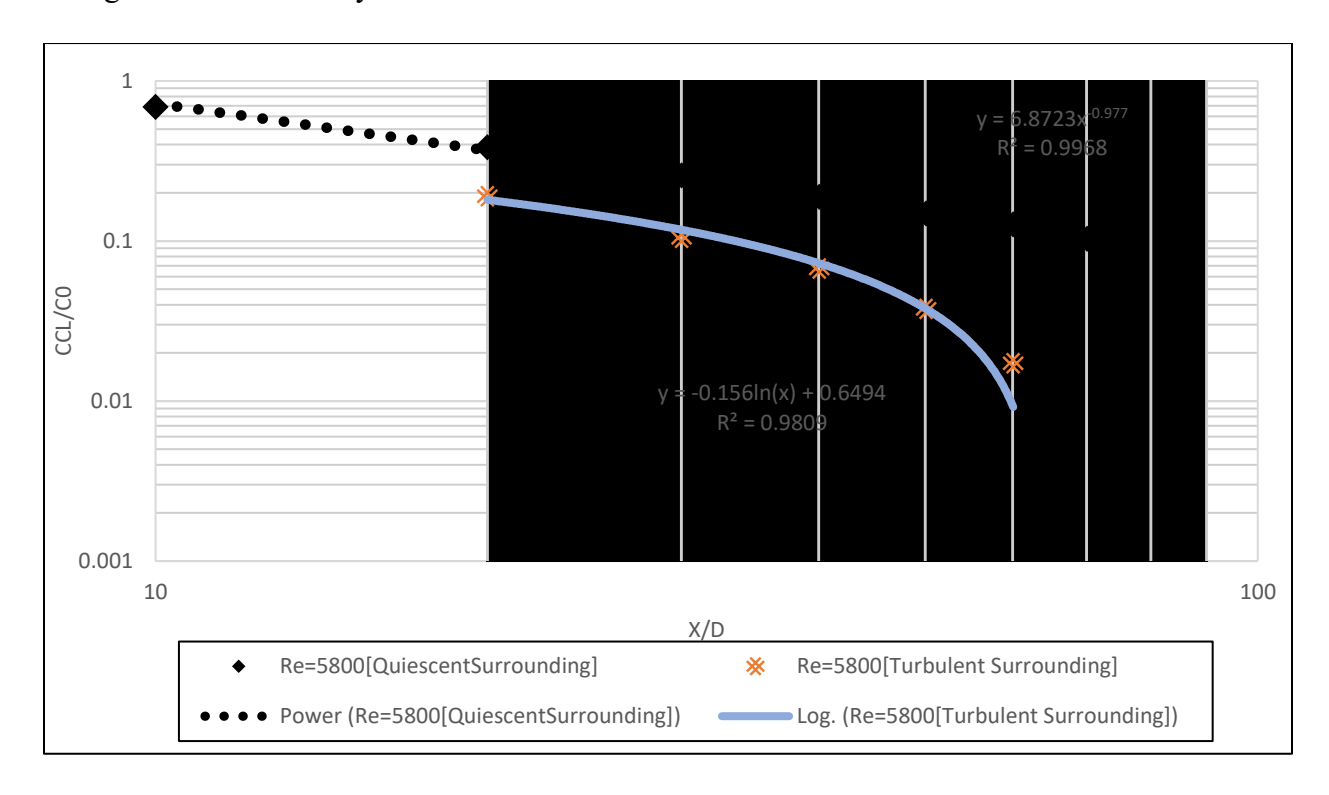


Figure 5.9 Streamwise evolution of the normalized mean centerline concentrations (C_c\(\mu \colon \cdot \cdo

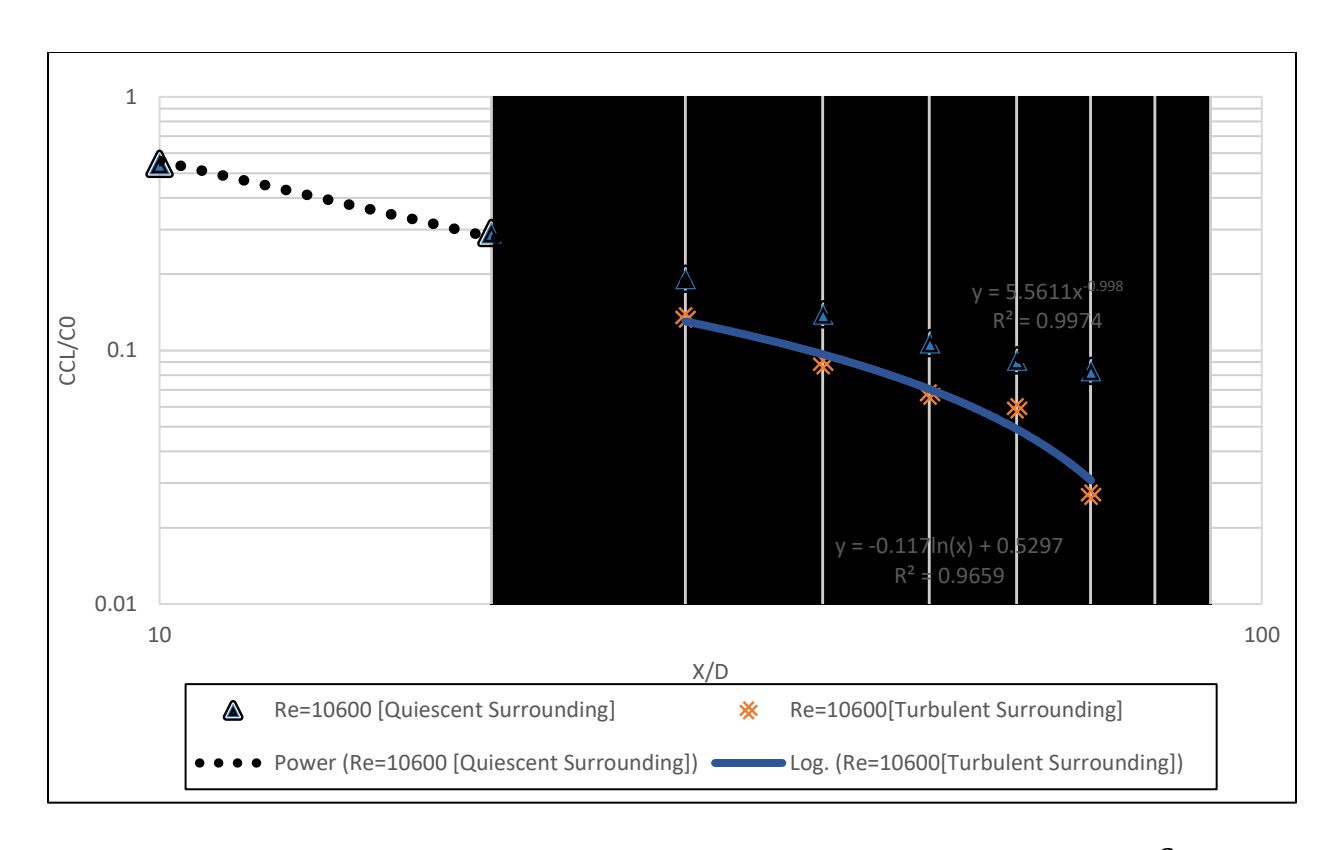


Figure 5.10 Streamwise evolution of the normalized mean centerline concentrations $\binom{\mathcal{C}_{cl}}{\mathcal{C}_0}$ of the Re=10600 turbulent jet issued into both turbulent and quiescent ambient. Best fit curve including point after breakup [Re=10600 into turbulent ambient]

Table 5.1: Downstream evolution of centreline mean concentration

Jet Reynolds number	5800		10600	
Ambient	Q	T	Q	T
Power law growth	x^{-1}	$x^{-1.7}$	x^{-1}	$x^{-1.2}$
Logarithmic equation (best fit)	$C_{cl} = -0.156 \ln(x) + 0.65$		$C_{cl} = -0.117 \ln(x) + 0.53$	
R ² value	0.98		0.98	

5.1.3 Mean radial concentration profiles

The mean radial concentration profiles obtained from a vertical section of a turbulent jet's crosssection will allow for observation of the effects of the turbulent ambient on the jet as compared to a quiescent ambient. Therefore, the mean radial concentration profiles of each cross-section are plotted for the jets issuing into both a quiescent and a turbulent ambient (Re of 5800 and 10600) in Figure 5.9. The radial profiles from $20 \le \frac{x}{D} \le 60$ are shown for the jet at the lower Reynolds number and from $30 \le \frac{x}{D} \le 70$ for the jet at the higher Reynolds number. (Note that the centreline of the jet does not always occur at x=0 due to a slight angle offset of the jet).

It can be observed that the turbulent ambient imposes a considerable disorder to the jet structure visible in the greater variability of the mean radial concentration profiles as compared to the quiescent ambient in spite of a data set that is five times longer. More variability is observed as axial distance increases and it is also greater for the jet at the lower Reynolds number.

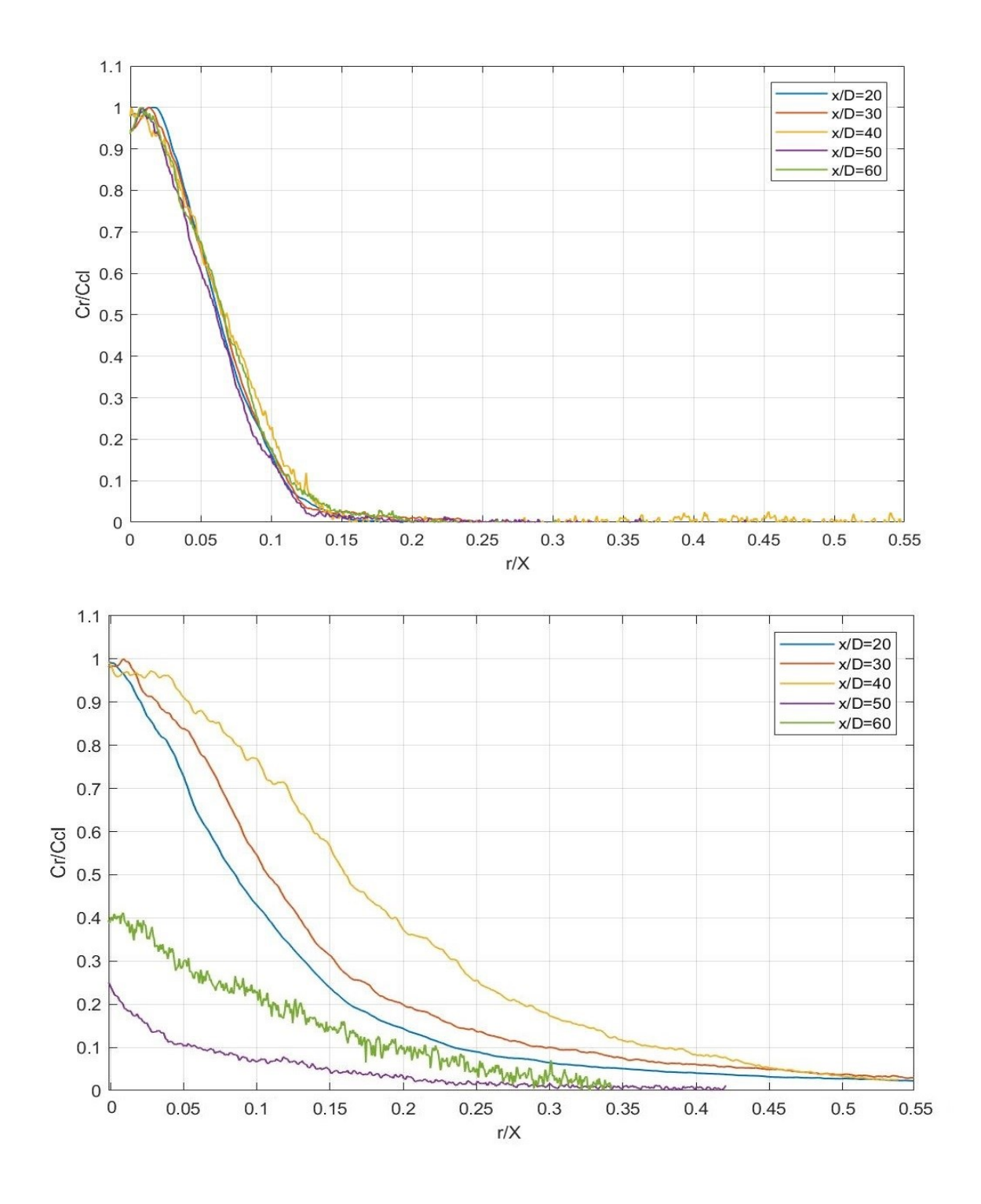


Figure 5.11 Radial profiles of mean concentration of the turbulent jet at Re=5800 (a) issuing into the quiescent ambient and (b) issuing into the turbulent ambient. [$^{\chi}/_{D}$ = 20, 30, 40, 50, and 60 respectively]

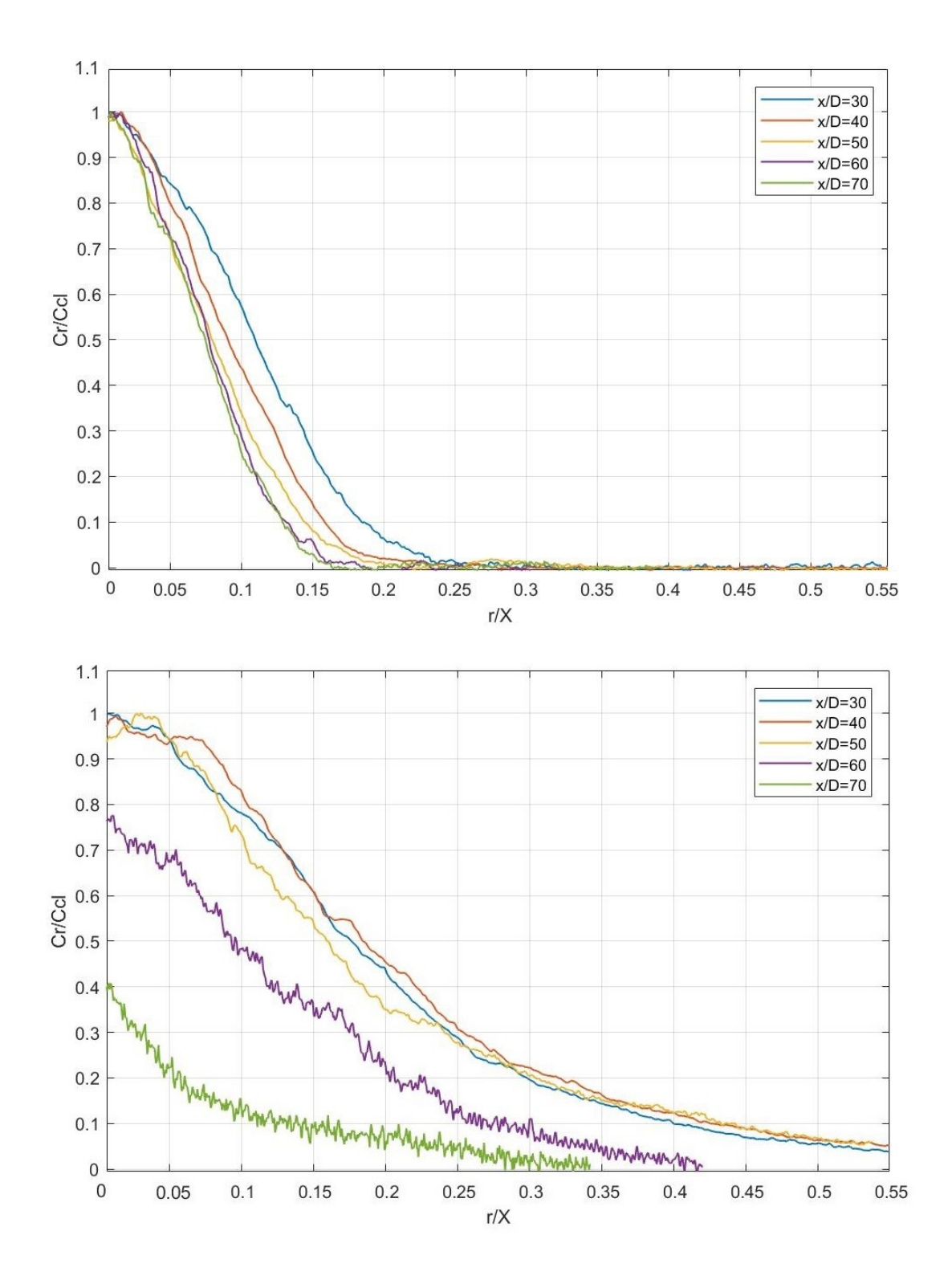


Figure 5.12 Radial profiles of mean concentration of the turbulent jet at Re=10600 (a) issuing into the quiescent ambient and (b) issuing into the turbulent ambient. [$^{x}/_{D}$ = 30, 40, 50, 60, and 70 respectively]

5.1.4 Half-width of the mean concentration profile

The half-width of the mean concentration profile is defined as the radial distance at which the concentration equals half of the centreline concentration value (where $^{C}/_{C_{cl}} = ^{1}/_{2}$). As shown in the following figure, the half-widths were normalized by the jet diameter $^{r_{1/2}}/_{D}$) and plotted versus the normalized streamwise axial distances $^{x}/_{D}$).

The growth of the half-width indicates the streamwise width growth of the jet, which can be compared in the quiescent and turbulent ambient. In Figure 5.13a, the width growth of the jet with streamwise distance at each Reynold number (5800 and 10600) in both quiescent and turbulent ambient are plotted and a linear best fit shown. The jet in a quiescent ambient has a width growth that is proportional to axial distance (x^1) as expected. The jet in a turbulent ambient grows at a faster rate and the rate is greater for the lower Reynolds number jet, with $x^{1.21}$ for Re = 10600 and with $x^{1.35}$ for Re = 5800, likely due to the lower initial momentum of the lower Reynolds number jet. It can be observed that the width growth deviates from these curves at the last point as this is beyond the breakup point of the jet. This change in behaviour was also seen in the evolution of the mean centreline concentration with axial distance. A non-linear best fit curve including the point beyond the breakup point (i.e. up to the furthest axial distance) gives, $y = 1.25e^{0.046x}$ and $y = 0.894e^{0.044x}$ for Re=5800 and 10600 respectively, as shown in Figure 5.13b.

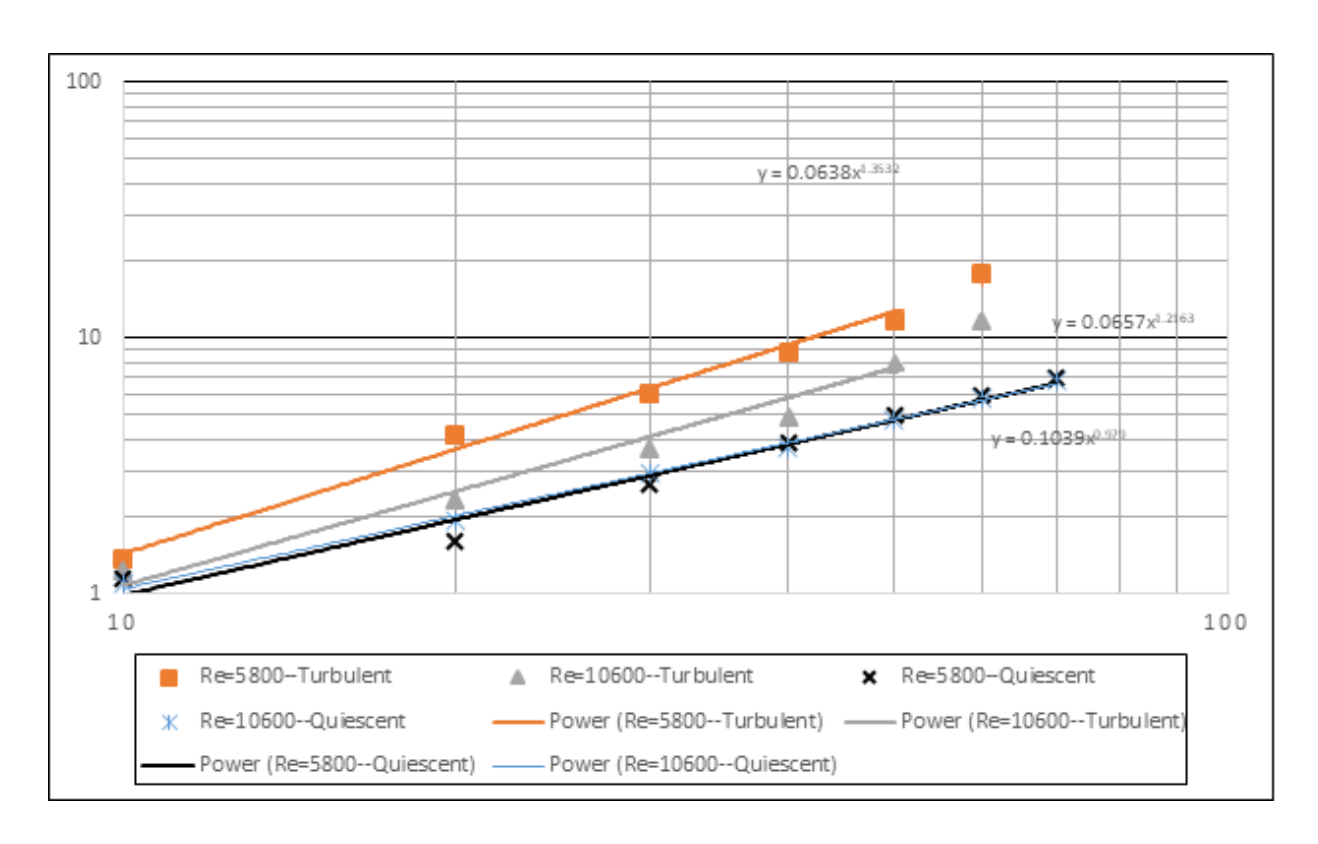


Figure 5.13a Downstream evolution of the half-width of the scalar field of the turbulent jet (Re = 10600 and Re = 5800) in turbulent and quiescent ambient.

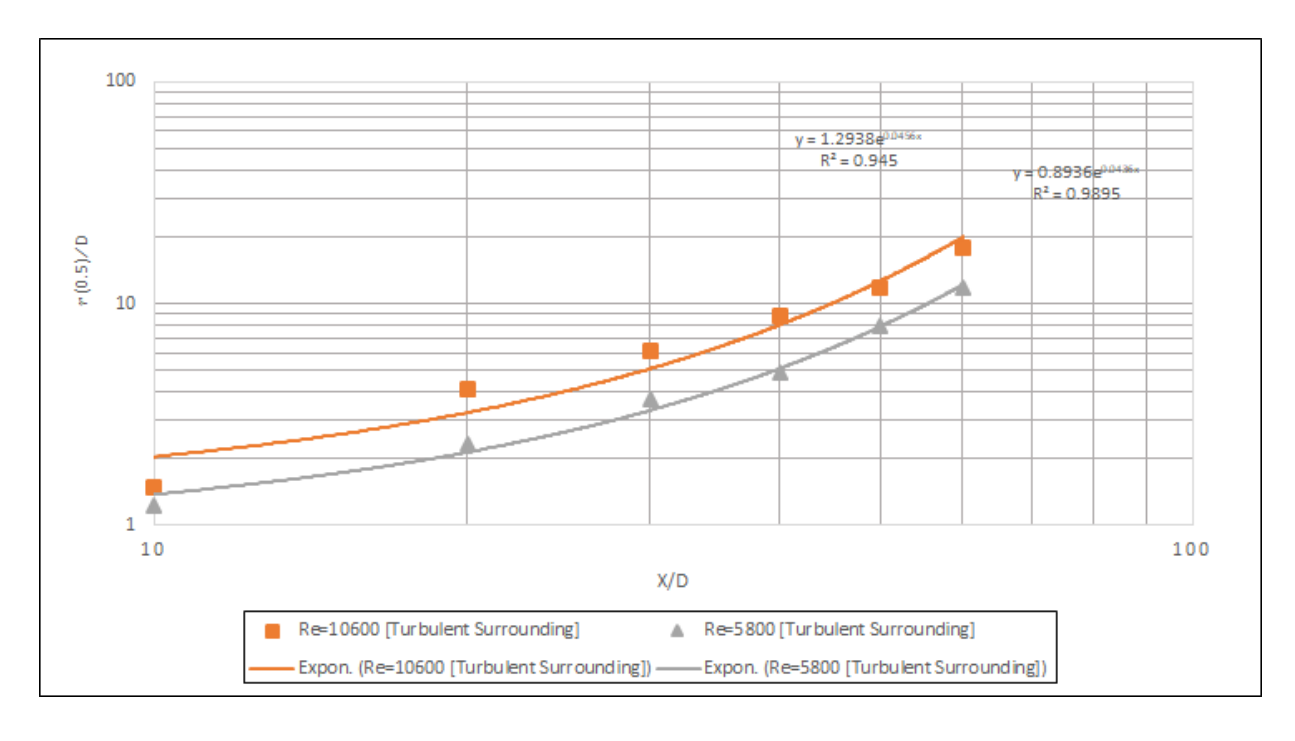


Figure 5.13b Best fit curves of the half-width of the scalar field of the turbulent jet (Re = 10600 and Re = 5800) including anomalous furthest axial distances

5.1.5 Cross-sectional center of mass

Observations of the streamwise trajectory of the turbulent jets subjected to a turbulent ambient shows its path meandering about its centerline due to the larger eddies of the ambient turbulence. Therefore, an assessment of the meandering of the jet's streamwise trajectory was of interest. The simplest assessment of the meandering of the jet is the changing location of the jet's center of mass (as when meandering it will not coincide with the geometric centre). In addition, knowing the centre of mass of the cross-sections will allow other characteristics of the jet's behaviour in the turbulent ambient relative to its centre of mass to be revealed, such as the growth of the radius of gyration.

In Figure 5.14, the streamwise evolution of the magnitude of the meandering of the scalar field's cross-sectional center of mass is shown in a scatter plot for the turbulent jet at a Reynolds number of 5800 in both turbulent and quiescent ambient. It is clear seen that the centre of mass of the jet in a quiescent ambient remains very close to the geometric centre, while that of the jet in the turbulent ambient shows much greater scatter who magnitude increases in the downstream axial direction.

It can be clearly observed that the meandering of the jet increases in the axial direction. Moreover, a sort of discontinuity is observed in the behaviour of the jet in the turbulent ambient. This can be shown by plotting the location of the centre of masses as a line plot rather than as a scatter plot as seen n Figure 5.15 for the cross-sections at x/D of 30 and 60. At an axial distance of 30, these plots are the same, indicating that the jet itself is continuous in the axial direction. However, at the axial distance of 60, the plots are different, with the line plot returning to some point in the lower centre left corner. Analysis revealed that the centre of mass was located here when the total mass in the cross-section was close to zero, indicating that the jet structure had broken and there was a lack on continuity of the jet in the axial direction due to the large radial displacement of the jet due to its meandering path.

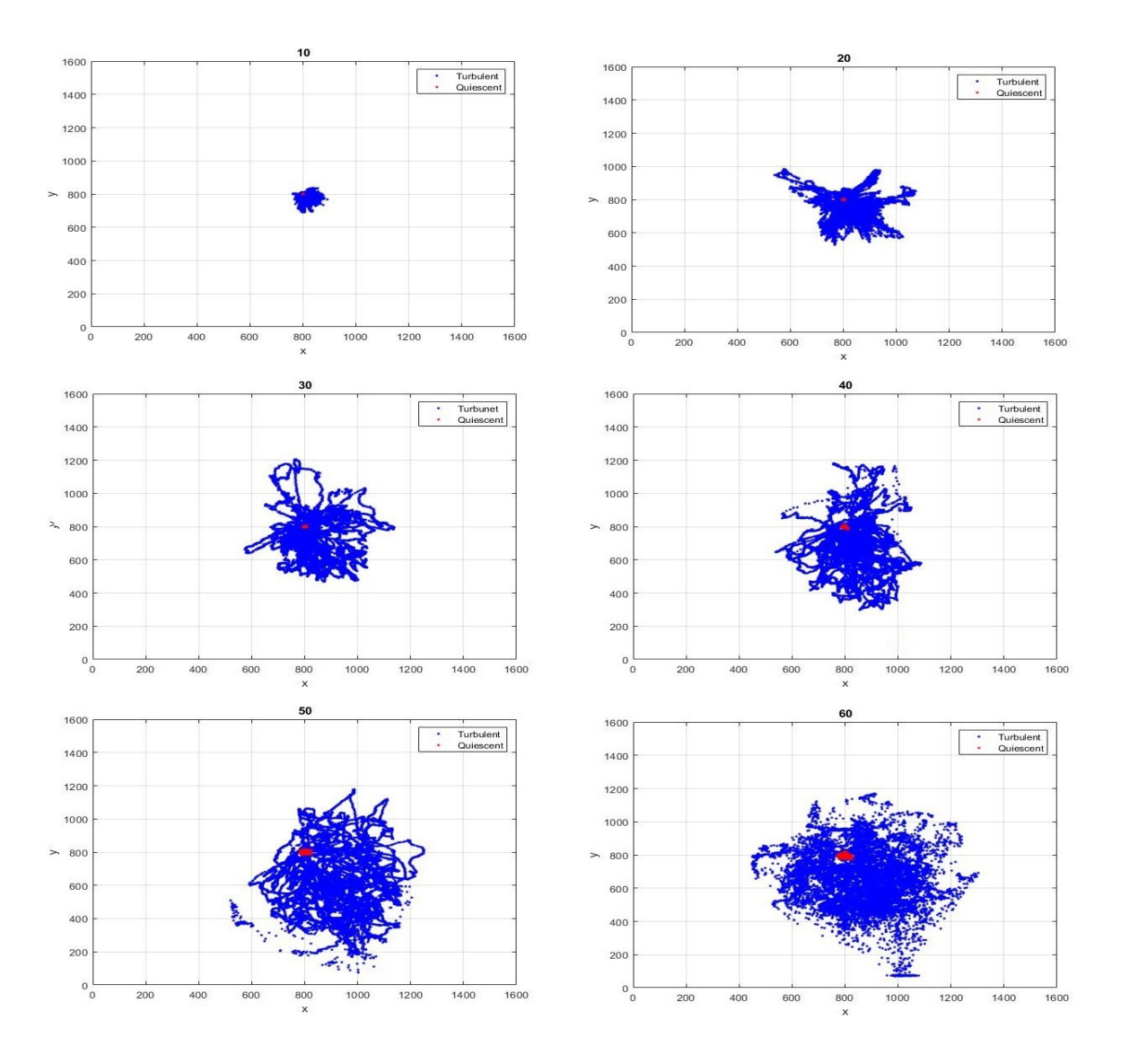


Figure 5.14 Streamwise evolution of the radial position of the centre of mass of cross-sections of the scalar field for a turbulent jet of Re = 5800

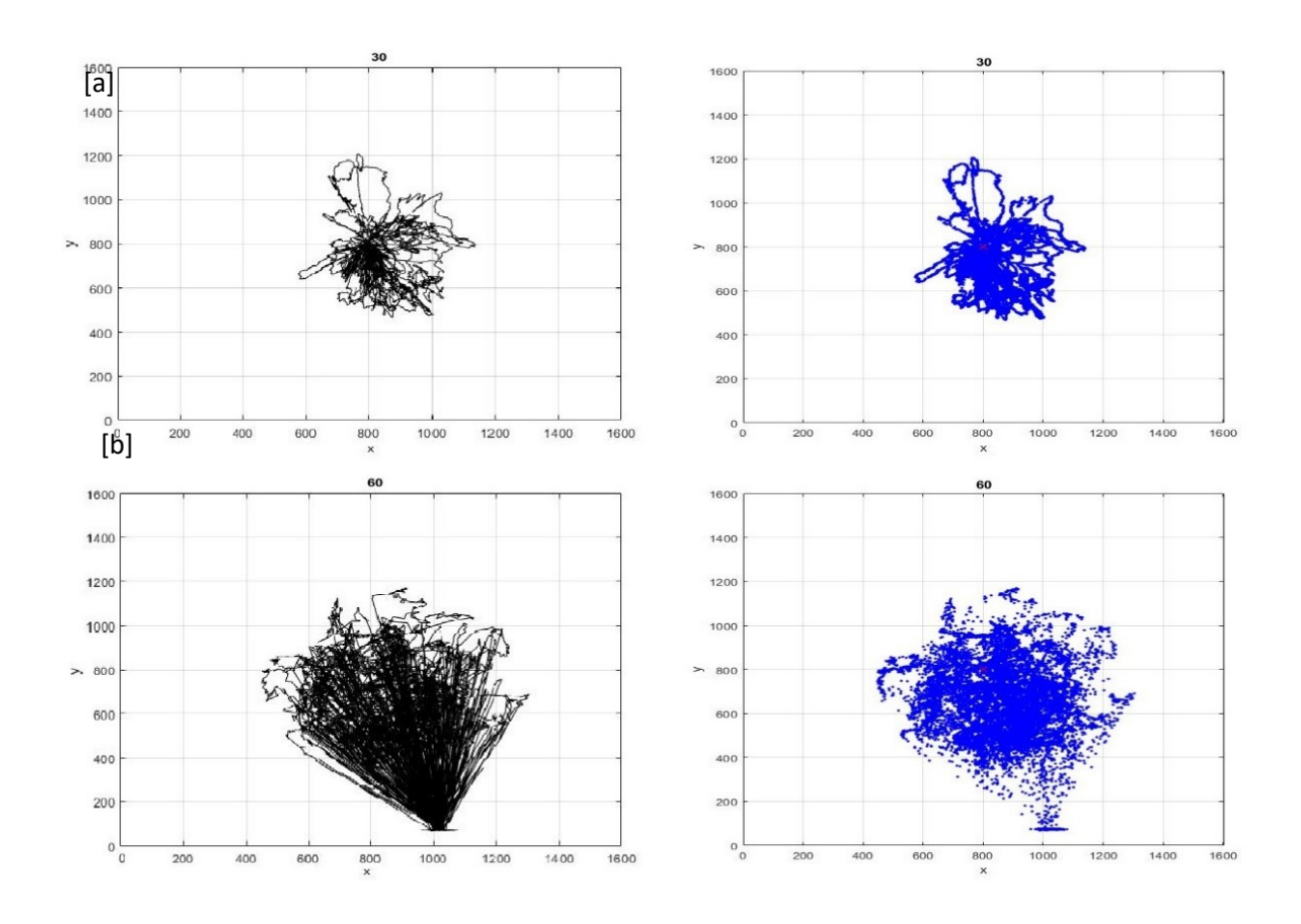


Figure 5.15 Comparison of the center of mass position plots of (a) x/D=30 and (b) 60 of the Re=5800 jet plotted as a line plot and as a scatter plot.

5.1.6 Cross-sectional radius of gyration

The apparent width growth of the jet presented in section 5.1.4, is due to a spatial averaging of the jet over time. This width growth is then due both to the increase in the width of the jet at that axial distance and to the meandering of the jet path (displacement of the jet cross-section from the jet exit centerline axis) at that instant due to the larger eddies of the turbulent ambient. The radius of gyration of the scalar concentration in a jet cross-section can be used to assess the expansion of the jet relative to its centre of mass. The growth in the radius of gyration of the jet in the turbulent ambient can be compared to that in the quiescent ambient to determine the effect of the ambient turbulence on the width growth of the turbulent jet structure relative to its centreline path.

In Figure 5.16, the non-dimensionalized average radius of gyration of the jet (R_G/D) is plotted versus the non-dimensionalized axial distance (x/D). For the jet at both Re = 10600 and 5800 in the quiescent ambient, the data collapse onto the same curve varying with non-dimensionalized axial distance as $\binom{x}{D}^{0.6}$. When the jet is released into a turbulent ambient, the normalized radius of gyration still varies as $\binom{x}{D}^{0.6}$, however the radius of gyration is greater, and the increase is greater for the lower Reynolds number. Thus, the lower Reynold number jet is more affected by the ambient turbulence (at this level). In addition, at the greatest axial distance beyond the point at which the jet breaks up, x/D = 50 for Re = 5800 and x/D = 60 for Re = 10600, the growth of the jet radius of gyration has decreased and no longer follows the same curve (at x/D = 50 for Re = 5800 and at x/D = 60 for Re = 10600). The variation with time of the radius of gyration for x/D = 50 shows an abrupt change in magnitude due to the larger eddies causing a disruption in the jet path.

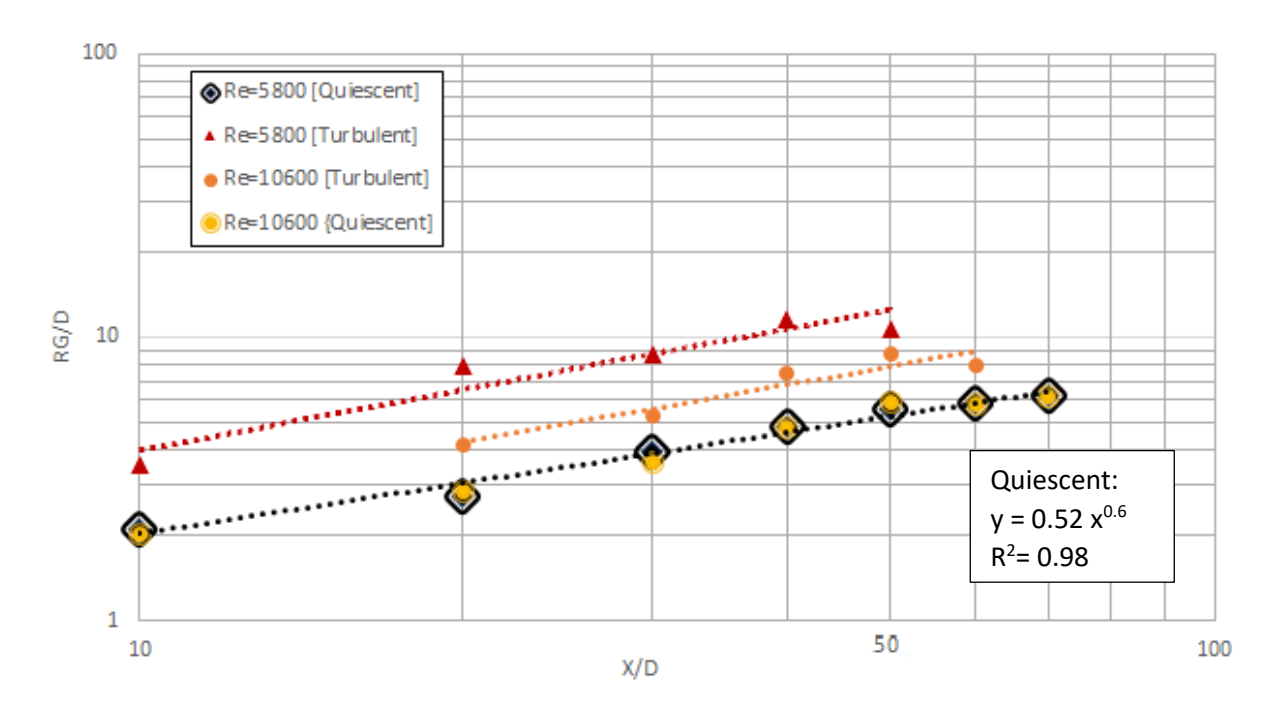


Figure 5.16 Downstream evolution of the dimensionless radius of gyration of turbulent jets of Re = 10600 and 5800 issuing into quiescent and turbulent ambient.

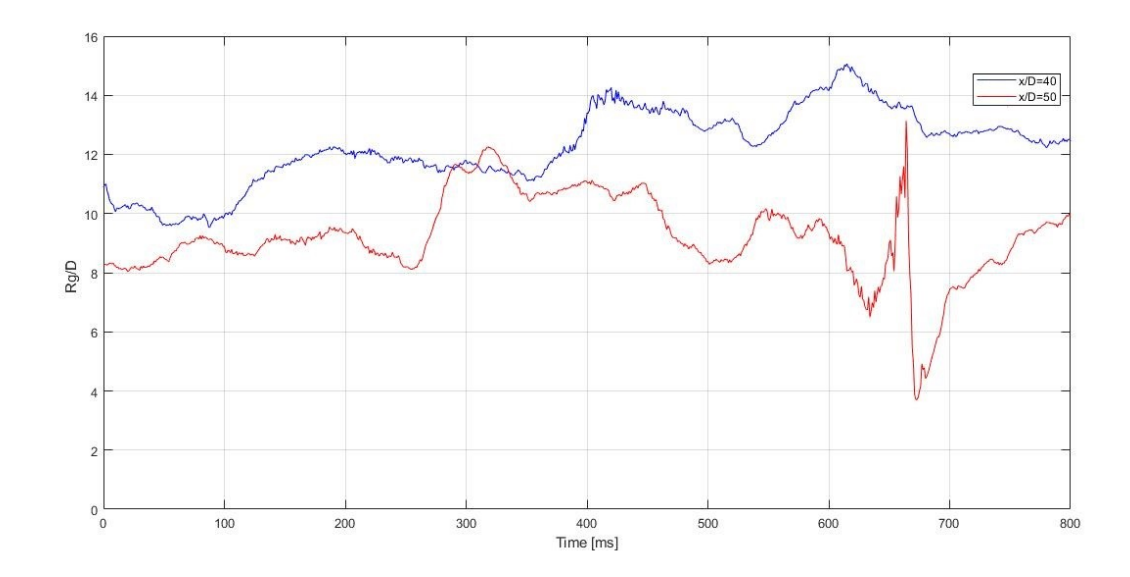


Figure 5.17 Time traces of radius of gyrations of the jet of Re=5800 issued at the turbulent Background at streamwise axial distances of x/D=40 and 50 (only covering the middle 25 sec interval.)

5.1.7 Cross-sectional shape factor

Throughout the experiments, it was observed that the cross-sectional shape of the jets changed becoming less round with increasing axial distance. Moreover, the non-roundness of the jet was greater for the jets in a turbulent ambient as compared to a quiescent ambient. To investigate this, the circularity shape factor, as it is the closest fit to the cross-sectional shape of a turbulent jet, was chosen. The circularity of the jet was found to be slightly less than 1 at the nozzle's exit (while a perfect circle's circularity is equal to 1).

The circularity of each jet image at all cross-sections was calculated. Thereafter, the averaged cross-sectional circularity values were normalized by the circularity of the jets at zero axial distance. The normalized circularities of the jets at both Reynolds number in both quiescent and turbulent ambient were plotted versus the non-dimensionalized axial distance in Figure 5.18. to illustrate the shape factor evolution of the jets while demonstrating the imposed transformation due to the turbulent ambient in compare to the quiescent ambient.

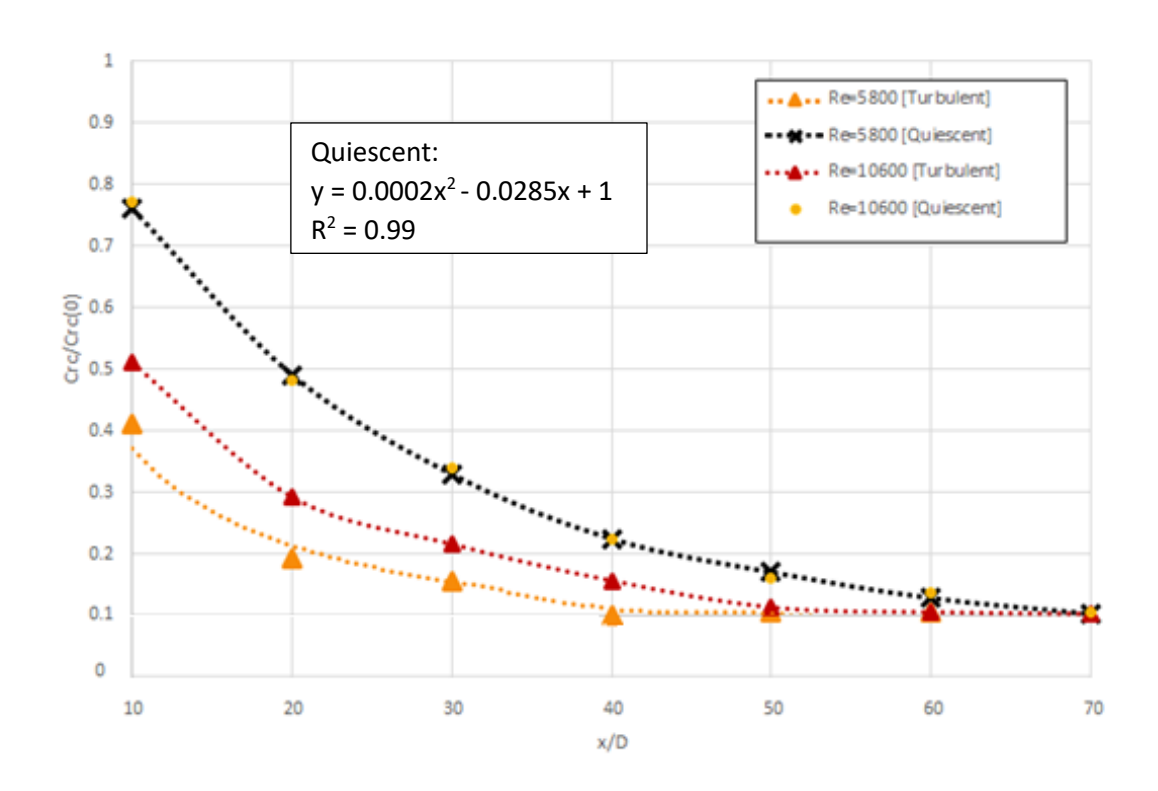


Figure 5.18 Streamwise evolution of the cross-sectional shape factor of turbulent jets of Re=5800 and Re=10600 issuing into both quiescent and turbulent ambient.

Self-similarity of the jets in the quiescent ambient is seen, while the shape factor decreases with axial distance with an asymptote of 0.1. In the turbulent ambient, the shape factor is lower than for the quiescent case and lower for the lower Reynolds number jet, indicating a greater effect by the turbulent ambient in this case. Again, the shape factor has an asymptote of 0.1. The shape factor reaches the value of 0.1 at the point of breakup for the jets released into the turbulent ambient (x/D = 50 for Re = 5800 and x/D = 60 for Re = 10600).

5.3 Comparison of the velocity and concentration fields

The correlation between the velocity vector field and the passive scalar field of the turbulent axisymmetric jets subjected to both quiescent and turbulent ambient were investigated. The variation of the centreline mean velocity with axial distance, obtained from Khorsandi (2011), was compared to the variation in of centreline mean concentration. The two sets of data are both for jet Reynolds numbers of 10600 and 5800 obtained at the same axial distances from experiments

performed in in the same laboratory and hence having the same quiescent and turbulent ambient condition. The mean centerline velocities were non-dimensionalized by the initial velocity at the jet exit and the concentrations non-dimensionalized by the concentration at the jet exit. In Figure 5.19 and 5.20, the centreline velocity is plotted against the centreline concentration at each cross-section. The ratio of the mean centreline velocity to mean centerline concentration in a quiescent ambient is constant with axial distance with a value of 1:0.97 for the jet with Re = 5800 and 1:1.4 for Re = 10600.

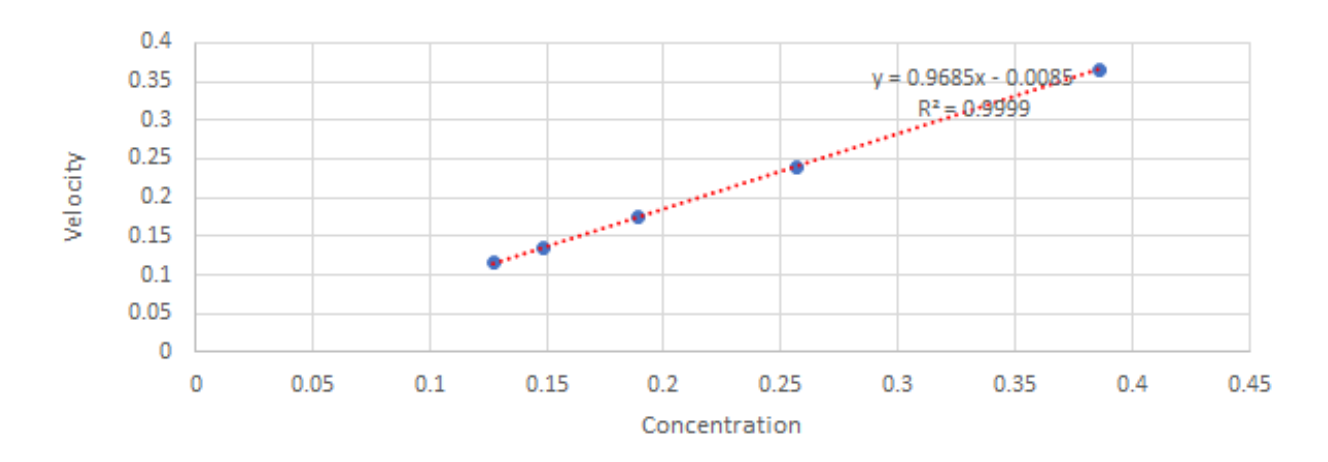


Figure 5.19 Linear regression relation between the mean centerline passive scalar and velocity fields of the turbulent jet with the Reynolds number of 5800 [at streamwise normalized axial distances of 20, 30, 40, 50, and 60(quiescent ambient]

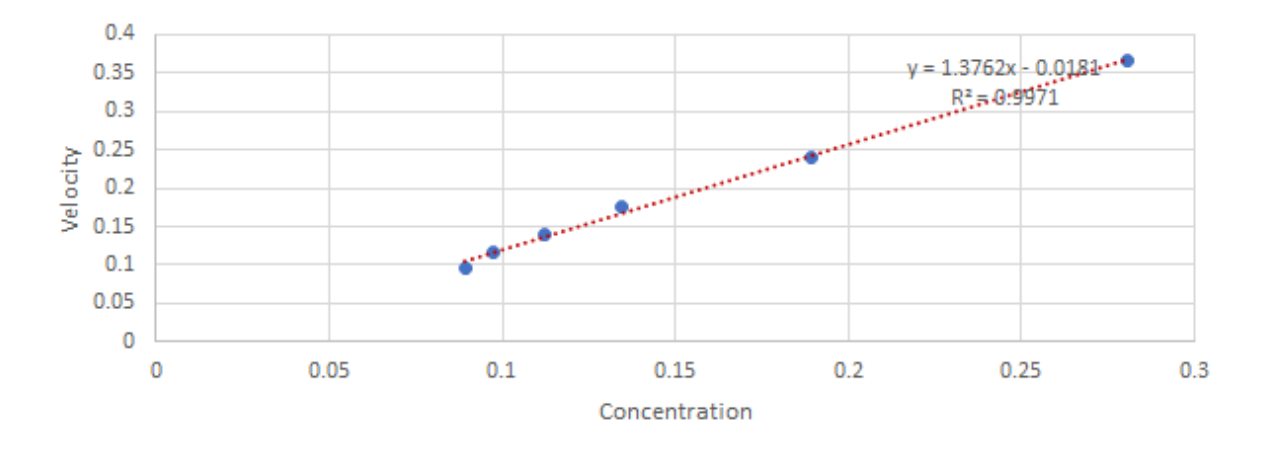


Figure 5.20 Linear regression relation between the mean centerline passive scalar and velocity fields of the turbulent jet with the Reynolds number of 10600 [at streamwise normalized axial distances of 20, 30, 40, 50, 60, and 70 (quiescent ambient)]

For the jets issuing into a quiescent ambient, both mean centreline velocity and concentration decay as a function of x^{-1} , as seen in Fig. 5.21 for the jet at Re = 10600. The same trend was seen for the Re = 5800 jet.

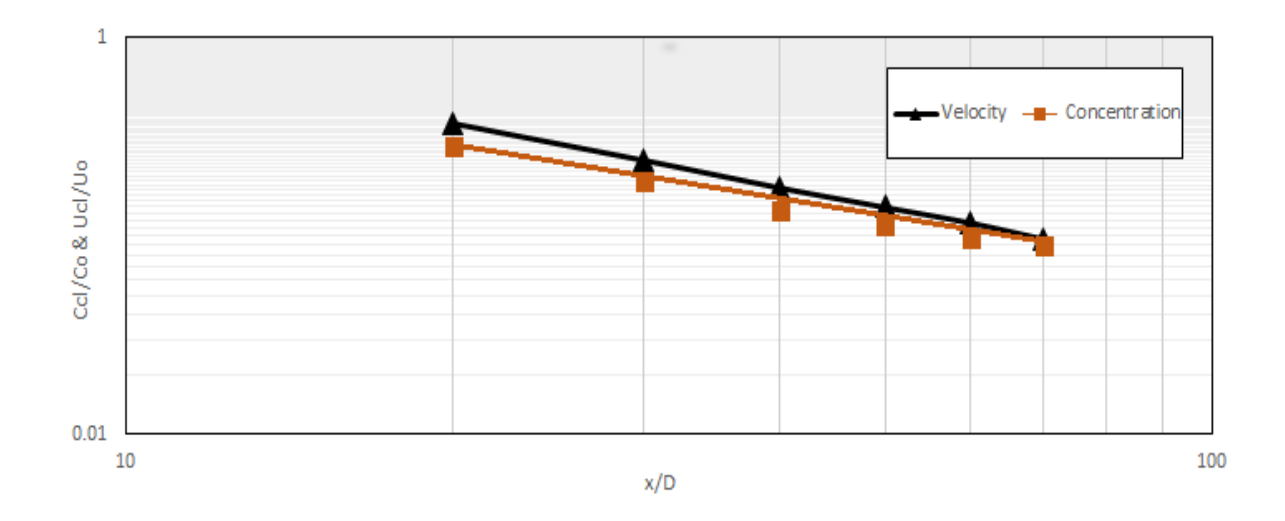


Figure 5.21 comparison of mean centerline velocities and concentrations of the turbulent jet with Reynolds number of 10600 subjected to the quiescent surrounding [at streamwise normalized axial distances of 20, 30, 40, 50, 60, and 70]

For the jets issuing into the turbulent ambient, the plots of the streamwise variation of the mean centerline velocities and concentrations for the jets at Re = 5800 and 10600 are presented Figures of 5.22 and 5.23, respectively.

It is clear that in the turbulent ambient, the mean centreline velocity decays faster than the mean centreline concentration, as shown in Table 5.2. The rate of decay of the velocity is greater than that of the concentration, as once the turbulence in the ambient has disrupted the jet, the jet velocity decays to zero. Whereas, when the ambient turbulence disrupts the jet structure, the concentration of the scalar decays more slowly as the scalar remains. Both the concentration and velocity decay rate is greater for the jet with the lower Reynolds number. The difference in the change in the rate of decay results in a different axial distance at which the velocity and concentration decay curves intersect. This intersection point is at x/D of 40 and x/D of 50 for the jets Reynolds numbers of 5800 and 10800 respectively. Table 2 summarizes the decay constants for both jet Reynolds numbers in both the quiescent and turbulent ambient for both concentration and velocity.

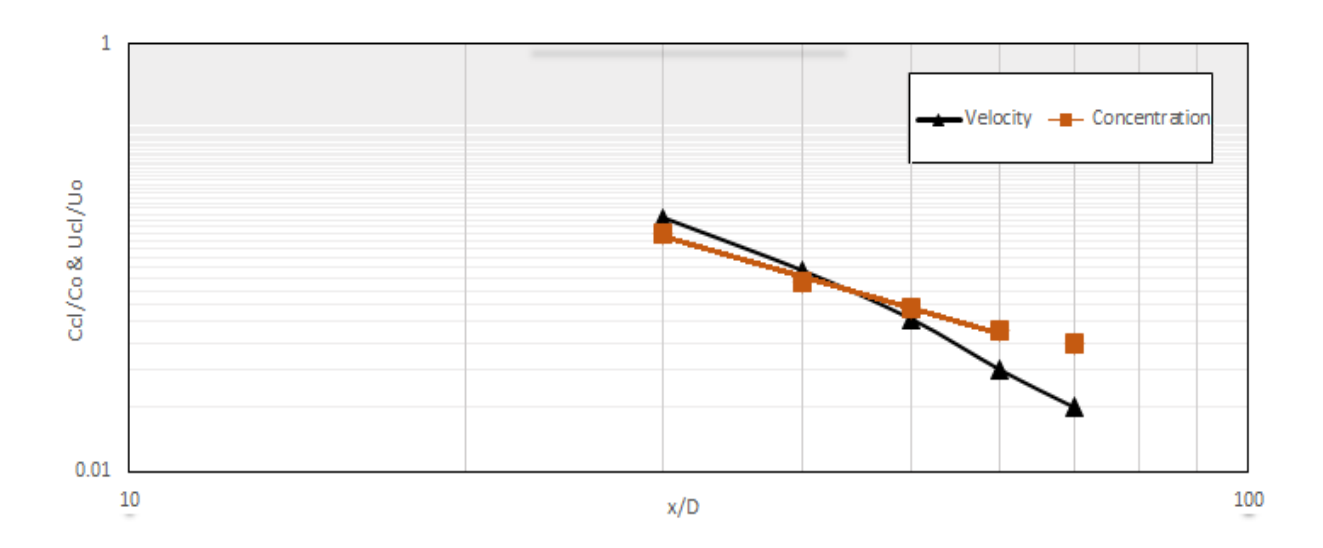


Figure 5.22 comparison of mean centerline velocities and concentrations of the turbulent jet with Reynolds number of 5800 subjected to the turbulent ambient [at streamwise normalized axial distances of 20, 30, 40, 50, and 60 (turbulent ambient)]

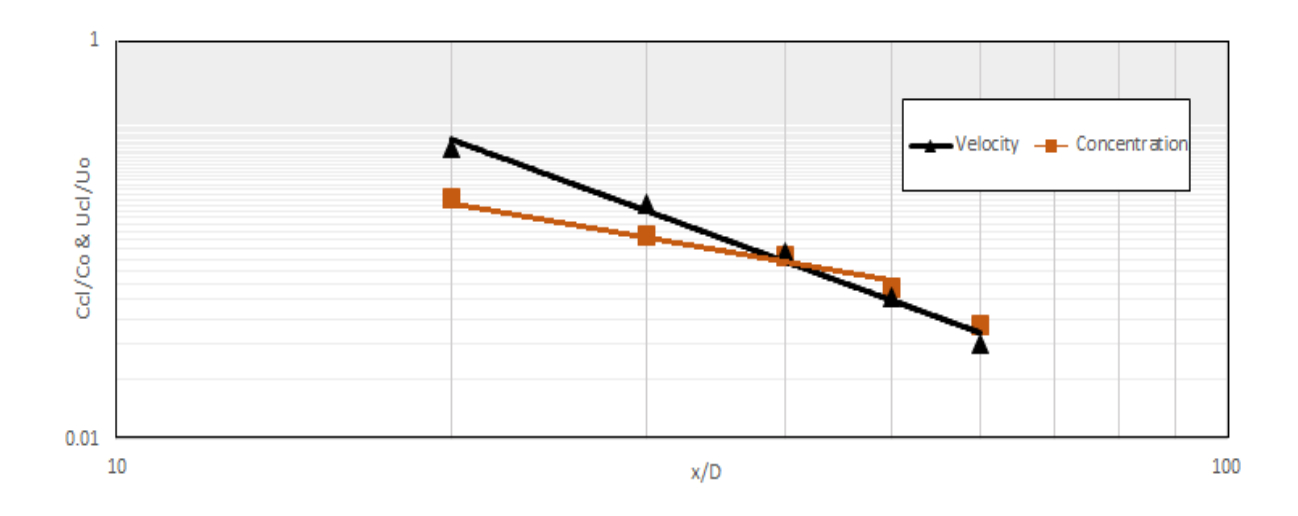


Figure 5.23 comparison of mean centerline velocities and concentrations of the turbulent jet with Reynolds number of 10600 subjected to the turbulent ambient [at streamwise normalized axial distances of 30, 40, 50, 60, and 70 (turbulent ambient)]

Table 5.2: Decay constants for centreline mean velocity and concentration for the jet in quiescent and turbulent ambient.

Jet Reynolds number	Velocity decay	Concentration decay
Quiescent ambient:		
Re = 5800	x^{-1} , for $x/D \le 70$	x^{-1} , for $x/D \le 70$
Re = 10600	x^{-1} , for $x/D \le 70$	x^{-1} , for $x/D \le 70$
Turbulent ambient:		
Re = 5800	$x^{-2.5}$, for $x/D \le 45$	$x^{-1.7}$, for $x/D \le 50$
Re = 10600	$x^{-1.8}$, for $x/D \le 50$	$x^{-1.2}$, for $x/D \le 60$

This behaviour is explained as the jet is relatively undisrupted by the ambient turbulence when its turbulence is much greater, i.e. closer to the jet exit. At a certain point downstream the jet turbulence has decreased such that the ambient turbulence is now great than it, this it the point of jet breakup. In between these two regions, turbulent fluid from the ambient is entrained into the jet and has an effect on the jet width growth. In addition, the larger eddies of the ambient turbulence displace the jet causing its path to meander.

Chapter 6: Conclusions

When a turbulent jet issues into and ambient that is turbulent, the ambient turbulence disrupts the jet structure. This is seen in the visualization of the jet, and the shape factor describing the jet cross-section shape. The jet structure becomes more variable and the path of the jet meanders until at some point the velocity of the jet has decreased to the extent that the jet no longer exists. The evidence of the breakup of the jet is the change in the behaviour with axial distance of the rate of decay of the mean centreline concentration, the jet width growth and the radius of gyration growth. These parameters all indicate a break up of the jet of Re = 5800 at x/D between 40 and 50 and the breakup of the jet of Re = 10600 at x/D between 50 and 60.

The ambient turbulence has a greater effect on the jet with the lower Reynolds number, as seen in the greater rate of centreline concentration decay, the increased rate of width growth and increased rate of radius of gyration growth. This can be explained by the lower jet turbulence and lower jet momentum at the lower Reynolds number, resulting in more disruption by the ambient turbulence.

The disruption of the jet results in both an increase in the rate of increase of the radius of gyration of the jet, which is caused by the smaller length scales of the turbulence being entrained into the jet. It also results in a meandering of the jet path due to the larger length scales of the ambient turbulence displacing the jet. These effects are greater for the lower Reynolds number jet as it has a lower turbulence intensity and a lower jet momentum and hence is more vulnerable to disruption by the ambient turbulence.

When the jet cross-sections are averaged spatially with time, the width growth includes the effect of the increase of the jet cross-section and of the meandering of the jet path. The effect of the meandering of the jet can be removed by averaging the jet by superimposing the jet centers of mass. The rate of growth of radius of gyration of jet cross-sections was then compared for the quiescent and turbulent ambient. Again, the lower Reynolds number jet has the greater increase of radius of gyration in the turbulent ambient.

At some point in the axial direction, the jet structure will decay to the point that the jet no longer exists. This can be more easily identified from the jet velocity as zero mean centerline velocity means no jet. For the case of the jets with Reynolds numbers of 5800 and 10600, this decay of the jet in the quiescent ambient occurred beyond x/D = 70, the limit of the experimental data. For the

jets issuing into the turbulent ambient, the jet with Reynolds number of 5800 had decayed by x/D between 40 and 50, while the jet with Reynolds number of 10600 had decayed by x/D between 50 and 60.

The comparison of the decay of the centreline mean velocity and the centreline mean scalar concentration shows that the jet velocity decays at a faster rate in the turbulence as compared to the scalar concentration. This is because once the jet momentum has decayed, its evidence, the velocity, is not longer measurable. However, the scalar is conserved, so even when it is not being further advected by jet momentum, it is still measurable.

This research on the effect of ambient turbulence on the dilutions possible with a jet has implications for the design of ocean outfalls that issue into an environment with a back ground turbulence level. Current practise is to assume that the jet will produce the dilution that is possible in a quiescent ambient and that this is the starting point for the turbulent diffusion by the turbulence in the receiving fluid (ocean, lake). This is not a conservative assumption, because when there is turbulence in the ambient it will cause the jet to decay more quickly, thereby producing a lower initial dilution that will then undergo the turbulent diffusion. The magnitude of this decrease in dilution rate is greater when the outfall jet has a lower jet momentum and lower jet velocity. However, the absolute magnitude of this effect is as yet unknown as a parameter study has not been undertaken for a large range of jet Reynolds numbers and ambient turbulence intensities.

References

Aanen, L., et al. (1999). "Measurement of turbulent mixing usind PIV and LIF." Machine Graphics and vision 8(4): 529-543.

Amoura, Z., et al. (2010). "Attenuation of the wake of a sphere in an intense incident turbulence with large length scales." Physics of fluids 22(5): 055105.

Antoine, Y., et al. (2001). "Turbulent transport of a passive scalar in a round jet discharging into a co-flowing stream." European Journal of Mechanics-B/Fluids 20(2): 275-301

Antonia, R. and P. Orlandi (2003). "Effect of Schmidt number on small-scale passive scalar turbulence." Applied Mechanics Reviews 56(6): 615-632.

Batchelor, G. K. (1959). "Small-scale variation of convected quantities like temperature in turbulent fluid Part 1. General discussion and the case of small conductivity." Journal of Fluid Mechanics 5(1): 113-133.

Becker, H., et al. (1967). "The nozzle-fluid concentration field of the round, turbulent, free jet." Journal of Fluid Mechanics 30(2): 285-303.

Belin, F., et al. (1997). "Velocity gradient distributions in fully developed turbulence: An experimental study." Physics of fluids 9(12): 3843-3850.

Bellani, G. and E. A. Variano (2014). "Homogeneity and isotropy in a laboratory turbulent flow." Experiments in Fluids 55(1): 1646.

Berg, J., et al. (2006). "Backwards and forwards relative dispersion in turbulent flow: an experimental investigation." Physical Review E 74(1): 016304.

Birch, A., et al. (1978). "The turbulent concentration field of a methane jet." Journal of Fluid Mechanics 88(3): 431-449.

Blum, D. B., et al. (2011). "Signatures of non-universal large scales in conditional structure functions from various turbulent flows." New Journal of Physics 13(11): 113020.

Bodenschatz, E., et al. (2014). "Variable density turbulence tunnel facility." Review of Scientific Instruments 85(9): 093908.

Buch, K. A. and W. J. Dahm (1996). "Experimental study of the fine-scale structure of conserved scalar mixing in turbulent shear flows. Part 1. Sc [Gt] 1." Journal of Fluid Mechanics 317: 21-71.

Burattini, P. and L. Djenidi (2004). "Velocity and passive scalar characteristics in a round jet with grids at the nozzle exit." Flow, Turbulence and Combustion 72(2-4): 199-218.

Burridge, H., et al. (2017). "Conditional sampling of a high Péclet number turbulent plume and the implications for entrainment." Journal of Fluid Mechanics 823: 26-56.

Carlier, J. and K. Sodjavi (2016). "Turbulent mixing and entrainment in a stratified horizontal plane shear layer: joint velocity–temperature analysis of experimental data." Journal of Fluid Mechanics 806: 542-579.

Catrakis, H. J. and P. E. Dimotakis (1996). "Mixing in turbulent jets: scalar measures and isosurface geometry." Journal of Fluid Mechanics 317: 369-406.

Chang, K., et al. (2012). "Experimental study of the influence of anisotropy on the inertial scales of turbulence." Journal of Fluid Mechanics 692: 464-481.

Chen, D. and G. H. Jirka (1999). "LIF study of plane jet bounded in shallow water layer." Journal of Hydraulic Engineering 125(8): 817-826.

Ching, C., et al. (1995). "Breakdown of line plumes in turbulent environments." Journal of Geophysical Research: Oceans 100(C3): 4707-4713.

Corrsin, S. (1951). "On the spectrum of isotropic temperature fluctuations in an isotropic turbulence." Journal of Applied Physics 22(4): 469-473.

Corrsin, S. and A. L. Kistler (1955). "Free-stream boundaries of turbulent flows."

Cowen, E., et al. (2001). "A single-camera coupled PTV–LIF technique." Experiments in Fluids 31(1): 63-73.

Craft, T. and B. Launder (2001). "On the spreading mechanism of the three-dimensional turbulent wall jet." Journal of Fluid Mechanics 435: 305-326.

Crimaldi, J. and J. Koseff (2006). "Structure of turbulent plumes from a momentumless source in a smooth bed." Environmental Fluid Mechanics 6(6): 573-592.

Crimaldi, J. P., et al. (2002). "The relationship between mean and instantaneous structure in turbulent passive scalar plumes." J. Turbul 3(014): 1-24.

Dahm, W. and P. Dimotakis (1987). "Measurements of entrainment and mixing in turbulent jets." AIAA journal 25(9): 1216-1223.

Dahm, W. J. and P. E. Dimotakis (1990). "Mixing at large Schmidt number in the self-similar far field of turbulent jets." Journal of Fluid Mechanics 217: 299-330.

Darisse, A., et al. (2015). "Budgets of turbulent kinetic energy, Reynolds stresses, variance of temperature fluctuations and turbulent heat fluxes in a round jet." Journal of Fluid Mechanics 774: 95-142.

Dasi, L., et al. (2007). "The geometric properties of high-Schmidt-number passive scalar isosurfaces in turbulent boundary layers." Journal of Fluid Mechanics 588: 253-277.

Dimotakis, P. E. (1986). "Two-dimensional shear-layer entrainment." AIAA journal 24(11): 1791-1796.

Dimotakis, P. E. (2000). "The mixing transition in turbulent flows." Journal of Fluid Mechanics 409: 69-98.

Dimotakis, P. E. (2005). "Turbulent mixing." Annu. Rev. Fluid Mech. 37: 329-356.

Douady, S., et al. (1991). "Direct observation of the intermittency of intense vorticity filaments in turbulence." Physical review letters 67(8): 983.

Dowling, D. R. and P. E. Dimotakis (1990). "Similarity of the concentration field of gas-phase turbulent jets." Journal of Fluid Mechanics 218: 109-141.

Eriksson, J., et al. (1998). "An experimental study of a two-dimensional plane turbulent wall jet." Experiments in Fluids 25(1): 50-60.

Feng, H., et al. (2006). Conditional Statistics for Passive-Scalar Mixing in Confined Turbulent Shear Flows. ASME 2006 International Mechanical Engineering Congress and Exposition, American Society of Mechanical Engineers.

Fischer, H. B., et al. (2013). Mixing in inland and coastal waters, Elsevier.

Fukushima, C., et al. (2002). Investigation of the mixing process in an axisymmetric turbulent jet using PIV and LIF. Laser techniques for fluid mechanics, Springer: 339-356.

Funatani, S., et al. (2004). "Simultaneous measurement of temperature and velocity using two-colour LIF combined with PIV with a colour CCD camera and its application to the turbulent buoyant plume." Measurement Science and Technology 15(5): 983.

Gampert, M., et al. (2013). "Experimental investigation of dissipation-element statistics in scalar fields of a jet flow." Journal of Fluid Mechanics 724: 337-366.

Gaskin, S., et al. (2004). "The effect of background turbulence on jet entrainment: an experimental study of a plane jet in a shallow coflow." Journal of hydraulic research 42(5): 533-542.

George, W. K. (1989). "The self-preservation of turbulent flows and its relation to initial conditions and coherent structures." Advances in turbulence 3973.

Gibson, C. and W. Schwarz (1963). "The universal equilibrium spectra of turbulent velocity and scalar fields." Journal of Fluid Mechanics 16(3): 365-384.

Giger, M., et al. (1991). "Entrainment and mixing in plane turbulent jets in shallow water." Journal of hydraulic research 29(5): 615-642.

Goepfert, C., et al. (2010). "Characterization of a system generating a homogeneous isotropic turbulence field by free synthetic jets." Experiments in Fluids 48(5): 809-822.

Gordon, M., et al. (2004). "Investigation of the mean passive scalar field in zero-net-mass-flux jets in cross-flow using planar-laser-induced fluorescence." Physics of fluids 16(3): 794-808.

Guillard, F., et al. (1998). "Mixing in a confined turbulent impinging jet using planar laser-induced fluorescence." Experiments in Fluids 25(2): 143-150.

Guo, Y., et al. (1999). Influence of background turbulence on the evolution of turbulent jets. Conference Proceedings of the 28th IAHR Congress. International Association of Hydro-Environment Engineering and Research (IAHR).

Hancock, P. and P. Bradshaw (1989). "Turbulence structure of a boundary layer beneath a turbulent free stream." Journal of Fluid Mechanics 205: 45-76.

Hancock, P. E. and P. Bradshaw (1983). "The effect of free-stream turbulence on turbulent boundary layers." Journal of Fluids Engineering 105(3): 284-289.

Hunt, J. (1994). Atmospheric jets and plumes. Recent Research Advances in the Fluid Mechanics of Turbulent Jets and Plumes, Springer: 309-334.

Hunt, J. C., et al. (2008). Vortical interactions with interfacial shear layers. IUTAM Symposium on Computational Physics and New Perspectives in Turbulence, Springer.

Hussein, H. J., et al. (1994). "Velocity measurements in a high-Reynolds-number, momentum-conserving, axisymmetric, turbulent jet." Journal of Fluid Mechanics 258: 31-75.

Johari, H. and R. Paduano (1997). "Dilution and mixing in an unsteady jet." Experiments in Fluids 23(4): 272-280.

Kabanshi, A., et al. (2018). Measurement of Entrainment into an Axisymmetric Jet using Temperature as a Tracer: A Pilot Study. Roomvent and Ventilation 2018.

Khorsandi, B. (2011). Effect of Background Turbulence on an Axisymmetric Turbulent Jet, McGill University.

Khorsandi, B., et al. (2013). "Effect of background turbulence on an axisymmetric turbulent jet." Journal of Fluid Mechanics 736: 250-286.

Kolmogorov, A. N. The local structure of turbulence in incompressible viscous fluid for very large Reynolds numbers.

Kolmogorov, A. N. (1941). Dissipation of energy in locally isotropic turbulence. Dokl. Akad. Nauk SSSR.

Kothnur, P. and N. Clemens (2005). "Effects of unsteady strain rate on scalar dissipation structures in turbulent planar jets." Physics of fluids 17(12): 125104.

Kravtsov, Z., et al. (2016). Acetone PLIF concentration measurements in a submerged round turbulent jet. AIP Conference Proceedings, AIP Publishing.

Krug, D., et al. (2014). "A combined scanning PTV/LIF technique to simultaneously measure the full velocity gradient tensor and the 3D density field." Measurement Science and Technology 25(6): 065301.

Lavertu, T., et al. (2008). "Differential diffusion of high-Schmidt-number passive scalars in a turbulent jet." Journal of Fluid Mechanics 612: 439-475.

Lavertu, T. M. (2006). Differential diffusion in a turbulent jet.

Law, A. W.-K. and H. Wang (2000). "Measurement of mixing processes with combined digital particle image velocimetry and planar laser induced fluorescence." Experimental Thermal and Fluid Science 22(3-4): 213-229.

Liao, Q. and E. Cowen (2010). "Relative dispersion of a scalar plume in a turbulent boundary layer." Journal of Fluid Mechanics 661: 412-445.

Lipari, G. and P. K. Stansby (2011). "Review of experimental data on incompressible turbulent round jets." Flow, Turbulence and Combustion 87(1): 79-114.

Liu, S., et al. (1999). "Evolution and modelling of subgrid scales during rapid straining of turbulence." Journal of Fluid Mechanics 387: 281-320.

Lockwood, F. and H. Moneib (1980). "Fluctuating temperature measurements in a heated round free jet." Combustion Science and Technology 22(1-2): 63-81.

Long, M., et al. (1981). "Instantaneous two-dimensional gas concentration measurements by light scattering." AIAA journal 19(9): 1151-1157.

Lubbers, C., et al. (2001). "Simulation of the mixing of a passive scalar in a round turbulent jet." Fluid Dynamics Research 28(3): 189.

Mathew, J. and A. J. Basu (2002). "Some characteristics of entrainment at a cylindrical turbulence boundary." Physics of fluids 14(7): 2065-2072.

McKenna, S. P. and W. R. McGillis (2004). "Observations of flow repeatability and secondary circulation in an oscillating grid-stirred tank." Physics of fluids 16(9): 3499-3502.

Mellado, J. P., et al. (2009). "Gradient trajectory analysis of a scalar field with external intermittency." Journal of Fluid Mechanics 626: 333-365.

Meneveau, C. and K. Sreenivasan (1990). "Interface dimension in intermittent turbulence." Physical Review A 41(4): 2246.

Mi, J., et al. (2001). "Influence of jet exit conditions on the passive scalar field of an axisymmetric free jet." Journal of Fluid Mechanics 432: 91-125.

Miller, P. L. and P. E. Dimotakis (1991). "Reynolds number dependence of scalar fluctuations in a high Schmidt number turbulent jet." Physics of Fluids A: Fluid Dynamics 3(5): 1156-1163.

Miller, P. L. and P. E. Dimotakis (1996). "Measurements of scalar power spectra in high Schmidt number turbulent jets." Journal of Fluid Mechanics 308: 129-146.

Mistry, D. and J. Dawson (2014). Experimental investigation of multi-scale entrainment processes of a turbulent jet. 17th international symposium on applications of laser techniques to fluid mechanics, Lisbon, Portugal.

Mistry, D., et al. (2018). "The multi-scale geometry of the near field in an axisymmetric jet." Journal of Fluid Mechanics 838: 501-515.

Mistry, D., et al. (2016). "Entrainment at multi-scales across the turbulent/non-turbulent interface in an axisymmetric jet." Journal of Fluid Mechanics 802: 690-725.

Mondal, T., et al. (2015). "Computational study of periodically unsteady interaction between a wall jet and an offset jet for various velocity ratios." Computers & Fluids 123: 146-161.

Morton, B., et al. (1956). "Turbulent gravitational convection from maintained and instantaneous sources." Proc. R. Soc. Lond. A 234(1196): 1-23.

Mydlarski, L. and Z. Warhaft (1996). "On the onset of high-Reynolds-number grid-generated wind tunnel turbulence." Journal of Fluid Mechanics 320: 331-368.

Nickels, T. and A. Perry (1996). "An experimental and theoretical study of the turbulent coflowing jet." Journal of Fluid Mechanics 309: 157-182.

Nironi, C., et al. (2015). "Dispersion of a passive scalar fluctuating plume in a turbulent boundary layer. Part I: Velocity and concentration measurements." Boundary-layer meteorology 156(3): 415-446.

Oboukhov, A. (1949). "Structure of the temperature field in turbulent flows." Isv. Geogr. Geophys. Ser. 13: 58-69.

Or, C., et al. (2011). "Potential core lengths of round jets in stagnant and moving environments." Journal of Hydro-environment Research 5(2): 81-91.

Orszag, S. A. (1974). Lectures on the statistical theory of turbulence, Flow Research Incorporated.

Panchapakesan, N. and J. Lumley (1993). "Turbulence measurements in axisymmetric jets of air and helium. Part 1. Air jet." Journal of Fluid Mechanics 246: 197-223.

Panchapakesan, N. and J. Lumley (1993). "Turbulence measurements in axisymmetric jets of air and helium. Part 2. Helium jet." Journal of Fluid Mechanics 246: 225-247.

Pérez-Alvarado, A., et al. (2016). "Effect of the driving algorithm on the turbulence generated by a random jet array." Experiments in Fluids 57(2): 20.

Peterson, B., et al. (2013). "High-speed PIV and LIF imaging of temperature stratification in an internal combustion engine." Proceedings of the Combustion Institute 34(2): 3653-3660.

Pope, S. B. (2000). "Turbulent flows(Book)." Cambridge, United Kingdom: Cambridge University Press, 2000.

Robins, A. (1978). "Plume dispersion from ground level sources in simulated atmospheric boundary layers." Atmospheric Environment (1967) 12(5): 1033-1044.

Romano, G. (2002). "The effect of boundary conditions by the side of the nozzle of a low Reynolds number jet." Experiments in Fluids 33(2): 323-333.

Ryan, K. J., et al. (2017). "Turbulent scalar mixing in a skewed jet in crossflow: experiments and modeling." Flow, Turbulence and Combustion 98(3): 781-801.

Shan, J. W. and P. E. Dimotakis (2006). "Reynolds-number effects and anisotropy in transverse-jet mixing." Journal of Fluid Mechanics 566: 47-96.

Shao, D., et al. (2017). "Flow patterns and mixing characteristics of horizontal buoyant jets at low and moderate Reynolds numbers." International Journal of Heat and Mass Transfer 105: 831-846.

Sharp, N. S., et al. (2009). "Effects of large-scale free stream turbulence on a turbulent boundary layer." Physics of fluids 21(9): 095105.

Shinneeb, A.-M., et al. (2010). "Confinement effects in shallow-water jets." Journal of Hydraulic Engineering 137(3): 300-314.

Shlien, D. J. (1987). "Observations of dispersion of entrained fluid in the self-preserving region of a turbulent jet." Journal of Fluid Mechanics 183: 163-173.

Soltys, M. and J. Crimaldi (2015). "Joint probabilities and mixing of isolated scalars emitted from parallel jets." Journal of Fluid Mechanics 769: 130-153.

Soulopoulos, N., et al. (2015). "Mixing and scalar dissipation rate statistics in a starting gas jet." Physics of fluids 27(12): 125103.

Su, L. K. and N. T. Clemens (2003). "The structure of fine-scale scalar mixing in gas-phase planar turbulent jets." Journal of Fluid Mechanics 488: 1-29.

Tachie, M., et al. (2004). "Roughness effects on turbulent plane wall jets in an open channel." Experiments in Fluids 37(2): 281-292.

Tennekes, H., et al. (1972). A first course in turbulence, MIT press.

Thole, K. and D. Bogard (1996). "High freestream turbulence effects on turbulent boundary layers." Journal of Fluids Engineering 118(2): 276-284.

Thompson, S. and J. Turner (1975). "Mixing across an interface due to turbulence generated by an oscillating grid." Journal of Fluid Mechanics 67(2): 349-368.

Thong, C. X., et al. (2017). "An experimental study on the near flow field of a round jet affected by upstream multi-lateral side-jet." Experimental Thermal and Fluid Science 82: 198-211.

Thong, C. X., et al. (2015). "Flow dynamics of multi-lateral jets injection into a round pipe flow." Experiments in Fluids 56(1): 15.

Tong, C. and Z. Warhaft (1995). "Passive scalar dispersion and mixing in a turbulent jet." Journal of Fluid Mechanics 292: 1-38.

Torres, L. A., et al. (2012). "Mean concentration field of a jet in a uniform counter-flow." Journal of Fluids Engineering 134(1): 014502.

Townsend, A. (1966). "The mechanism of entrainment in free turbulent flows." Journal of Fluid Mechanics 26(4): 689-715.

Trabold, T., et al. (1987). "Entrainment by turbulent jets issuing from sharp-edged inlet round nozzles." Journal of Fluids Engineering 109(3): 248-254.

Tsinober, A. (2001). An informal introduction to turbulence, Springer Science & Business Media.

Vanderwel, C. and S. Tavoularis (2016). "Scalar dispersion by coherent structures in uniformly sheared flow generated in a water tunnel." Journal of Turbulence 17(7): 633-650.

Variano, E. A., et al. (2004). "A random synthetic jet array driven turbulence tank." Experiments in Fluids 37(4): 613-615.

Variano, E. A. and E. A. Cowen (2008). "A random-jet-stirred turbulence tank." Journal of Fluid Mechanics 604: 1-32.

Villermaux, E., et al. (1995). "Intense vortical structures in grid-generated turbulence." Physics of fluids 7(8): 2008-2013.

Voth, G. A., et al. (2002). "Measurement of particle accelerations in fully developed turbulence." Journal of Fluid Mechanics 469: 121-160.

Wang, H. and A. W.-k. Law (2002). "Second-order integral model for a round turbulent buoyant jet." Journal of Fluid Mechanics 459: 397-428.

Wang, L. and N. Peters (2006). "The length-scale distribution function of the distance between extremal points in passive scalar turbulence." Journal of Fluid Mechanics 554: 457-475.

Wang, L. and N. Peters (2008). "Length-scale distribution functions and conditional means for various fields in turbulence." Journal of Fluid Mechanics 608: 113-138.

Webster, D., et al. (2001). "Simultaneous DPTV/PLIF measurements of a turbulent jet." Experiments in Fluids 30(1): 65-72.

Webster, D. R., et al. (2004). "A novel laboratory apparatus for simulating isotropic oceanic turbulence at low Reynolds number." Limnology and Oceanography: Methods 2(1): 1-12.

Wen, X., et al. (2018). "Near-field interaction of an inclined jet with a crossflow: LIF visualization and TR-PIV measurement." Journal of Visualization 21(1): 19-38.

Westerweel, J., et al. (2005). "Mechanics of the turbulent-nonturbulent interface of a jet." Physical review letters 95(17): 174501.

Westerweel, J., et al. (2009). "Momentum and scalar transport at the turbulent/non-turbulent interface of a jet." Journal of Fluid Mechanics 631: 199-230.

Wilson, R. and P. Danckwerts (1964). "Studies in turbulent mixing—II: A hot-air jet." Chemical engineering science 19(11): 885-895.

Wolf, M., et al. (2012). "Investigations on the local entrainment velocity in a turbulent jet." Physics of fluids 24(10): 105110.

Wright, S. J. (1994). The effect of ambient turbulence on jet mixing. Recent research advances in the fluid mechanics of turbulent jets and plumes, Springer: 13-27.

Wygnanski, I. and H. Fiedler (1969). "Some measurements in the self-preserving jet." Journal of Fluid Mechanics 38(3): 577-612.

Xia, L. and K. M. Lam (2009). "Velocity and concentration measurements in initial region of submerged round jets in stagnant environment and in coflow." Journal of Hydro-environment Research 3(1): 21-34.

Xu, D. and J. Chen (2010). Experimental Study of Structure and Dynamics of Turbulent Stratified Jet. ASME 2010 3rd Joint US-European Fluids Engineering Summer Meeting collocated with 8th International Conference on Nanochannels, Microchannels, and Minichannels, American Society of Mechanical Engineers.

Xu, D. and J. Chen (2014). Experimental Study of Mixing and Entrainment in a Horizontal Turbulent Stratified Jet. ASME 2014 4th Joint US-European Fluids Engineering Division Summer Meeting collocated with the ASME 2014 12th International Conference on Nanochannels, Microchannels, and Minichannels, American Society of Mechanical Engineers.

Xu, G. and R. Antonia (2002). "Effect of different initial conditions on a turbulent round free jet." Experiments in Fluids 33(5): 677-683.

Yoda, M., et al. (1994). "Instantaneous three-dimensional concentration measurements in the self-similar region of a round high-Schmidt-number jet." Journal of Fluid Mechanics 279: 313-350.

Yule, A. (1978). "Large-scale structure in the mixing layer of a round jet." Journal of Fluid Mechanics 89(3): 413-432.

Zarruk, G. and E. Cowen (2008). "Simultaneous velocity and passive scalar concentration measurements in low Reynolds number neutrally buoyant turbulent round jets." Experiments in Fluids 44(6): 865-872.

Hu, Y., Liu, Z., Yang, J., Jin, Y., & Cheng, Y. (2010). Study on the reactive mixing process in an unbaffled stirred tank using planar laser-induced fluorescence (PLIF) technique. Chemical Engineering Science, 65(15), 4511-4518.

Hanson, R. K., Spearrin, R. M., & Goldenstein, C. S. (2016). Laser-Induced Fluorescence. In Spectroscopy and Optical Diagnostics for Gases (pp. 177-199). Springer, Cham.

Donges, A., & Noll, R. (2015). Laser-Induced Fluorescence. In Laser Measurement Technology (pp. 373-392). Springer, Berlin, Heidelberg.

Cho, K. Y., Satija, A., Pourpoint, T. L., Son, S. F., & Lucht, R. P. (2014). High-repetition-rate three-dimensional OH imaging using scanned planar laser-induced fluorescence system for multiphase combustion. Applied optics, 53(3), 316-326.

Deusch, S., & Dracos, T. (2001). Time resolved 3D passive scalar concentration-field imaging by laser induced fluorescence (LIF) in moving liquids. Measurement Science and Technology, 12(2), 188.

Larsen, L. G., & Crimaldi, J. P. (2006). The effect of photobleaching on PLIF. Experiments in fluids, 41(5), 803-812.

Marcek Chorvatova, A., Kirchnerova, J., Cagalinec, M., Mateasik, A., & Chorvat Jr, D. (2018). Spectrally and spatially resolved laser-induced photobleaching of endogenous flavin fluorescence in cardiac myocytes. Cytometry Part A.

Smith, D. C. (1977). High-power laser propagation: thermal blooming. Proceedings of the IEEE, 65(12), 1679-1714.

Crimaldi, J. P. (2008). Planar laser induced fluorescence in aqueous flows. Experiments in fluids, 44(6), 851-863.

Wang, G. R., & Fiedler, H. E. (2000). On high spatial resolution scalar measurement with LIF Part 1: Photobleaching and thermal blooming. Experiments in fluids, 29(3), 257-264.

Koochesfahani, M. M. (1984). Experiments on turbulent mixing and chemical reactions in a liquid mixing layer (Doctoral dissertation, California Institute of Technology).

Vanderwel, C., & Tavoularis, S. (2014). On the accuracy of PLIF measurements in slender plumes. Experiments in fluids, 55(8), 1801.

Wang, G. R., & Fiedler, H. E. (2000). On high spatial resolution scalar measurement with LIF Part 2: the noise characteristic. Experiments in Fluids, 29(3), 265-274.

Ferrier, A. J., Funk, D. R., & Roberts, P. J. W. (1993). Application of optical techniques to the study of plumes in stratified fluids. Dynamics of Atmospheres and Oceans, 20(1-2), 155-183.

Koochesfahani, M., & Dimotakis, P. E. (1985). Laser-induced fluorescence measurements of mixed fluid concentration a liquid plane shear layer. AIAA journal, 23(11), 1700-1707.

Guillard, F., Fritzon, R., Revstedt, J., Trägårdh, C., Alden, M., & Fuchs, L. (1998). Mixing in a confined turbulent impinging jet using planar laser-induced fluorescence. Experiments in fluids, 25(2), 143-150.

Guilbault, G. G. (Ed.). (1990). Practical fluorescence (Vol. 3). CRC Press.

Lavertu, T. M. 2006. Differential diffusion in a turbulent jet. PhD thesis, McGill University.

Shan, J. W., Lang, D. B., & Dimotakis, P. E. (2004). Scalar concentration measurements in liquidphase flows with pulsed lasers. Experiments in Fluids, 36(2), 268-273.

Crimaldi, J. P. (2008). Planar laser induced fluorescence in aqueous flows. Experiments in fluids, 44(6), 851-863.

Ball, C. G., Fellouah, H., & Pollard, A. (2012). The flow field in turbulent round free jets. Progress in Aerospace Sciences, 50, 1-26.

Dahm, W. J., & Dimotakis, P. E. (1990). Mixing at large Schmidt number in the self-similar far field of turbulent jets. Journal of Fluid Mechanics, 217, 299-330.

Law, A. W. K., & Wang, H. (2000). Measurement of mixing processes with combined digital particle image velocimetry and planar laser induced fluorescence. Experimental Thermal and Fluid Science, 22(3-4), 213-229.

Webster, D. R., Roberts, P. J. W., & Ra'ad, L. (2001). Simultaneous DPTV/PLIF measurements of a turbulent jet. Experiments in Fluids, 30(1), 65-72.

Fukushima, C., Aanen, L., & Westerweel, J. (2002). Investigation of the mixing process in an axisymmetric turbulent jet using PIV and LIF. In Laser techniques for fluid mechanics (pp. 339-356). Springer, Berlin, Heidelberg.

Pérez-Alvarado, A., Mydlarski, L., & Gaskin, S. (2016). Effect of the driving algorithm on the turbulence generated by a random jet array. Experiments in Fluids, 57(2), 20.

GORGEON, A. Ü. A., & GÖKALP, S. (1993). A planar laser induced fluorescence study of turbulent flame kernel growth and fractal characteristics. Combustion science and technology, 92(4-6), 265-290.

Wilkes, J. A., Danehy, P. M., & Nowak, R. J. (2005). Fluorescence imaging study of transition in underexpanded free jets. In Instrumentation in Aerospace Simulation Facilities, 2005. iciasf'05. 21st International Congress on (pp. 1-8). IEEE.